

TESIS DOCTORAL

2023

PEM FUEL CELL SPATIAL HOMOGENEITY AND TEMPORAL STABILITY STUDY USING LONG-TERM DYNAMIC SIMULATIONS

Sergi Culubret i Cortada

PROGRAMA DE DOCTORADO EN INGENIERÍA DE
SISTEMAS Y CONTROL

Miguel Ángel Rubio González

Acknowledgements

Quiero agradecer especialmente esta tesis a su director Miguel Ángel Rubio por todo el trabajo realizado, su tiempo dedicado y su incuestionable paciencia. Por las ganas de hacer un trabajo mejor día a día, por transmitirlas y por el esfuerzo puesto para que así fuera. La experiencia de trabajar con él uno de los mejores intangibles que me llevo.

A los compañeros de la DLR, especialmente a Dani García que ha colaborado aportando los datos experimentales e iterativas revisiones y correcciones.

También quiero agradecer al departamento, especialmente a Alfonso Urquía, por la oportunidad que me brindó de realizar investigación en su departamento y de asistir en el curso realizado por la St. Petersburg University in Russia. También a Raquel Dormido por su apoyo y soporte cuando lo necesitaba.

Finalmente querría agradecer a mi familia:

Voldria especialment agrair la paciència a la meva parella, l'Aina, que durant tots aquests anys ha estat al meu costat animant-me quan més ho necessitava. També voldria agrair als meus pares, Jordi i Mercè, i a la meva germana Clara, per creure en mi des del primer moment, no seria res sense ells.

Abstract

The temporal stability and spatial homogeneity of a Polymer Electrolyte Membrane Fuel Cell (PEMFC) performance during constant demand operation are key factors in ensuring the durability of its components. Spatial and temporal differences in the state of the cell, such as current density, fuel concentration, or membrane water load level, cause non-uniform degradation of the cell, shortening its lifetime.

To study the cell operating and design factors that may contribute to the improvement of the cell's stability and homogeneity, a dynamic pseudo-3D model capable of performing long-term and intensive simulations of PEMFC with low computational cost has been developed. The model is designed to simulate the impact of different flow field topologies and operating parameters to evaluate the overall fuel cell performance considering relevant phenomena in the homogeneity and stability of the cell, such as fuel and relative humidity concentration along the flow field, water droplets movement in the flow field, electrochemical reactions, and others.

The model has been implemented using independent submodels interconnected using a sequential strategy. This strategy enabled to independently analyze and validate each submodel and interconnect them using only the required variables. The complete model is composed of two groups of submodels representing the cell's main physical components, a) the MEA and b) the flow field. The main physical phenomena that are represented in the MEA model are the electrochemical reactions, the membrane water balance, the gases and water diffusion in the gas diffusion layers (GDL), the evaporation and condensation of water from the GDLs, and the liquid water removal from the GDL. The flow field model represents the following phenomena: the pressure drop due to channel geometry and the species consumption, the gas species distribution along the channels, the movement of liquid water droplets, the liquid water droplet's evaporation, and the water re-absorption to the GDL.

The model has been validated using two experimental data, a 25 cm² cell with a single serpentine operating under drying and humidifying cycles and a 141 cm² cell with 23 parallel channels applying different relative humidity conditions, which current density distribution is measured using the segmented cell method. The experimental data allows the model to be validated dynamically and spatially, focusing on water management.

The model simulations have been performed to study the homogeneity and stability of the cell, evaluating the effect of the channel/rib ratio, the number of

parallel channels, and the stoichiometry ratio. The parallel serpentine and straight parallel designs have been compared. Moreover, single design parameters, such as gas diffusion layer thickness, the membrane thickness, or operating parameters, such as operating temperature and co-flow or counter-flow design, have been analyzed. A total of 52 long-term simulation experiments have been conducted.

The simulated experiments' results show the importance of an adequate flow field design and gas flow control to remove the channel's liquid water and keep a homogeneous feeding. Furthermore, the importance of proper control of the gas diffusion layer and membrane thickness is observed to balance the water content between the anode and the cathode and reduce the local variability due to liquid water removal. Moreover, the temperature has significantly impacted the cell's homogeneity and stability due to its influence on the water evaporation rate. Finally, the effect of co-flow or counter-flow configuration has been proven to be significant in the current density homogeneity of the cell.

Resumen

La estabilidad temporal y la homogeneidad espacial de una pila de combustible de membrana electrolítica polimérica (PEMFC) durante una operación en demanda de corriente constante son factores clave para asegurar la durabilidad de los componentes. Variaciones en el estado de funcionamiento espaciales y temporales tales como de densidad de corriente, de concentración de especies o de cantidad de agua en la membrana son causantes de degradación no uniforme en la pila, reduciendo su vida útil.

Para estudiar los parámetros de operación y diseño que contribuyen en la mejoría del comportamiento en estabilidad y homogeneidad se ha desarrollado un modelo dinámico pseudo-3D que es capaz de realizar simulaciones de larga duración y de forma intensiva de la PEMFC con un bajo coste computacional. El modelo ha sido diseñado para simular el impacto de diferentes topologías de distribuciones de flujo y parámetros operacionales, para evaluar el rendimiento global de la celda considerando fenómenos importantes que afectan a la homogeneidad y estabilidad, como la evolución de la concentración de la humedad relativa y los combustibles, el movimiento de las gotas de agua dentro de los canales de distribución de gas o las reacciones electroquímicas, entre otros.

El modelo ha sido implementado usando una estrategia secuencial de submodelos independientes interconectados. Esta estrategia permite validar y analizar de forma independiente cada submodelo e interrelacionarlos usando las variables de estado necesarias. El modelo completo está formado por dos grupos de submodelos que representan los principales componentes físicos, a) la MEA y b) el patrón de flujo. Los fenómenos físicos que ocurren en cada componente són, en la MEA las reacciones electroquímicas, el balance de agua de la membrana, la difusión de gases y agua en las capas de difusión gaseosa (GDL), la evaporación de agua y extracción de agua líquida de las GDL; en el patrón de flujo se modela la pérdida de presión del gas debido a la geometría del canal y consumo de especies, la distribución de las especies dentro de los canales, el movimiento del agua líquida en forma de gotas, la evaporación de las gotas, y la reabsorción de agua hacia la GDL.

La validación del modelo se ha realizado usando datos experimentales de una pila de 25 cm² con un solo serpentín operando en ciclos de secado y humectación y con una pila segmentada de 141 cm² con 23 canales en paralelo usando diferentes niveles de

humidificación para observar la distribución de corriente. Los datos experimentales usados han permitido validar el modelo de forma dinámica y espacial, enfocando la validación a la gestión del agua en la celda.

El modelo ha sido usado para estudiar múltiples configuraciones de celda y evaluar su homogeneidad y estabilidad. Las simulaciones han servido para evaluar el efecto de la relación canal-costilla, el número de canales paralelos y la relación de estequiometría. Se ha comparado el uso de canales paralelos en serpentín con canales rectos paralelos. Además, se ha estudiado el impacto de variaciones individuales de parámetros de diseño de la pila como el grosor de la capa difusora, el grosor de la membrana o de parámetros operativos como la temperatura o el sentido del flujo de los gases en co-flujo o a contra-flujo. Para el estudio se han realizado un total de 52 simulaciones de larga duración.

Los resultados de los experimentos realizados muestran la importancia de un adecuado patrón de flujo y del control del flujo de gas para eliminar correctamente el agua líquida de los canales y mantener una alimentación constante y uniforme. Además, se ha observado la relevancia de asegurar un grosor tanto de la capa difusora como de la membrana para tener un balance adecuado de agua entre el ánodo y el cátodo, y reducir la variabilidad local debida a la variabilidad de la eliminación de agua líquida de la GDL. También se ha demostrado importante el impacto de la temperatura en la homogeneidad y estabilidad de la celda debido a su influencia en la capacidad de evaporación de agua. Finalmente, el efecto del sentido del flujo de los gases a contra-flujo o en co-flujo se ha demostrado significativo en la homogeneidad de la densidad de corriente de la celda.

Contents

1	Introduction, objectives and structure	1
1.1	Introduction	1
1.2	Objectives	3
1.3	Dissertation structure	4
2	Fuel Cell Introduction	7
2.1	Introduction	7
2.2	History of fuel cells	8
2.3	Types of fuel cells	10
2.3.1	Alkaline fuel cells (AFC)	10
2.3.2	Phosphoric acid fuel cells (PAFC)	11
2.3.3	Solid oxide fuel cells (SOFC)	12
2.3.4	Molten carbonate fuel cells (MCFC)	13
2.3.5	Direct Methanol fuel cells (DMFC)	13
2.3.6	Reversible fuel cells (RFC)	14
2.3.7	Polymer electrolyte membrane (PEM)	15
2.3.8	Conclusions	16
3	PEM fuel cells introduction	17
3.1	Introduction	17
3.2	PEM fuel cell components	18
3.2.1	Membrane-Electrode Assembly (MEA)	19
3.2.2	Bipolar plates	24
3.2.3	Flow field	25
3.2.4	Cooling plates	27
3.2.5	Auxiliary components	27
3.3	PEM Fuel cell technology challenges	29
3.3.1	Technological challenges	30
3.3.2	Economical challenges	31
3.3.3	Material cost	31
3.3.4	Complementary operations	32
3.4	Conclusions	34

4	Introduction to PEM fuel cell modeling	35
4.1	Introduction	35
4.2	Modeling challenges in PEM fuel cells	36
4.2.1	Water management	37
4.2.2	Heat management	39
4.2.3	Fuel feeding	40
4.3	Model classification in PEM fuel cells	41
4.3.1	Dimensional classification	42
4.3.2	Structural classification	44
4.3.3	Dynamic classification	46
4.3.4	Thermal classification	46
4.4	Conclusions	47
5	Modeling hypothesis	49
5.1	Introduction	49
5.2	Submodel description	51
5.2.1	MEA modeled phenomena	52
5.2.2	Flow field modeled phenomena	54
5.3	Models classification summary	55
5.4	MEA model	56
5.4.1	Electrochemical model	56
5.4.2	Membrane water balance	68
5.4.3	GDL water and gas diffusion	71
5.4.4	GDL water evaporation and condensation	76
5.4.5	GDL liquid water removal	79
5.5	Flow field model	80
5.5.1	Gas pressure drop along the flow field	81
5.5.2	Concentration variation of species in the flow field	83
5.5.3	Droplet movement model	87
5.5.4	Droplet water evaporation	98
5.5.5	Droplet water re-absorption	99
5.6	Conclusions	100
6	Numerical implementation and simulation procedure	101
6.1	Introduction	101
6.2	Simulation methodology	102
6.3	Simulation procedure	106
6.4	Submodels numerical implementation	110
6.4.1	Iterative solving	111
6.4.2	Flow field discrete model	112

6.4.3	Finite time centered scheme	113
6.4.4	Droplet re-absorption numerical implementation	116
6.4.5	Liquid water removal from the GDL	117
6.5	Conclusions	118
7	Model experimental validation	119
7.1	Introduction	119
7.2	Temporal stability analysis	120
7.3	Experimental data and simulation	122
7.3.1	Different relative humidity conditions	123
7.3.2	Drying and humidification cycles	126
7.4	Model performance on validation setups	131
7.5	Conclusions	133
8	Analysis of simulation results	135
8.1	Introduction	135
8.2	Experimental investigation	136
8.3	Uniformity general study (Exp ₁)	140
8.4	Serpentine and parallel channel design (Exp ₂)	148
8.5	GDL thickness (Exp ₃)	149
8.6	Membrane thickness (Exp ₄)	153
8.7	Temperature (Exp ₅)	156
8.8	Co-flow and counter-flow (Exp ₆)	159
8.9	Conclusions	160
9	Conclusions and future work	163
9.1	Conclusions	163
9.2	Future work	165
A	Nomenclature	167
B	List of Figures	175
C	List of Tables	181
D	Implementation code samples	183
D.1	Electrochemical model	184
D.1.1	Voltage and current density calculation	184
D.1.2	Electrochemical model	186
D.1.3	Activation overpotential	186
D.1.4	Ohmic overpotential	186

D.1.5	Concentration overpotential	187
D.1.6	Electro-osmotic drag	188
D.1.7	Back-diffusion algorithm	188
D.2	GDL Model	189
D.2.1	FTCS algorithm	189
D.2.2	Liquid water removal from GDL	191
D.2.3	Water evaporation from the GDL	192
D.2.4	Water condensation from the GDL	193
D.3	Droplet movement	194
Bibliography		195

1

Introduction, objectives and structure

Contents

1.1	Introduction	1
1.2	Objectives	3
1.3	Dissertation structure	4

1.1 Introduction

Nowadays, society agrees that climate change is a critical problem. The excess of pollution produced by factories, private automobiles, and others had set a countdown to life on earth as we know it.

The industrial revolution, back in mid 18th century, made the first step towards the current state, but it was around 1890s when we reached a tipping point. In 1887 one of the first car races was held [1], at the end of the 19th century, three kinds of technologies were competing in these races a) the steam-powered, b) gasoline-powered, and c) electric cars. A steam-powered car won the race, but it became disqualified. A Peugeot car won with his petroleum-powered vehicle at an average speed of 12 mph (20 km/h); when the judges of this race handed the trophy, they thanked the manufacturer by saying that he "turned petroleum or gasoline fuel

into a practical solution". Petroleum-based cars became standard, and the other technologies' investigations and evolution became the second priority.

With research drifting away from electric engines and electric energy storage, the advances in these fields have been punctual and mainly conducted by small groups of investigators. The recurrent investment in petroleum-based engines generated a technological advantage over other technologies, which made it economically useless to investigate them for a short or mid-term return.

More than 120 years later, thanks to the continuous evolution of petroleum-based engines, there is no cost-effective alternative to substitute current petroleum cars.

The combustion of fossil-based fuels is the leading cause of global warming and the greenhouse effect consequence of the CO₂ emissions [2]. To mitigate the impact of climate change is essential to seek alternative energy sources of fossil fuels with comparable power capabilities.

For the proper energy solution, three stages are required a) clean energy sourcing, for instance, windmills, solar panels, or geothermal energy are clean energy sources; b) energy storage and transport via energy reservoirs such as tanks or batteries with no energy losses over time and finally c) clean and efficient transformation into the energy type required, mechanical torque, heat or others.

Storing and converting energy into electricity to deliver the required power is challenging, especially in devices with restricted weight or volume. The *hydrogen society* proposes a cycle where energy is sourced via clean methods and converted into Hydrogen (H₂) via electrolysis in a clean end-to-end process. Later, the H₂ is stored in tanks or transported via pipelines into the transformation point where it is converted into electricity using *fuel cells*.

Hydrogen fuel cells provide a complete solution to fossil fuel engine pollution with comparable power capabilities. Fuel cells are electrochemical devices that use H₂ and O₂ to generate electric current. Some types of fuel cell technologies can be used in a wide range of applications with different power needs.

Hydrogen can easily be obtained by hydrolysis using electricity from renewable sources such as the sun or wind. Nowadays, only 5% of H₂ is obtained by this

method, and about 95% is obtained using natural gas or petroleum-based sources [3]. The hydrogen can be stored in high-pressure tanks or in liquid form for later use, converting it into electricity using fuel cells.

The automobile industry is a clear example of how fuel cells, in combination with other technologies such as the improvement of electric motors' power efficiency, compactness, and cost, will contribute to the change of power source and technology.

Low-temperature polymer electrolyte membrane fuel cells (PEMFCs), also called proton exchange membrane fuel cells, are key in the Hydrogen society model since they obtain high energy electricity conversion efficiency by operating at temperatures below 90°C. At present, PEMFC technology is in the commercial deployment phase. However, some aspects, such as durability and robustness, must be optimized.

1.2 Objectives

This thesis dissertation aims to analyze the temporal and spatial uniformity of PEM fuel cells as a function of design and operating parameters analyzing the simulation results of a developed dynamic 3D model. The uniformity of the fuel cell behavior is a determining factor in its durability and robustness.

In order to fulfill this objective, the thesis has been divided into three sub-objectives, as described below.

1. Model and simulation procedure development:

Develop a 3D dynamic PEM fuel cell model and long-term simulation procedure with low computational effort to represent the cell's most important phenomena, such as the fluid-dynamic behavior of water in the liquid and vapor phase, together with the feed gases at the anode and cathode. To analyze spatial and temporal uniformity, the model must also be able to represent the spatial distribution of species and current density as well as show their dynamic behavior. This model and the simulation procedure will allow the study of the setup parameters to optimize the uniformity of the cell performance via extensive simulation.

2. Model validation with experimental data:

Two different sets of experimental data have been used for the model validation. The first experimental data set corresponds with a single serpentine cell operating under low humidification conditions [4]. The cell was re-humidified via water droplets inserted in the anode flow field. Neutron imaging allows the evaluation of the water distribution in the cell. The second experimental data set corresponds with a study of the anode and cathode humidification states applied in a 23-parallel serpentine channel cell. This thesis uses experimental data from a segmented cell [5] tool to measure the current density distribution.

3. Study of experimental and design parameters impact the cell's uniformity:

A systematic analysis of the design and operating parameters of the cell will be conducted to evaluate the setup parameters that optimize the spatial and temporal uniformity of the cell performance through the simulation of the developed model.

1.3 Dissertation structure

This thesis is structured as it is described:

Chapter 1 Introduction, objectives and structure: An introduction to the contents of the thesis document and its structure is presented to facilitate its reading.

Chapter 2 Fuel cell introduction: This chapter briefly introduces fuel cells' history and the main cell types. Also, a brief introduction to PEM fuel cell, its main characteristics, and the significant challenges associated with its commercial viability are shown.

Chapter 3 PEM fuel cells introduction: This chapter focuses on introducing the PEM fuel cell, which is this thesis's key element of study. The internal and auxiliary parts of the PEM fuel cells are described to have a complete

vision of the fuel cell system. Finally, a brief description of the PEM fuel technology challenges is presented.

Chapter 4 PEM Fuel cell modeling: This chapter shows the different types of PEM fuel cell model classifications and reviews the literature on the different types of models. In addition, the challenges in which PEM fuel cell modeling is used to provide knowledge and improve cell development are described.

Chapter 5 Modeling hypothesis: This chapter shows the model developed for studying spatial and temporal uniformity. The chapter presents the submodels that compose the complete model and the equations defining the physical phenomena described.

Chapter 6.1 Numerical implementation and simulation procedure: For simulation optimization, the submodels are decoupled. The variable interaction between submodels is explained in this chapter. The simulation procedure, oriented to improve the computation time, is also shown.

Chapter 7 Model experimental validation: In this chapter, the model is validated with two different fuel cell experiments. The chapter shows how the model has been validated from the dynamic perspective, which is suitable for evaluating the temporal stability of the cell and spatially for analyzing the homogeneity of the cell.

Chapter 8 Analysis of simulation results: This chapter shows the results of the systematic long-term simulations of the model for different experimental and cell design configurations. The impact analysis of these parameters in the performance uniformity of the cell is shown in this chapter.

Chapter 9 Conclusions and future work: Lastly, this chapter shows the conclusions of this thesis and proposed future work.

2

Fuel Cell Introduction

Contents

2.1	Introduction	7
2.2	History of fuel cells	8
2.3	Types of fuel cells	10
2.3.1	Alkaline fuel cells (AFC)	10
2.3.2	Phosphoric acid fuel cells (PAFC)	11
2.3.3	Solid oxide fuel cells (SOFC)	12
2.3.4	Molten carbonate fuel cells (MCFC)	13
2.3.5	Direct Methanol fuel cells (DMFC)	13
2.3.6	Reversible fuel cells (RFC)	14
2.3.7	Polymer electrolyte membrane (PEM)	15
2.3.8	Conclusions	16

2.1 Introduction

The focus of this chapter is an introduction to fuel cells, showing a brief historical review from the first steps to the current state of the art. Moreover, the different fuel cell types are reviewed, highlighting their main advantages and disadvantages. Finally, and to conclude the chapter, a review of the main challenges of the PEM fuel cells is presented to focus the investigation shown in this thesis.

2.2 History of fuel cells

In 1800 Sir Anthony Carlisle and William Nicholson [6] discovered water electrolysis which consists of obtaining hydrogen (H_2) and oxygen (O_2) from water using electric energy.

During 1838-1839, Sir Willian Robert Grove performed the first scientific research regarding fuel cells. Grove described the hydrogen fuel cell concept by immersing two platinum electrodes in a sulphuric acid solution in two separate ends and observed a current flow between the electrodes [6].

In 1893, Friedrich Wilhelm Ostwald related the chemical and physical reactions to explain how Grove's gas battery worked and how the different components of a fuel cell are interrelated. This understanding of the physics of the gas battery led William W. Jacques in 1896 to the first applicable fuel cell [7].

Later, Ludwig Mond and Carl Langer redefined Grove's fuel cell by creating porous electrodes similar to the current fuel cell designs. Mond and Langer were the first to use the terminology *fuel cell*. For their experiments, they used industrial coal gas [8], obtaining 2-2.5 A current density with a cell's area of 700 cm^2 and 0.73 V voltage. As observed on the performance parameters obtained by Mond and Langer, the limitations were huge, mainly due to gas leaks [8].

In 1910 Emil Baur plotted the polarization curve, which showed the relationship between voltage and current density of a fuel cell [9]. Later in the 1920s, Emil Baur developed a molten carbonate fuel cell, and William W. Jacques created the first 1.5 kW fuel cell and later developed another fuel cell of 30 kW. During the early 1930s, Thomas Francis Bacon developed a fuel cell that converted air and hydrogen into electricity; his early work was in Alkaline fuel cells with nickel electrodes working at pressures near 200 atm.

During the 1950s, Polytetrafluoroethylene, more known by the commercial name Teflon developed by DuPont company, began to be used in fuel cells as it helped remove water from within the cell.

It was Thomas Grubb in 1955, working by General Electric (GE), who modified the original designs to the current concept of cells by using an ion-exchange polystyrene sulfate electrolyte as a membrane. Also, during this period, another chemist in GE, Leonard Niedrach, developed a technique for platinum deposition into the membrane, which acts as a catalyst for the reactions [6].

It was in 1959 when Bacon, in collaboration with Marshall Aerospace, presented a 40 cells stack fuel cell with a 5 kW power capacity and an efficiency of 60%. Later, a bulldozer used a fuel cell compound of 1008 cells, generating 15 kW.

From 1950-1960, when fundamental advances were made, fuel cells started to take the attention of the scientific and industrial world, and multiple investigations started to happen worldwide. Recently, multiple companies have been working on fuel cell for stationary systems and transport vehicles.

The high power density of fuel cells compared with batteries make the fuel cells attractive for the automotive market [10]. Multiple automotive manufacturers are developing fuel cell-based vehicles. Honda, in 2021, produced the Clarity model, with a power of up to 175 PS with about 700 km of autonomy. Toyota, since 2013, has been making the Tucson model, with 136 PS with up to 600 km of range. Other car manufacturers, such as Toyota, produce the fuel cell-based Nexo (2018) or Mirai (2021). Not only automobiles are produced using fuel cell technology, but also Xiaomi is working on a fuel cell motorcycle.

Although automobiles are the most common example of fuel cell usage, other applications, such as home electric generators, have been developed. In early 2021 the first domestic hydrogen battery (electric storage plus fuel cell) was presented, triplicating the capacity of Tesla's Powerwall 2 [11].

The importance of fuel cells and their interest is growing fast as more commercial applications arise. A clear example of this growth is the number of patents published in the field; from 2007 to 2014, the number of patents has been duplicated over passing the 500 patents [12], marking a landmark in the transition to the hydrogen society.

The applications of fuel cells are multiple, and there are different types of fuel cells that better fit specific applications. The following subsections provide an overview of the most-known fuel cell types.

2.3 Types of fuel cells

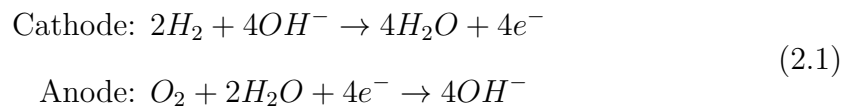
Since Grove developed the first fuel cell, other implementations using different chemical compounds have been created. In the following subsections, a quick review of the different fuel cell technologies will be performed, comparing each technology to the polymer electrolyte membrane fuel cells (PEMFC).

2.3.1 Alkaline fuel cells (AFC)

The AFC is a type of fuel cell that converts H_2 and O_2 into electricity using an alkaline solution such as potassium hydroxide (KOH) separating two electrodes [13].

The early developments in AFC were in the late 1890s [14]. Later, in the 1930s, Francis T. Bacon started working on increasing the effective area of the electrode via the introduction of porous sintered electrodes. Twenty years later, in the mid-1950s, the first commercially viable fuel cell of 6 kW working at 41 atm of O_2 producing 240 A at 24 V was implemented on a forklift truck [15]. The AFC was widely used by NASA in the Apollo project [16], which helped its development. From 1960 to the 1980s, other fuel cell technologies, such as PEMFC, increased power density and durability, reducing the interest in AFC. Recently, due to the development of Anion Exchange membranes (AEM), the investigations in AFC are re-bumping [15].

The overall reaction of an AFC is represented in (2.1).



The Alkaline fuel cells operate at low temperatures, typically between 23 - 70 °C. The hydrogen kinetic reaction is fast, which reduces the overvoltage. Also, a lower catalyst load is required since the chemical reaction has a higher rate in acidic conditions; therefore, the usage of expensive materials for the catalytic layers can be reduced [13].

On the other hand, the Alkaline fuel cell has a high sensitivity to CO_2 . The oxidant feed has to be controlled to have very low concentrations of CO_2 , which would damage the cell producing K_2CO_3 in reaction with the KOH. Due to this, new researches are focused on replacing the KOH solution of polymer electrolyte membranes [17]. As a consequence of the sensibility of CO_2 , this technology is mainly used for space applications, where pollution is smaller or controlled.

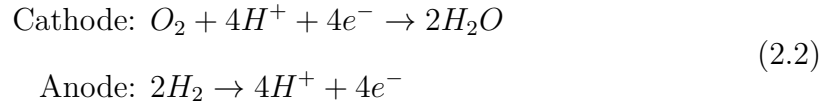
Typically, the AFC has an efficiency range from 30-80% [18]. The power density reaches $150 \text{ mW}\cdot\text{cm}^{-2}$ with implementations from 70 W to 6 kW [19].

2.3.2 Phosphoric acid fuel cells (PAFC)

The PAFC is a fuel cell that converts H_2 and O_2 into electric power by using phosphoric acid compound (H_3PO_4) over a silicon carbide matrix to separate the electrodes [20].

G. V. Elmore and H. A. Tanner, in 1961, performed the first phosphoric acid fuel cell experiments. They used a 35% phosphoric acid and 65% silica powder over a carbon-coated Teflon gasket [21]. Despite the early phases, those developed cells could last up to 6 months without deterioration. During the 1950s and 60s decades, General Electric attempted to develop a PAFC which used conventional hydrocarbon fuel [22].

In 1967, the TARGET international program developed a combined heat and power co-generation power plant for small home residences. Thanks to the TARGET program, PAFC could scale the production of the graphite used in the cell and the development of the bipolar plates. But commercial implementation failed as no cost-effective solution was found. The Japanese company Toshiba designed 11 MW PAFC for TEPCO company, which worked more than 23000 h since 1991, but it had to be operated at lower power than expected due to its instability. Nowadays, other companies commercialize phosphoric acid fuel cells for residential such as the FP-100, which produces 100 kW of power [23].

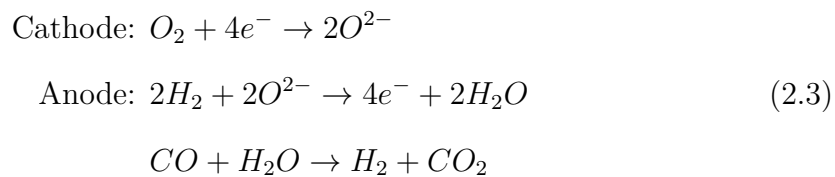


PAFC fuel cells are capable of tolerating any concentration of CO₂ and CO concentrations up to 1.5% but require pure hydrogen. Therefore an external reformer is required [24].

PAFC working temperature typically ranges from 150-200° C with a power density of 130 mW·cm⁻². The electric conversion efficiency is between 35-45%, but used with combined heat and power (CHP), the efficiency can reach up to 80% [24].

2.3.3 Solid oxide fuel cells (SOFC)

The SOFC technology uses solid oxide as an electrolyte. Those cells are fed by hydrogen and oxygen (in the form of air). The SOFC cells operate at high temperatures taking advantage of the heat waste. The energy co-generation presents SOFC as a green technology [25, 26]. SOFC was discovered by E. Baur and H. Preis in the 1930s while using La, W, Y, Zr, and Zr oxides. The interest in SOFC took off after Carl Wagner in 1943 related the electric conductivity of mixed oxides to the presence of oxygen vacancies. In the 1980s, Westinghouse Electric corporation produces SOFC from 5 to 250 kW [27, 28].

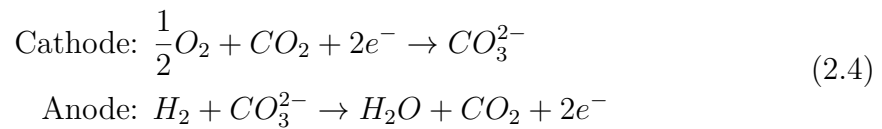


The SOFC operating temperature is typically between 800-1000 °C. Due to its high temperatures, Pt is not required to catalyze the reaction [25, 29], and it is CO tolerant. The SOFC requires a long-startup time to reach the operating temperature moreover, high-temperature alloys and ceramics must be used to sustain the operation without aging. Solid oxide fuel cells typically have a power density within 300-600 mW·cm⁻² with implementations of around 1-250 kW [30]. Its efficiency is usually calculated with a co-generation system, so it reaches beyond 60% [31].

Currently, a new variant of Solid oxide fuel cells is being developed. The PC-SOFC (Proton-conduction SOFC) transports protons instead of oxygen ions, allowing much lower working temperatures.

2.3.4 Molten carbonate fuel cells (MCFC)

An MCFC bases its working principle on the carbonate ions transfer from cathode to anode. The technology is similar to SOFC but uses molten carbonate on a ceramic matrix as electrolyte [32]. One important characteristic is that this type of cell can generate electricity directly from hydrocarbon-based fuels such as natural gas, which also is a significant inconvenience in the sense of environmentally friendly technology. During the 1960s, the interest in MCFC technology arose instead of SOFC due to its lower temperature operating point. Companies such as General Electric, the United Technology Corporation, and the Institute of Gas Technology started developing projects for MCFC, studying the material selection to work on the operating temperatures of MCFC.

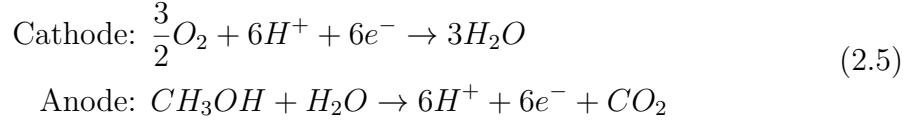


MCFCs are highly reliable thanks to their tolerances to CO₂. However, although hydrogen is used as a fuel is not considered a purely green technology since they produce CO₂ as a product. MFCF efficiencies are around 60-70% [24] with a power density within the range of 130 mW·cm⁻² with implementations from 300 W to 3000 kW [33]. The MFCF operating temperature is typically above 600 °C.

2.3.5 Direct Methanol fuel cells (DMFC)

The DMFC is a fuel cell that converts CH₃OH in liquid form into electricity by using a composed phosphoric acid membrane, Nafion. During the 1960s, the research was mainly focused on the active anode components since methanol oxidation was the limiting reaction of the cell performance [34]. Commercially, the direct methanol fuel cells compete with Li-ion batteries in small portable devices as they meet

similar power requirements with much lower volume [35]. Small vehicles for material handling or low-weight automobiles such as scooters have been developed using DMFC since 2005 with power ranges from 0.5 to 6 kW [36].

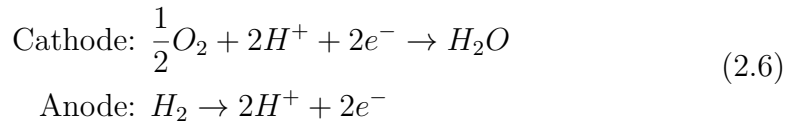


DMFC operates at low temperatures, between 30-130 °C, which makes it suitable for portable devices. These fuel cells use liquid fuel instead of gas, making it easier to store [37]. Low concentrations of methanol are used to avoid methanol cross-over, which decreases the efficiency significantly. Moreover, the slow anode chemical reaction and the inefficient reaction in the cathode reduce the overall performance to efficiencies of 30-40% despite the theoretical efficiency being around 97%. Typically the power density of the DMFC is from 200-300 mW·cm⁻² [38].

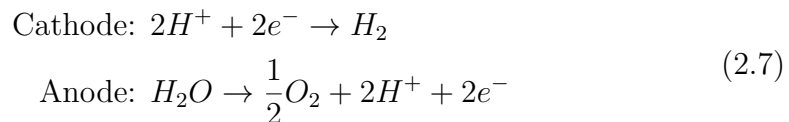
2.3.6 Reversible fuel cells (RFC)

An RFC can operate efficiently in electric power generation and electrolysis modes. The RFCs may be based on SOFC, PAFC, or other technologies [39]. In this case, we will focus on PEM RFC [40]. A reversible fuel cell has two operating modes a) the current generation when fed with O₂ and H₂, Eq. (2.6), and b) the electrolyzer mode, which is connected to an external electric supplier and water fed in the anode produces H₂ in the cathode, Eq. (2.7), [41]. The two reactions can be observed as follows:

1. Electric power generation mode.



2. H₂ production mode (electrolyzer).



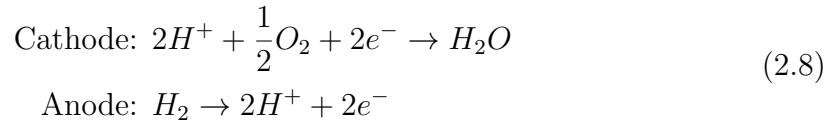
The PEM RFC uses the same type of membrane as the PEM fuel cell, which consists of an MEA formed by two GDLs, two catalyst layers, and a perfluorosulfonic acid membrane known by the commercial name Nafion.

RFCs are cells that can be used as rechargeable batteries thanks to their reversibility which, combined with the compact design, are suitable for usage in aerospace applications. The reversibility of the cell limits the operational point, trading off performance to ensure durability.

The efficiency of PEM RFC in generation mode is around 30-40% with current densities of $1 \text{ A}\cdot\text{cm}^{-2}$, which is lower than the PEMFC. In reverse mode, the efficiency is around 70% with a current density demand of $0.5 \text{ A}\cdot\text{cm}^{-2}$ [41]. On the other hand, the SOFC RFC has an efficiency around 60% [42] with power densities higher as $480 \text{ mW}\cdot\text{cm}^{-2}$ at $800 \text{ }^\circ\text{C}$ [43].

2.3.7 Polymer electrolyte membrane (PEM)

The PEM fuel cell, or PEMFC, converts hydrogen and oxygen into electric power using a perfluorosulfonic acid membrane (also commercially known as Nafion) as an electrolyte. The membrane is composed of a polymer with excellent mechanical properties that make it suitable for assembly with the rest of the cell components. The membrane allows the conduction of protons and liquid water, but the crossover of gases between anode and cathode is considered practically negligible for small membrane thicknesses. The polymer of the electrolyte is hydrophilic, and for proper conductivity, it must be well-hydrated [44].



PEMFC are typically in the range of $500 \text{ mW}\cdot\text{cm}^{-2}$ operating between $40\text{-}80 \text{ }^\circ\text{C}$. With the high power density obtained, the stack cell is typically smaller compared with other technologies, which are suitable for transport vehicles. PEM fuel cells have a theoretical efficiency of 63%, but practical implementations reach up to 37% due to heat loss on the cell. The low operating temperature makes gas humidity play

an essential role in cell performance. Water condensation in the feeding channels may produce flooding from liquid droplets. Some PEMFCs are designed to work at higher temperatures to reduce the impact of humidity, working in the range from 120-200 °C. The platinum used as a catalyst in the electrochemical reaction in anode and cathode can capture CO. Small concentrations of CO (over 10 ppm) can poison the catalyst and significantly reduce the cell performance [44]. PEM fuel cells, especially the low-temperature cells, are deeply described in chapter 3, as they are the type of cells under study in this thesis.

2.3.8 Conclusions

This chapter presents a brief review of the history of fuel cells, from the first gas battery to the latest concept and implementation of fuel cells in modern vehicles.

Also, an overview of the different types of fuel cells and their chemical reactions have been presented to contextualize PEM fuel cells' properties and compare them. Next chapter, 3.2 describes in detail the PEMFC as it is the focus of the thesis.

3

PEM fuel cells introduction

Contents

3.1	Introduction	17
3.2	PEM fuel cell components	18
3.2.1	Membrane-Electrode Assembly (MEA)	19
3.2.2	Bipolar plates	24
3.2.3	Flow field	25
3.2.4	Cooling plates	27
3.2.5	Auxiliary components	27
3.3	PEM Fuel cell technology challenges	29
3.3.1	Technological challenges	30
3.3.2	Economical challenges	31
3.3.3	Material cost	31
3.3.4	Complementary operations	32
3.4	Conclusions	34

3.1 Introduction

This chapter is divided into two sections which describe the components of the PEM fuel cell and the main challenges PEMFC still face to become a technologically and economically viable solution for the market.

The PEM fuel cell components section describes the MEA, the bipolar plates, the flow field, and the cooling plates. Also, other parts are not specific or intrinsic to the PEMFC but are required for optimal cell operation.

In the section dedicated to PEM fuel cell technology challenges, a brief description of the most critical limitations of the technology is presented, and a review of the additional operations and components which drive the operative cost of the PEMFC.

3.2 PEM fuel cell components

The PEM fuel cells use a perfluorosulfonic acid (Nafion) membrane as an electrolyte which separates the cathode and anode streams (H_2 and O_2 respectively). Other components of the cell have to ensure an efficient reaction in terms of fuel consumption and current density uniformity, such as the GDL, collector plates, gaskets, and others.

Fig. 3.1 presents a scheme of the PEM fuel cell.

PEM fuel cell is composed of three main parts, which are: a) the cathode collector plate and flow field, b) the Membrane-Electrode Assembly (MEA), which is composed of the gas diffusion layers (GDL), the catalytic layers (CL) and the membrane, and c) the anode collector plate and flow field. The cell usually has a symmetric structure in the anode and cathode, as shown in Fig. 3.1.

Each of these components has multiple functions and some specific requirements. In the following sections, a brief introduction of each component and the functionalities and requirements are presented.

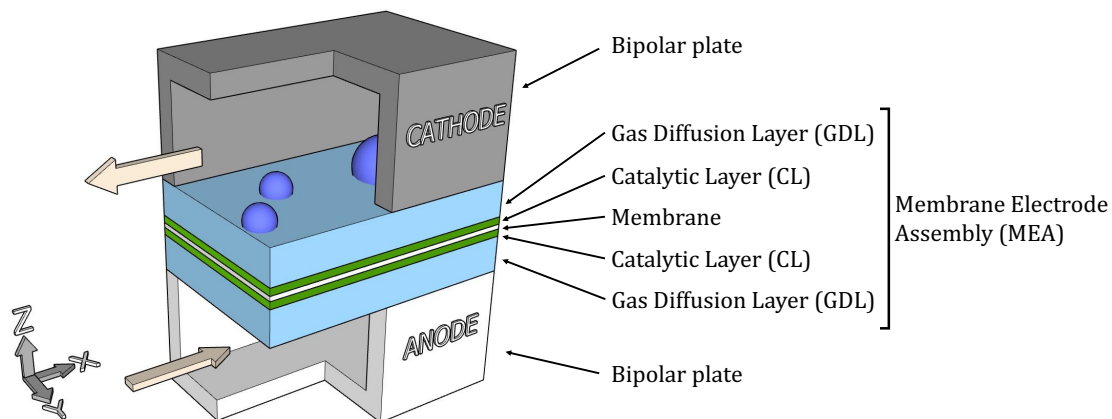


Figure 3.1: PEM fuel cell components overview

3.2.1 Membrane-Electrode Assembly (MEA)

The MEA is one of the most critical components in the fuel cell as it determines the overall cell performance and durability [45]. Despite having a symmetric distribution of components, the thickness of each may vary depending on the cathode or anode, mainly due to the different content of Pt [46]. The assembly of the MEA components, which have different mechanical properties, and the surface deposition of the catalytic layers, is a highly complex task that can condition the durability and robustness of the cell operation. The manufacturing control of the MEA is a significant challenge since each component of the MEA thickness has to be adequately controlled to ensure uniform behavior of the cell. As a consequence, to ensure such precision, the production cost of the MEA is highly relevant in the overall fuel cell DMC, mainly driven by the catalytic layer and the usage of precious materials such as Pt [47]. In Fig.3.2 an SEM image of an MEA extracted from [48] is presented.

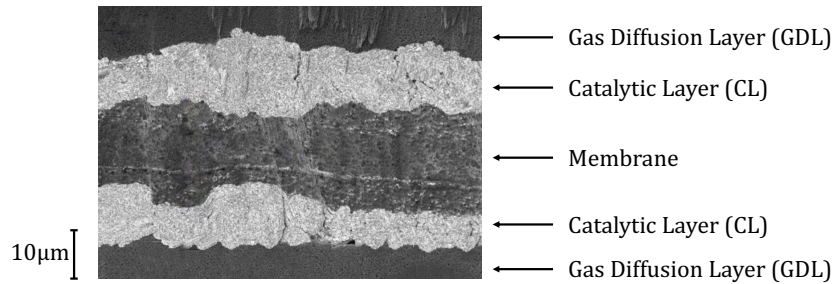


Figure 3.2: SEM image of PEM fuel cell MEA [48]

In the following sub-sections, each component of the MEA is explained.

Gas Diffusion Layer (GDL)

The GDL is located between the collector plate and the catalytic layer (Fig. 3.1) to distribute the gases into the catalytic layer uniformly and remove the produced liquid water appropriately. The GDL has five main functions:

1. Enable gas flow from the channels to the active areas of the catalytic layers. Porous media materials are used to fulfill this purpose.

2. Enable liquid water to be expelled from the catalytic layer to the channel, especially from under the rib zones of the flow field. Water removal from the GDL is required since excess water content in the GDL will reduce the access of reactants to the CL. To properly evacuate liquid water, two material properties have to be taken into account: a) the porous size to avoid water clogging inside the porous media [49] and b) the surface hydrophobic treatments. PTFE, as an example, is used to facilitate the removal of water [50].
3. Enable electronic conduction from the catalytic layers to the bipolar plates. The GDL is an undesirably electrical resistor in serial to the system. High electrical conductive materials such as carbon [51], or metallic foams are used to minimize this drawback.
4. The GDL has to be thermally conductive for efficient dissipation of the heat generated in the cell. A PEM fuel cell has four sources of heat: a) the Joule effect due to the electric resistance of the components, b) the heat released by the half-reactions, c) the electrochemical activation reactions, d) the water sorption and desorption, and e) the phase change from liquid water to steam [52].
5. The GDL helps to provide mechanical consistency to the overall MEA. The thickness of the membrane, typically around 25-50 μm , is usually subjected to a differential gas pressure between the anode and cathode. For this reason, the GDLs, with thicknesses of 100-300 μm [53], to support the membrane homogeneously, preventing its rupture. In addition, GDLs provide structural support to the MEA to resist the mechanical stress to which it is subjected in cell assembly [54].

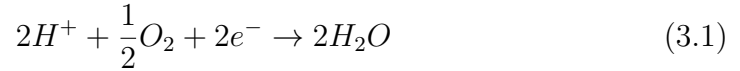
The proper balance of each requirement is essential for the cell's overall performance. For example, the pore size of the media has to be selected tightly to avoid creating water droplets inside the GDL, but it has to be sufficiently wide for gases to flow. The manufacturing process has to be adequately adjusted, as it could impact

the ohmic resistance of the GDL [55]. GDL thickness has to be balanced according to the material stiffness, the electric conductivity, and the capacity to expel water.

Catalytic layers (CL)

The catalytic layer is located between the GDL and the membrane (Fig. 3.1). There are two different CLs, the anode and the cathode CLs. The CL is the active surface where the electrochemical reactions occur:

1. In the cathode catalytic layer, the protons (H^+) that crossed the membrane react with the oxygen (O_2) supplied from the flow field that crossed the GDL and the electrons that close the electric circuit from the anode producing water Eq. (3.1).



2. In the anode CL, the H_2 is decomposed into protons (H^+) and electrons (e^-). The protons cross the membrane to reach the cathode CL. The electrons flow from the anode CL through the GDL, the anode bipolar plate to the electric load, the cathode bipolar plate, GDL, to finally reach the cathode CL Eq. (3.2).



Typically Platinum is used as a catalyst in PEMFCs and is formed of small particles supported by carbon powder [56]. The superposition of Pt over carbon powder reduces the required amount of Pt which reduces the cost of the MEA while maintaining a large active area. In order to reduce cost, other materials can be used as catalysts. Iridium (Ir) is typically used as a catalyst in PEM fuel cells; both are rare and expensive materials on earth. Alternative compounds such as molybdenum disulfide (MoS_2) are investigated to reduce the cost of the CL [57].

The design objectives of the catalyst layers are:

1. To use adequate carbon support to reduce the amount of platinum while increasing the access of the reactant to the active area [51]. Typically, the thickness of the catalyst layer is from 10-17 μm for the anode and between 15-30 μm for the cathode [58].
2. The fuel must be able to reach the active areas of the CL, and the produced liquid water must be drained so as not to block the flow of fuel gases. In some cases, catalyst patterns have been designed to facilitate fuel access, proving a cell performance improvement [59].
3. In the active area, where the reaction occurs, the catalyst and the support material should provide the lowest electrical resistance and the right electric contact with the GDL, efficiently collecting the electrons.
4. To efficiently dissipate the heat generated, the CL has to be a good thermally conductor.
5. The component must be mechanically robust. CLs are very thin but should sustain differential pressures and avoid breaking and prevent the drag of the catalytic element caused by the flow of the different species.
6. Most of the CL are manufactured using Pt which is very sensitive to CO_2 concentration on the gases. To increase the chemical robustness to pollutants, the Pt is typically mixed with other components to create a Pt alloy. Alloys with Ni to form Pt_3Ni have been studied to improve durability. Other alloys with Fe or with Zr (Pt_4ZrO_2) also produce similar durability increase results [60].

Membrane

The main objective of the membrane is to allow the flow of protons. Controlling the hydration of the membrane is essential since its conductivity depends on the water load in the electrolyte. To facilitate the proper hydration, the polymer membrane is usually composed of a fluoro 3,6-diozo 4,6-octane sulfonic acid (Nafion) with a PTFE

treatment, which provides the hydrophilic property [61]. The proton conductivity of the membrane is highly related to its humidification and, consequently, the overall performance of the cell [62].

The proton conductivity depends on two main phenomena:

1. Vehicular mechanism. By this mechanism, the H_3O^+ diffuses through the aqueous medium because of the electrochemical difference, considering water as a proton carrier.
2. Proton hopping. Also called the Grotthuss mechanism, it is a phenomenon in which the protons, H^+ , are transferred by consequently moving over hydrolyzed ionic sites SO_3^+ and H_3O^+ . Its contribution to Nafion conductivity is considered low [61, 63].

Despite the protonic conductivity, there are other important requirements the membrane must fulfill. The membrane's main functions are:

1. To separate reactant gases from the anode and cathode (avoiding the crossover) as undesired chemical reactions on the cell reduce the efficiency. Therefore, the membrane must adequately isolate the anode and the cathode gases to ensure only protonic flow. Gas crossover can be significant if the membrane thickness is very thin.
2. The membrane has to be thermally conductive to dissipate heat efficiently.
3. The membrane must be an electrical insulator to avoid electric short circuits.
4. The membrane must be water-permeable to enable the flow of liquid water.

To increase the membrane's proton conductivity, the thickness is reduced, around 25 to 50 μm [61]. The membrane's life longevity is highly related to the transient and uneven operating working points along the cell. The membrane thickness has to balance the durability, the fuel crossover, and the electric conductivity [61].

3.2.2 Bipolar plates

Bipolar plates have multiple purposes and are one of the most expensive components. The plates are located between the MEA and the end plates, as shown in Fig. 3.3, where the flow field is machined or stamped. Due to the flow field design entity, its importance and the different standard designs are described in the following sub-section 3.2.3, focusing this section on the general properties of a bipolar plate.

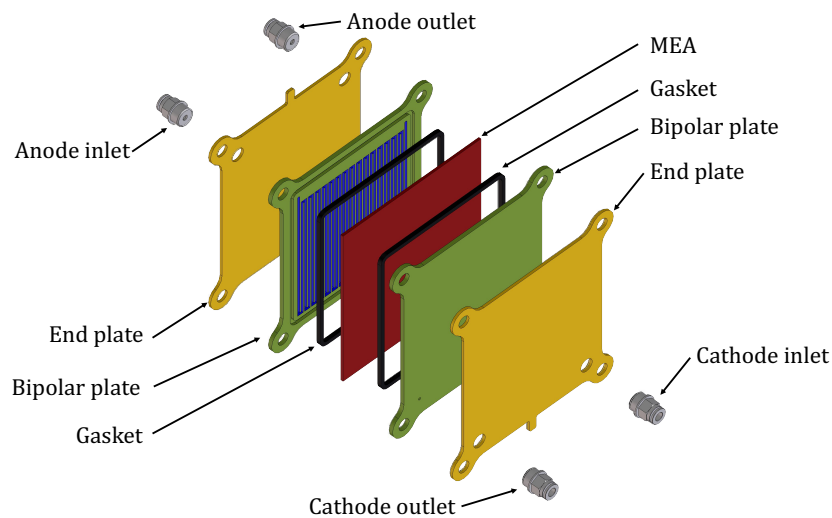


Figure 3.3: Conceptual design of a PEM fuel cell with its components

The bipolar plates functions are:

1. Support the flow field design of the channels to adequately remove the water generated by the chemical reaction [64] and properly distribute the gases.
2. Provide thermal dissipation using heat-conductive materials to avoid uneven aging of the components. In stacks cells device, cooling channels are added over the plates on high-end applications to evacuate heat uniformly.
3. Electrically connects the different individual cells of the stack.
4. The water is slightly acidic ($\text{pH} \approx 5$), and corrosion may occur due to the flow of electrons. To be chemical compatible, passivization surface treatments are typically applied to reduce corrosion effect [65]. Also, protective coatings are applied to protect bipolar plates from corrosion. Treatments or alloys

with Cr, Mo, and Ni show increased corrosion resistance values, similar to the gold-plated bipolar plates. In stainless steel (SS) bipolar plates, it has been demonstrated that higher Cr compositions improved corrosion resistance. Surface treatments with TiN depositions have been proven to increase corrosion resistance in 316L SS [65, 66].

5. The bipolar plates have to be non-permeable to gases.

In high-value applications, where cost plays a secondary role, bipolar plates are typically made of graphite or a combination of multiple materials to reduce the cost by creating corrosion-protective coatings over a copper conductive plate [67]. For other applications, carbon polymer composites or metal stamping, using stainless steel (SS) for non-coated plates, is used to meet the cost requirements. When surface treatments or coatings are considered, other materials such as aluminum are taken into account, those coatings are mainly carbon-based, or metal-based [64].

3.2.3 Flow field

The flow field design is crucial to properly distribute the gases along the cell and adequately remove the liquid water. The flow field design is an active research topic [68, 69, 70, 71] since it has a significant impact on the life longevity of the cell.

There are multiple types of flow field designs; the most common are:

1. Serpentine design. Single serpentine mode, or multiple parallel serpentes, is the most used configuration. This design ensures high gas speed in the flow field, which is helpful for water removal, but its length produces a high-pressure drop which causes higher non-uniformity [72]. Moreover, long channels produce gradients of RH and fuel concentrations, which cause uneven working conditions.
2. Parallel straight channels design. This flow field is conformed of multiple straight channels in parallel. As the channels are straight, the gas path is shorter than serpentine designs but requires a higher number of channels. Therefore gas speeds and pressure drops are lower for the same stoichiometry

ratios. The lower gas speeds may reduce the capacity of liquid water removal by droplet dragging, which increases the probability of clogging and deactivation of certain cell areas.

3. Interdigitated designs. Contain dead-end channels. Reactant gases are directed to flow under the rib, inducing high-pressure drops. Liquid water evacuation is compromised because the liquid must cross large volumes of the GDL in order to be extracted.
4. There are other possible channel designs; among them, it is worth mentioning the a) pin flow field design which consists of multiple punctual contact points with the MEA, typically in a structured shape. This design intends to uniform the pressure along the cell; b) bio-inspired designs which propose angled deflectors along a very wide channel [73]; c) interdigitated variations designs such as the Murray, which intend to search for more uniform gas distribution [73]; among others.

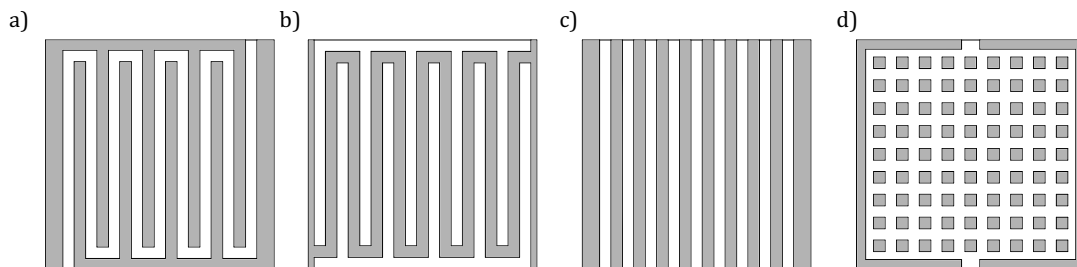


Figure 3.4: Example of some flow field designs (The gray area represents the surface of the bipolar layer resting on the diffusion layer), a) single serpentine, b) interdigitated, c) parallel straight channels, and d) pins designs.

The following properties of flow field design must be considered:

1. Liquid water removal capability by reducing the time of residence of a water droplet inside the fuel cell.
2. Uniformly gas feeding in the overall cell surface to ensure homogeneous pressure and fueling. Uneven working points reduce the expected life of the MEA [74].

- Typically, the MEAs are between 150-250 μm thickness, with support pressure drops and oscillations, which would cause its breakage. Then, the flow field design must avoid uneven pressure areas. To avoid excessive deformations, the MEA has to be sustained tightly, limiting the channels' width.

3.2.4 Cooling plates

The impact of temperature on the overall performance of a fuel cell is not negligible as it impacts the mass and charge transfer and, therefore, in the overall cell voltage [52, 75]. The primary heat sources are the Joule effect due to the electric resistance, the reversible and irreversible heat production on the chemical reaction, and the entropy production rate [76]. This heat has to be removed to enable the cell to operate at a constant and regulated temperature. Controlling the temperature within a range is important to optimize the cell's performance. Three mechanisms allow heat to be removed from the cell, a) the heat capacity of the gases. The gases increase their temperature as they flow, removing heat from the cell, b) the thermal conductivity of the cooling plates, which allows heat to be dissipated to the outside of the cell; and finally, c) the water content in terms of evaporation and condensation as well as water liquid removal from the cells, which reduces its temperature.

Using highly thermally conductive materials on the cooling plates, such as graphite or aluminum, allows the usage of cooling fluids, a gas, typically air, or a liquid, on those plates.

3.2.5 Auxiliary components

In order to complete a PEM fuel cell design, other auxiliary components are integrated to achieve an optimum working device. Those devices are briefly described in the following subsections.

Gaskets

Avoiding gas leaks is vital to ensure overall cell efficiency. Gaskets are components typically installed between the MEA and the bipolar plates to seal and prevent gas

leaks while being an electric insulator. Gaskets are materials that must sustain high working temperatures and chemical attacks. For this reason, typically high-performance silicone rubbers, fluoroelastomers (PTFE), or EPDM are used [77, 78]. The implementation may depend on the stack configuration and must be correctly ensembled with the proper tightening force to ensure it works properly.

Voltage control

To ensure the cell is working at its optimal performance point, it must operate within a range of current and voltage. Each application may have different consumption demands, requiring an electric current conversion. Typically a power converter is used to compensate for power spikes and punctual current demands. A DC-DC boost converter is used for such applications. Boosters are the most common solution to set a constant voltage at the cell's output for later usage.

Current consumption is commonly used in AC mode. Therefore, an extra device to convert DC-AC, an inverter, is installed.

Good power electronics management is important since non-adequate design will decrease the overall efficiency of the fuel cell. Typically the power converter devices have an efficiency of 85%.

Temperature control systems

In a PEM fuel cell, both semi-reactions are exothermic. Moreover, the current flow generates heat due to the Joule effect as well as the overvoltages which are also heat generators. An increase in temperature may cause membrane dehydration which is an undesired effect. The cell temperature control systems are installed to keep a controlled and steady temperature. Those devices have two main functions a) ensure a fast start-up process to reach the working regime in the shortest time possible, which may require heating the cell, and b) remove heat to prevent the cell from operating at undesired temperature. Typically, an external device controls the temperature of a fluid, gas, or liquid, which is used as a coolant for the cell. The cell has cooling channels on the bipolar plates or an intermediate plate between

two stacks of bipolar plates, which are used as coolant channels. The cooling and the electric efficiency are improved if the intrinsic contact resistances are removed.

Developing a proper and homogeneous cooling plate and thermal profile reduces the non-uniformities on the membrane surface.

Humidifying devices

Humidifiers are devices capable of introducing water steam or mist in a gas to control water content. Those devices ensure minimum humidification in the cell to maintain the membrane sufficiently hydrated [79].

Humidifiers are not typically used in commercial applications and are used mainly in lab test beds to produce very controlled environments for development. In commercial applications, typically self-humidifying systems are used. The self-humidifying PEM fuel cells use additives to increase the retention properties of Nafion [80]. The first self-humidifying fuel cell was conceptualized in 1996 [81] using silica or titania additive to the Nafion membrane. High proton conductivity additives are added to the membrane for self-humidifying fuel cells to operate in low-humidifying conditions.

Gas storage and conditioning

The PEM fuel cells require a specific working pressure for each gas. This pressure is obtained by using gas compressors which increase the pressure of the gas. Typically the gas is compressed and stored in high-pressure tanks for later usage. The high-pressure gas tank has the advantage of reducing the volume for mobile devices while enabling excellent control of the flow and pressure by regulating the aperture of the tank outlet valve. Using compressed gas reduces the overall efficiency of the hydrogen cycle since the energy consumption during the compression has to be considered.

3.3 PEM Fuel cell technology challenges

Fuel cells, especially PEM fuel cells, present a competitive alternative to fossil fuel engines for transport vehicles and other devices requiring high autonomy at

low weight with small storage space. As an example, the H₂ is stored in a small container in Mercedes Benz GLC-F-CELL to have an autonomy of 437 km with 4.4 kg of H₂ in an approximate 100 l tank [82].

But to access broader markets and become an accessible and reliable technology, there are multiple challenges to overcome on fuel cells. Those can be categorized into two groups, technological and economic challenges, mainly due to the cost of the components [83].

The economic and technological barriers are linked. To reduce the cost of the components, they have to be evaluated, and their technical feasibility demonstrated. Some current technical issues to overcome are typically solved by adding extra elements to the overall system.

The following subsections present a brief review of the different issues fuel cells present to deploy a reliable, economically competitive solution.

3.3.1 Technological challenges

The technological viability is mainly focused on the durability of the components, especially the membrane. The membrane degradation is widely studied [84, 85, 86, 87].

The main causes of membrane degradation are:

1. Mechanical failures of the MEA produced by multiple phenomena. In the same xy surface of the cell (xy is defined as the GDL plane, check Fig. 3.1 for clarity), the differential pressures between anode and cathode may easily break the membrane since they are very thin, between 25-50 μm . Humidity cycles on the membrane reduce its tensile strength, which may cause its breakage. Finally, manufacturing stability on the thickness and finishing of each component is essential to prevent uncontrolled early failures.
2. Chemical attacks to the membrane by hydroxyl and peroxy compounds produce fluoride release. Membrane manufacturers modified the chemical composition of the membranes to reduce their degradation.

3. Non-adequate feeding of contaminated humidifying water may introduce impurities into the cell. Uneven consumption of O_2 or H_2 , variation of humidification, or different amounts of liquid water along the flow field produces non-homogeneous aging of the cell, which leads to uneven degradation as local current densities are produced.

Non-uniformity of the cell compounds is typically mitigated by the design of the flow field, dimension of the cell, or gas flows. The objective is to keep all the areas of the cell sufficiently fed and remove the liquid water produced to ensure uniform humidification of the membrane.

3.3.2 Economical challenges

The total operation cost of a PEM fuel cell system has two main drivers: the cost of the materials used in the components of the fuel cell itself and the derived from the operation of the fuel cell, such as gas compression, gas purification, and others which has an impact as the metric delivered power per dollar, [W/\$].

In the following subsections, those two topics are going to be briefly analyzed.

3.3.3 Material cost

PEM fuel cells use precious and high-performance materials in the MEA and the bipolar plates to obtain good performance but at high costs. At high-volume manufacturing production, the catalyst in the MEA becomes the most expensive material as it is typically manufactured with Pt as described in section 3.2.1.

There are two main research lines to reduce the cost of the catalyst: a) reducing the amount of Pt used per cm^2 by setting the Pt over carbon surfaces or creating deposition patterns to maintain the active area [56, 59] or b) using alternate materials with similar properties than Pt at lower manufacturing cost [57].

Both lines of investigation must balance the manufacturing cost with the cell's durability and performance. This balance is accounted for not only in the direct material cost (DMC) but for the total cost of ownership (TCO), which is the cost

to generate a certain amount of energy during a defined period of time taking into account maintenance and repairs.

Bipolar plates are another great contributor to the cost of the PEM fuel cell. As described in section 3.2.2 they are made of graphite for high-end applications. Graphite has the advantage of high electrical conductivity and corrosion resistance but is not economically viable for high production due to its high costs. Alternative compounds with stainless steel, surface-treated aluminum, or titanium are investigated to replace graphite with similar electric conductivity and corrosion resistance but reducing cost, reducing the electric resistance, and simplifying the manufacturing process to enable scale to production.

3.3.4 Complementary operations

PEM fuel cell requires to be fed with clean H_2 and O_2 , without pollutants, especially CO. Also, other key parameters in the operation of PEMFC are the stable operating pressure, appropriate relative humidity (RH) of the feeding streams, a controlled operating temperature, depending on the application, compact fuel storage, and, to improve the efficiency, a H_2 recovery system. Complementary operations must be considered to carry out the previous requirements, and the devices to reach these objectives in the fuel cell eco-system must take into account the energy consumption cost, weight, and size of the equipment overall in mobile systems.

CO filtering

Reducing the CO from the hydrogen stream is important, mainly when the H_2 is produced by steam methane reformation, which contains quantities of CO up to 20000 ppm. There are multiple solutions for on-board or offline purification. On-board purification consists of devices that reduce the CO previously to the fuel feeding of the cell. The following three main technologies of hydrogen stream purification are exposed. The Electrochemical Preferential Oxidation (ECPrOx) are devices similar to the PEMFC but operating with potential oscillations which absorb and oxidize the CO into CO_2 [88]. Another electrochemical filtering system

consists of two PEMFCs operating alternatively, absorbing and oxidizing the CO [89]. The third technology is membrane separation is a mechanical filtering system that blocks specific molecules or components. The selection of which components cross the membrane depends on their permeability through a specific membrane; the selectivity [90].

Streams conditioning

Gas streams require certain pressure and humidity to ensure the cell operates within its desired range. Operating pressure can be obtained with pressurized tanks. The tank is filled and pressurized offline. The cell's pressure and gas consumption are controlled by the inlet valve leading to the cell. Gas blowers or inline compressors are commonly used when air feeds the cathode, not being necessary to use air pre-compressed in a tank.

Gas stream relative humidity is relevant to ensure the fuel cell does not dry out or flood during operation. Multiple technologies enable to humidify a gas stream, such as gas bubbling through water, nozzle spray, or membrane humidifiers [91]. Membrane humidifiers are commonly used as they do not require external power to operate; therefore, the cell's overall efficiency is not being impacted.

Hydrogen recovery system

PEM fuel cells are typically supplied with stoichiometry higher than one, meaning more fuel than strictly necessary for the reaction is provided. This excess of fuel, if not recovered and conditioned, is considered waste. If it is not used, this extra fuel decreases the cell's overall efficiency by the stoichiometry factor.

To reduce the inefficiency of fuel waste, the hydrogen recovery systems are reinserted into the fuel cell once the RH is removed from the stream, reducing the overall consumption of fuel and improving the overall performance. Adsorption of RH from the anode gas stream outlet is typically used with materials with water affinity, such as calcium chloride, or by condensing it with a cold trap [92].

3.4 Conclusions

This chapter presents a brief history of fuel cells from the early days. Afterward, an overview of the different types of fuel cells was done, defining the chemical reaction involved in each cell and their main characteristics. Finally, focusing on PEM fuel cells, a brief introduction to the main components of the cell and challenges facing the PEMFCs were explained.

4

Introduction to PEM fuel cell modeling

Contents

4.1	Introduction	35
4.2	Modeling challenges in PEM fuel cells	36
4.2.1	Water management	37
4.2.2	Heat management	39
4.2.3	Fuel feeding	40
4.3	Model classification in PEM fuel cells	41
4.3.1	Dimensional classification	42
4.3.2	Structural classification	44
4.3.3	Dynamic classification	46
4.3.4	Thermal classification	46
4.4	Conclusions	47

4.1 Introduction

This chapter is divided into two sections. First, a description is given of the most critical challenges in the modeling of PEM fuel cells currently being researched. These challenges focus mainly on the characteristics that most limit the performance of the cells or their economic viability and where modeling and simulation can provide valuable information. Secondly, the classification of the models exposed in this chapter will help understand the types of the PEMFC sub-models presented in this thesis, shown in the section 5.3.

4.2 Modeling challenges in PEM fuel cells

The models primarily intend to better understand the process that occurs inside the cell. Information obtained by simulation allows design or operational parameters optimization without requiring physical experimentation. Moreover, simulations allow observing phenomena incapable of being measured in an experimental setup. Those attributes make modeling and simulation very attractive for research. Also, as the capabilities of computers and simulation tools improve, models with higher computational complexity can be simulated.

In the fuel cell field, modeling is mainly focused on three different topics:

1. Water management (subsection 4.2.1). Managing the cell's water content and appropriate distribution is important to keep it constant within the optimum operating range. The cathode catalyst layer half-reaction produces water as a product which is removed through the GDL via evaporation or droplets on the flow field.

Also, properly managing water in the cell allows spatial distribution homogeneously, ensuring the cell's longevity and increasing efficiency.

2. Heat management (subsection 4.2.2). The electrochemical reactions in the PEM fuel cell are exothermic, producing heat. Properly dissipating the heat is vital to keep the cell working in stable conditions.
3. Fuel feeding (subsection 4.2.3). The experimental configuration and the design of the cell must allow the fuel to reach the active layer at the optimum concentration, avoiding starvation or excess fuel that would lower its performance in both cases.

In the following subsections, a description of each challenge is presented.

4.2.1 Water management

Water is the product of the cathode semi-reaction, which is generated in the cathode CL. Water content in the cell must be kept within the optimum operating range to ensure adequate proton conductivity in the membrane and the access of fuel gases into the CLs. As a consequence, a good balance of water content is required. Liquid water must be removed from the GDLs when in excess, typically for removal by evaporation or by dragging liquid water droplets along the channels. At cell start-up, in some experimental configurations is required to supply a specific RH to the feed gas to prevent uneven cell operation. As water is generated in the cathode, typically, the anode is more prone to dry; hence gas humidification is more commonly used in the anode. Phenomena like flooding and drying (both on the anode or cathode side) produce uneven performance. Overall, ensuring the proper distribution of water in the cell plays an essential role in the performance and life span of the PEM fuel cell [93, 94].

The water content in the cell must be controlled tightly. There exist multiple investigations that tackle this problem. The liquid water removal from the GDL depends on the properties of the GDL, such as surface treatments, pore size, porosity, and tortuosity. Commonly the Leverett approximation of the capillary pressure of water inside the GDL is used, but with numerical simulations using a Lattice-Boltzmann approach, a more accurate prediction of the capillary pressure is obtained using finite element VOF (Volume of Fluid) techniques [95].

Aside from phenomenon-specific models, other models are focused on control strategies of water content in the cell. A developed model of the amount of water content in a cell, in [96], consists of a transfer function model that relates the water content against the cell stack temperature and the air stoichiometry. The phase angle of single-frequency impedance was used to control the water content in the cell. The model is later used to propose a close loop function to control the amount of water in the stack using both the cooling temperature and stoichiometry as stack control variables. The results obtained with the simulation have an error to the target of about 3%.

The models used in real-time control must be low-effort computationally. In [97], a 1D complex model was developed and validated for applying order reduction techniques to have a physical representative model with low computational effort. The model has been applied to develop predictive of multiple water profiles controlling gas streams and humidification to ensure adequate water content in the cell.

Much more complex models tackle water management with flow field design and heat management using finite element techniques. These models can be implemented using commercial or open-source software. In [98] was modeled the gas movement in the flow field, the coolant effect of the gas, and the liquid water removal inside the cell.

The models presented before and others are focused on optimizing the cell performance through adequate feeding to ensure the right amount of water is present during operation. If the control is not performed adequately, the cell can dry out due to excess evaporation, decreasing its conductivity and damaging the cell components or flooding due to lack of water removal. In the following sub-sections, those phenomena are described.

Water flooding

Water flooding is an issue that consists of the deactivation of a part of the catalytic layer of the cell for fuel starvation due to liquid water clogging the GDL or flow field.

Water flooding occurs when an excess of water is accumulated locally in the cell. This phenomenon typically occurs on the cathode side due to the a) water generated by the electrochemical reaction happens on the cathode side, b) excess of water transferred from the anode due to the electro-osmotic drag and not sufficiently counteracted by the back-diffusion phenomenon or due to c) an excess of water feeding from the inlet gas humidity. The two first causes are due to high current densities, which increase the electro-osmotic drag and the water generation the third cause is due to non-controlled gas feeding conditions.

Flooding can also happen on the anode but is much less common due to the effect of the electro-osmotic drag [99]. Anode flooding typically occurs when low current densities occur. Hence there is a small effect of electro-osmotic water drag,

and water tends to stay in the anode. The anode flooding can also be accentuated by forcing undesirable excess water humidification on the inlet gas.

Water drying

Lack of humidification in the cell reduces the proton conductivity of the membrane, which causes an increment of ohmic resistance and may produce an increase in anode kinetic over potential [100]. This effect produces the undesired cell performance, which may cause fast degradation of the membrane life span [100].

Since the water is generated on the cathode side, the drying effect is more commonly observed in the anode. In these terms, it is crucial to control the humidification of the anode to prevent it from drying out. The humidification 100% RH value in the anode inlet stream is often used in operating PEMFC.

4.2.2 Heat management

The irreversibility of the chemical reactions and the intrinsic ohmic resistance of the cell components are the main factors of heat generation on fuel cells [101]. Moreover, the split of the chemical reaction in two separate active areas on each side of the membrane produces non-equal heat generation, higher on the cathode. The heat sources combined (irreversible heat, entropy heat, and ohmic losses) are comparable to the output power of the overall cell [101].

Typically, the PEMFC work within a range of 60-80 °C. The intent is to keep the membrane properly hydrated while avoiding flooding by excess liquid water (lack of evaporation) in the low-temperature range. Lower temperatures also reduce the reaction kinetics.

In terms of heat management, the key parameters to control are heat uniformity and heat dissipation, especially on stacks where natural heat dissipation becomes more complex. Therefore, active cooling strategies are put in place.

Controlling the temperature is vital for the overall performance of the cell. Heat management becomes even more challenging when the current demand is not constant. A PEMFC stack model was used [102] to evaluate the change in

the outlet water temperature of the coolant for different current loads. A cooling system is proposed using the described model to tightly control the operating temperature in a defined current density profile.

A more complex environment occurs when the electric current is not defined by a profile since it cannot be planned, such as in vehicles driven by human beings. In this sense, control tuning of the cooling settings to manage the variable demand or vary the cooling function of the demand is relevant to avoid uncontrolled temperatures. A driver demand model was used as input to a 0D model of a fuel stack temperature to analyze multiple cooling temperatures. The actual operating temperature and the flow rate of cooling were required to be fitted according to its dynamic power demand [103].

More complex models focus on the homogeneity of cooling along the cell [104]. The model presented studies a five-cell stack with constant cooling and analyzes how its cell operates at slightly different temperatures as a consequence of the position and the effect of cooling at each level.

4.2.3 Fuel feeding

The consumption of H_2 and O_2 along the cell requires correctly calculating the fuel fed on the gas streams to prevent the cell from starving. In these terms, high stoichiometric mixtures are used to ensure continuous and sufficient feeding to the whole cell. On the other side, excess fuel will cause inefficiency, as a considerable amount of fuel will be expelled through the exhaust. To ensure homogeneous and constant feeding, two considerations must be taken into account, a) managing the stoichiometric gas mixture and b) adequate flow field design.

Even with sufficient stoichiometry ratios, if the flow field design is not adequate, the partial pressure of the gases may not be even and cause a low-performance local operating point. This phenomenon is accentuated when low stoichiometry ratios are used.

Lack of adequate fuel feeding may produce non-satisfactory cell performance, but if managed properly, may be used as output power control [105]. The overall

power of the cell can be controlled by managing the H₂ feeding and has been proved that hydrogen control provides more stable results than O₂ control.

Flow field design to analyze the homogeneous feeding was simulated using complex 3D models with open source finite volume, OpenFoam, [106]. Other complex models using available commercial software were used to investigate novel flow field patterns for better distribution of gas streams and obtain a more homogeneous current density [107].

In [108], flow field designs were proposed using non-rectangular channel shapes only obtainable using additive manufacturing techniques, which were tested and analyzed to homogenize the fuel distribution.

4.3 Model classification in PEM fuel cells

Models are helpful in understanding or representing specific phenomena of the cell with a certain level of abstraction. There are numerous possible approaches and strategies for modeling the various phenomena in the cell. Each of them will focus on different characteristics obtaining different information depending on their approach. The models can be categorized into four different types according to the number of dimensions represented, the structure of the model, the time dependence of the variables, and the thermal dependence, Fig. 4.1.

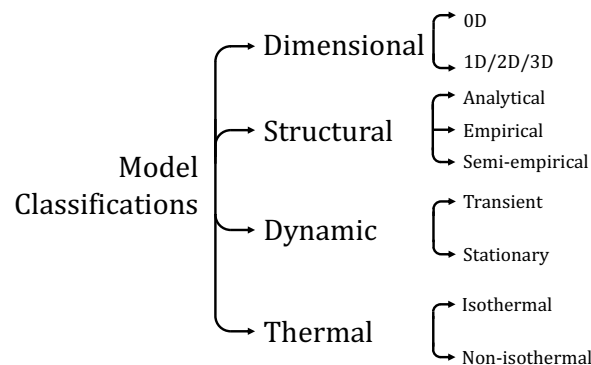


Figure 4.1: Model classification homogeneous function of their attributes.

In the following subsections, each classification is explained, and some examples of applications are provided.

4.3.1 Dimensional classification

The models can be categorized depending on the number of spatial dimensions they represent. There are four main types of models according to their dimensions 0D, 1D, 2D, and 3D. Inhere will also be considered the pseudo-N dimensions model, which combines different dimensionality models.

0-Dimension model

0-Dimensional models do not take into account any spatial analysis. For instance, the voltage-current relationship is a 0D model since no dimensional variable defines the performance relationship between both variables.

In this thesis, the models representing the electrochemical behavior are 0D, as shown in section 5.4.1.

1-Dimension model

Those models represent the phenomena in a single dimension. A simplification that is usually applied considers that in volumes where the studied dimension is much smaller than the other two ($z \ll x$ or y , for instance), only one-dimension models are typically used as the contribution of the other axes to the phenomenon studied is negligible in comparison with the primary axis. In the case of fuel cells, the most common one-dimensional models study the axis perpendicular to the GDL (in this thesis, it will be referenced as z). For example, in studying the liquid water expelled from the GDL, the plane is much bigger than the z axis, considering that the water movement occurs mainly on this axis. Therefore a single dimension model is an excellent approach to represent this phenomenon.

1D modeling is used in fuel cells to study the evolution of the species from anode to cathode focusing on the z axis in [109, 110].

2-Dimension model

Two-dimensional models typically study the planes a) zx or zy (referencing Fig. 3.1), which is, for example, a cross-section of the cell to analyze the movement of the gases

and water from under the ribs to the channel [111, 112, 113] or b) the MEA plane xy . The MEA plane study, xy , allows for analyzing the spatial distribution of gas and liquid water concentration due to the effect of the gas streams evolving along the flow field. In this thesis, the xy plane is considered to study species' spatial homogeneity.

2D models have been used to study the effect of the rib pressure over the MEA, and the local deformations and stresses produced due to the tightening forces [112]. It also studied the impact of the channel and ribs on the water removal [111].

3-Dimension model

3D models are an extension of the 2D models to evaluate the overall cell performance. Those models are used to study the evolution of gases inside the whole cell using Computer Fluid Dynamics (CFD) run by commercial software such as ANSYS, COMSOL, or others; or by open-source software such as OpenFoam. Those types of models have high computational costs. 3D models are used to study the effect of serpentine flow fields using Ansys Fluent 18.2 in [114]. Also, using a 3D Ansys Fluent model, the behavior of liquid water inside the channels for an interdigitated flow field design configuration was studied in [115]. In [116] is shown a 3D model simulated using a CFD to study the species' movement and the RH in the flow field.

Pseudo N-Dimension model

Pseudo-models reduce the computational cost as, by reducing the number of dimensions, typically the number of elements to simulate is lower, the algorithm is simpler hence faster, and the models used may be less expensive to calculate. This approach, the dimensional reduction, decreases the calculation effort. Multiple dimensional models, such as 2D or 3D, can be simplified by creating 1D+1D, 1D+2D, 2D+2D, or other combination models to obtain an approximate N-Dimensional representation with less computational cost.

To reduce the dimensionality of a model, typically, the axes showing the most significant impact on the variables are taken as the main ones. The rest of the axes are decoupled or disregarded. In the case of the water liquid removal in the GDL, it may be considered that the z axis is the principal axis, and the x and y are secondary.

Therefore, the water liquid removal model could be dimensionally reduced to a 1D in the axis z . When reducing dimensionality, some information may be lost. For instance, in the previous example, the liquid water movement in the xy plane. If this phenomenon is considered to be taken into account, it is possible to create a liquid water movement model in the xy plane decoupled from the model in the z -axis.

In this thesis, models of different dimensionality have been used to compound a pseudo-3D model to represent the complete PEMFC spatially.

Other authors have also used pseudo-3D models such as [117], which investigates the cell performance uniformity or [118] the impact on cell performance due to carbon corrosion on a dead-end and anode bleeding operation modes.

4.3.2 Structural classification

This section explains the classification of the models according to their structure, that is, according to the level of dependence of the variables on basic physicochemical principles or experimental values, in analytical, empirical, and semi-empirical models.

Analytical model

Analytical models are composed of physicochemical-based principles equations. These models typically define physical phenomena from the theoretical standpoint based on other physical properties or constants. This type of model ranges from elementary models to highly complex equations systems that may require high computational effort. The precision obtained with those models can be extremely high but may require multiple variables, becoming very expensive computationally to solve, and parameters sometimes hard to physically measure. Analytical models use measurable parameters of the elements such as thickness, conductivity, heat capacity, or others depending on the field. In fuel cells, for instance, the open voltage, Eq.(5.13), or the fuel consumptions, Eqs.(5.4-5.5), are analytical models.

Empirical model

Empirical models usually are fitted curves, neuronal network functions, or other correlated models of the experimental data. These models, also known as parametrized models, usually describe the relationship between the variables as a polynomic equation (or other simple mathematical systems) in which parameters are fitted with the empirical data.

This kind of model is helpful to represent, once adjusted, a physical behavior within a known operating range. Identifying parameters simplifies the effort required to understand the physical definition of the unknown parameters. Also, this kind of model has a reduced computational effort due to the mathematical simplicity of solving them. Due to adjusting parameters, its extrapolation capability is compromised as the parameters identified may vary outside the studied range.

In fuel cells, a typically used empirical model is membrane conductivity which is a function of the water content in the cell. The model is fitted using experimental data that relates water activity or water content in the membrane with conductivity [119]. Another example of this kind of model is the Leverett equation which describes the capillary pressure concerning the liquid water content on a porous media [120].

Semi-empirical model

Semi-empirical models are primarily analytical, but fitted empirical equations represent part of the behavior. Electro-osmotic drag flow could be an example of a semi-empirical model since the molar water flow is analytically described, but the electro-osmotic drag coefficient is a fitted parameter equation based on regression from experimental data. Actually, regarding the nature of the electro-osmotic drag coefficient, there is still debate on its nature [121]. Therefore, the definition of n_d is still under discussion. Similarly, the water diffusion coefficient of the membrane in the back-diffusion equation is experimentally adjusted. The law describing the water diffusion is analytically described by Darcy, but the coefficient which defines the rate of the diffusion is experimentally obtained and is a function of the water content in the membrane [122].

4.3.3 Dynamic classification

Models can be classified according to their capacity to represent the time evolution of specific variables. By this classification, two different types of models can be developed:

Transient model

In transient models, their outcome depends on time or previous states. This is the case of the model, which represents a droplet movement inside the flow field. To calculate the advancing speed of a droplet, the acceleration is calculated using the forces that act upon its current time step. To simulate this model, the previous time step has to be known to determine the current speed Eq. (5.57) [123].

Stationary model

In stationary models, their outcome does not depend on time but on the value of their state variables. The PEM fuel cell polarization relationship is a 0D stationary model; the relationship between current and voltage is solely defined by the amount of water in the membrane and the partial pressures of the gases (subsection 5.4.1).

Typically transient models are more expensive computationally than stationary models since they represent the transition with states instead of the values of a single state.

4.3.4 Thermal classification

Models can be classified considering if the variation of temperature along the simulations is evaluated. There are two types of models depending on temperature behavior:

Isothermal model

Those types of models consider the temperature constant along their simulation. It simplifies the whole complex model, which helps study certain areas in a more simplified way considering the cell is working at a constant temperature.

In this thesis, the models implemented are isothermal, considering a known steady-state temperature homogeneous in the whole cell.

Non-isothermal model

Non-isothermal models consider the generation of heat due to the electrochemical reaction and study how this flux and the temperature change affect cell performance.

4.4 Conclusions

This chapter focuses on the main PEMFC challenges that are being tackled using simulations a) water management, b) heat management, and c) fuel feeding.

Later a model classification is proposed to categorize the different models to facilitate the understanding of the submodels used in this thesis.

5

Modeling hypothesis

Contents

5.1	Introduction	49
5.2	Submodel description	51
5.2.1	MEA modeled phenomena	52
5.2.2	Flow field modeled phenomena	54
5.3	Models classification summary	55
5.4	MEA model	56
5.4.1	Electrochemical model	56
5.4.2	Membrane water balance	68
5.4.3	GDL water and gas diffusion	71
5.4.4	GDL water evaporation and condensation	76
5.4.5	GDL liquid water removal	79
5.5	Flow field model	80
5.5.1	Gas pressure drop along the flow field	81
5.5.2	Concentration variation of species in the flow field	83
5.5.3	Droplet movement model	87
5.5.4	Droplet water evaporation	98
5.5.5	Droplet water re-absorption	99
5.6	Conclusions	100

5.1 Introduction

This chapter shows a PEM fuel cell modeling and simulation methodology to enable a pseudo-3D dynamic simulation with low computational cost. This objective

is tackled by a) designing a model with the required hypotheses to enable low computational cost solvers without compromising the accuracy of the results and b) designing a simulation methodology that intends to optimize the speed of the simulations to allow long-term simulations.

The model presented in this thesis enables the study of a PEM fuel cell's spatial and temporal behavior, allowing the cell performance evaluation under different conditions and flow field geometries. The model simulations can represent liquid water in a fuel cell and its impact on spatial uniformity in the 2D plane. The model is transient and isothermal. The complete model is compounded with multiple submodels using different dimensional reductions to provide a pseudo-3D PEMFC representation for the complete model result.

Each submodel represents physical phenomena or a physical layer in the cell with a low computational effort; these computational approaches have been obtained using stationary models instead of transient when possible and by dimensional reduction.

Depending on the phenomenon studied, the different models may contain analytical, empirical, or semi-empirical equations to describe the studied phenomenon.

In this chapter and the following one, each submodel is described and explained how it has been numerically implemented. To facilitate the understanding of the models, this chapter is divided into the following sections:

1. Submodels description. Section 5.2 presents a high-level description of the two main groups of submodels: MEA and flow field submodels.
2. Dimensionality of submodels. The classification of submodels depending on the dimensionality is later explained in section 5.3.
3. Physical hypotheses of submodels. In sections 5.4 - 5.5, the physical hypotheses equations describing each submodel are presented.

The next chapter describes the numerical procedure implemented and the inter-connection between models.

5.2 Submodel description

In chapter 2, a detailed description of the components of a fuel cell was presented. The model has been simplified, considering that it is isothermal. The cooling plates are not modeled to save computational effort. The PEM fuel cell has been divided into three different main components, which represent three physical elements a) the cathode flow field, b) the MEA, and c) the anode flow field. The symmetry of the fuel cell and the phenomena described in those three components allow it to be represented by two models: the flow field and MEA.

Conceptually, at the modeling level, the different components of the cell are interconnected by an interface that permits the exchange of species, gases, and water. Regarding water, the model allows representing the exchange in liquid or steam form. In Fig. 5.1, an illustration shows the multiple water exchange phenomena occurring in a PEM fuel cell. This figure is used as a reference when describing the different submodels explained in this chapter.

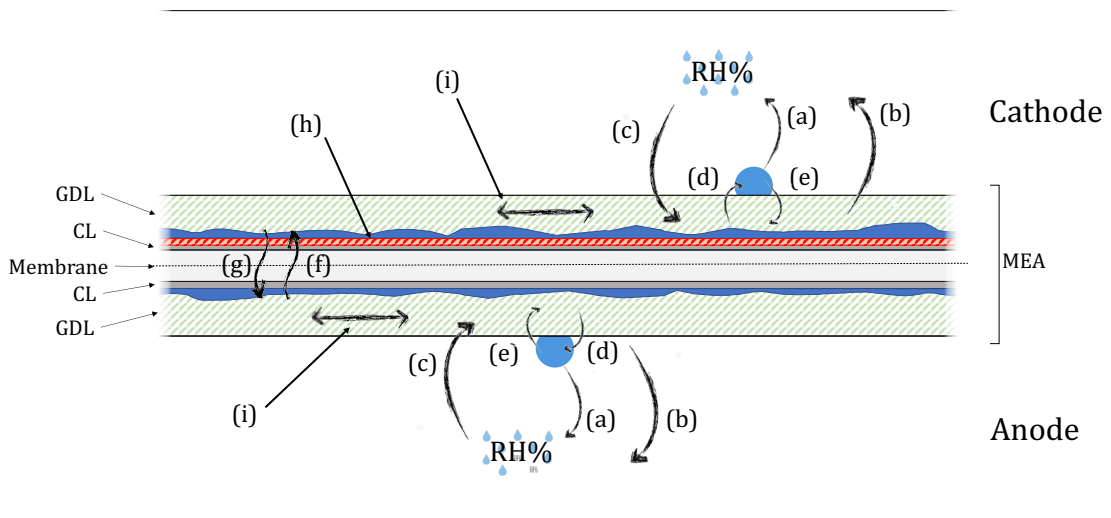


Figure 5.1: Conceptual representation of the different phenomena of water exchange in the cell a) droplet evaporation in the flow field, b) liquid water evaporation from the GDL, c) flow field to GDL steam condensation, d) GDL liquid break-through, e) liquid water re-absorption in the steam phase, f) electro-osmotic drag, g) back diffusion, h) water generation, i) in-plane diffusion.

5.2.1 MEA modeled phenomena

The MEA is composed of the GDLs, the catalytic layers (CL), and the membrane. Each physical component is modeled using a different principal axis depending on the phenomenon modeled. The submodels implemented to represent the MEA are:

1. Electrochemical reactions model, species consumption and generation (section 5.4.1). This model allows calculating the electrochemical reactions that convert the fuel species into electric current and water. The generation of water and the consumption of O_2 occurs in the cathode CL due to the semi-reaction. The model considers the consumption of H_2 in the anode.

The model implemented is stationary, isothermal, and 0D. The model allows updating the amount of water, and the concentration of the gases exchanged with other physical layers represented by different submodels.

2. Membrane water balance (subsection 5.4.2). The membrane water balance model accounts for the electro-osmotic drag (Fig. 5.1-f) and back-diffusion (Fig. 5.1-g), which calculates the water movement in the membrane between anode and cathode side. The electro-osmotic drag is an ion water dragging phenomenon caused by the ions flow in the polymeric membrane in the direction of the protonic flow from anode to cathode. On the other side, the back diffusion, or just water diffusion, is caused by the difference in water concentration on each side of the membrane. As the electro-osmotic drag direction is from the anode to the cathode, the water concentration tends to be higher on the cathode side than on the anode. Therefore, this phenomenon is called back diffusion since it compensates the water concentration gradient between the anode and cathode side.

Those models are implemented as stationary, isothermal, and 0D. The simulation calculates the water flow considering the current value of water content on each side of the membrane.

3. GDL water and gas diffusion (section 5.4.3). Water is generated on the cathode CL and removed from the flow field through the GDL. Liquid water movement inside a porous media (Fig. 5.1-j) is modeled using Knudsen diffusion. The steam water and other gases' movement inside a porous media is modeled using the Fick, or Stefan-Maxwell [124] diffusion. In this thesis, Fick's equation represents a single-component gas diffusion in the models. Liquid water movement inside the porous media is modeled using capillary pressure Fick diffusion [110]. Other phenomena such as heat conduction, mechanical deformation due to tightening force, or others are not considered nor included in the models. The models used to represent these phenomena are transient, isothermal, and 2D focused on the xy plane.

4. GDL water evaporation and condensation (subsection 5.4.4). Water evaporation (Fig. 5.1-b) and condensation (Fig. 5.1-c) from the GDL is a consequence of the difference between the relative humidity on the flow field and the concentration of water in the GDL.

To prevent MEA from drying, the inlet gases are humidified to maintain the cell within the water content in the working range. The gas humidity in the flow field is condensed over the interface GDL-flow field. This phenomenon occurs both on the cathode and anode sides and is modeled.

The evaporation and condensation rate also depends on the temperature of each specific localization. To reduce the complexity of the model, the spatial variation of temperature in the cell is not considered; therefore, the model used is isothermal. Dynamically the model is stationary, and 0D occurs over a specific area on the GDL.

5. GDL liquid water removal (subsection 5.4.5). The water content of the GDL may be removed in liquid form to the flow field (Fig. 5.1-d). This phenomenon occurs when, locally, the water content surpasses the capillary pressure limit in the GDL, and liquid water is expelled to the flow field. GDL surfaces are commonly treated with high hydrophobic materials such as PTFE and others

to reduce the amount of water retained in the GDL [61]. The hydrophobic treatments of GDL have three main functions a) prevent evacuated liquid water from swallowing again into the GDL, b) reduce the capillary breakthrough pressure of the GDL, and c) facilitate the liquid water removal from the cell. This phenomenon may happen both in the cathode and the anode side, but it is more common on the cathode due to the electro-osmotic drag effect. These phenomena are implemented in the model. The model is transient, isothermal, and 0D, which allows the simulation of the amount of water expelled, taking into account the water content in the GDL.

5.2.2 Flow field modeled phenomena

The flow field model represents the humidity evolution, the effect of gas consumption on the species concentration in the gas flow, and the pressure drop. In addition, it allows the representation of the movement of the water droplets. The submodels whose compound the flow field model are stationary, isothermal, and 1D along the path of the flow field. Inside, the flow field spatially corresponds with the channels where the gas flows. The kinetic energy of the gas is lost due to friction in the form of pressure loss, the droplets' movement, and condensation of steam water from the GDL. To simulate the flow field, the following submodels have to be considered:

1. Gas pressure drop along the flow field (subsection 5.5.1). The gas pressure changes in the flow field are modeled in a transient manner, isothermal in 1D along the flow field path, and they are due to two phenomena:
 - The gas speed inside the flow field reduces its energy due to the friction with the walls. The flow field turns obstacles droplets' movement, and the geometry of the flow field causes a decrease in pressure as a consequence of the gas speed reduction.
 - The fuel consumption produces a drop in gas concentration in the gas stream, which directly decreases the overall pressure.

2. Species evolution (subsection 5.5.2). The amount of water in the flow field changes due to: the liquid water evaporation (Fig. 5.1-b) and the condensation (Fig. 5.1-c) from the GDL and the droplets (Fig. 5.1-d). Similarly, as a consequence of fuel consumption, the concentration of those species evolves along the flow field.
3. Droplet movement (section 5.5.3). The droplet movement is dynamic and isothermal in 1D along the path of the flow field. To properly represent the serpentine shape of the flow fields into the cell, the 1D is converted into a pseudo-2D model. The movement of droplets over a surface is widely studied in [123, 125, 126]. The submodels developed considered droplets with known volume, airflow, and surface-drop properties to compute the advancing velocity along the flow field. Furthermore, as multiple drops may be moving simultaneously, the clutter of two or more drops that are close enough is considered.
4. Droplet water evaporation (section 5.5.4). When the relative humidity is not saturated inside the flow field, droplets are reduced by the evaporation effect (Fig. 5.1-a). Relative humidity condensation to a specific droplet is neglected in this model. Those models are transient, isothermal 0D occurring on a specific droplet in the flow field.
5. Droplet water re-absorption (section 5.5.5). Liquid water can be reabsorbed from a droplet of the flow field to the GDL. The water content re-absorption modeling occurs in the steam phase (Fig. 5.1-e). The water transfer from the flow field into the GDL only occurs when the difference between the RH of the flow field and the GDL reaches a critical threshold. The droplet water re-absorption is modeled as 0D, stationary isothermal.

5.3 Models classification summary

In the previous section, an introduction of each model developed for this thesis, and a high-level description is presented. The number of dimensions, the main axis

represented in the model, the structure type, and the dynamic classification of each submodel are summarized in Tab. 5.1. This table is divided into two submodel groups, MEA and flow field. This differentiation, already used in the previous section, is achieved by sharing physical characteristics and variables.

	#Dims	Axes	Structure	Dynamic
MEA				
CL electrochemical reactions	0D	-	analytical	stationary
Membrane/CL water back diffusion	0D	-	analytical	stationary
Membrane/CL water E-O. drag	0D	-	analytical	stationary
GDL/CL water and gas diffusion	2D	x, y	semi-empirical	transient
GDL water evap. and cond.	0D	-	semi-empirical	transient
GDL liquid water removal	0D	-	semi-empirical	transient
Flow field				
Pressure drop	pseudo-2D	x, y^*	empirical	transient
Species concentration evolution	pseudo-2D	x, y^*	analytical	transient
Droplet movement	pseudo-2D	x, y^*	empirical	transient
GDL liquid water re-absorption	0D	-	semi-empirical	transient

Table 5.1: Summary table of the classification of each implemented submodel

The symbol * in the axis field of Tab. 5.1 denotes that the model uses an approach on a straight channel that will represent the x and y axes. Those models are further described in sections 5.4 - 5.5 where the equations describing the model are presented. For some models also, a reference to a portion of the implemented code is referenced.

5.4 MEA model

5.4.1 Electrochemical model

Electrochemical reaction

This section presents the main electrochemical equations which drive a PEM fuel cell. The equations and models describe the reactions, the theoretical performance, as well as the overpotentials which limit the cell efficiency. Most models representing the electrochemical models in the literature are analytical or semi-empirical, dimensionally 0D, and represent the system's state given certain conditions. Due

to the semi-empirical structure of the model, some equation parameters must be adjusted to have a realistic representation of the cell's performance.

A PEM fuel cell generates current by a chemical reaction within O_2 (fed in the cathode) and H_2 (fed in the anode) as a reaction of both components H_2O is produced, Eq. (5.1). This overall reaction has a free Gibbs (ΔG) energy between $-228.57 \text{ kJ}\cdot\text{mol}^{-1}$ and $-237.13 \text{ kJ}\cdot\text{mol}^{-1}$ function of how water is produced, in steam or liquid form.



This reaction, Eq. (5.1), occurs in two separate places. On the anode CL, hydrogen is dissociated into protons and electrons, Eq. (5.2). The protons flow through the electrolyte to the cathode CL, while the electrons generated in the anode flow through the external electric conductors from the anode to the cathode side. In the cathode CL, those protons are combined with the oxygen molecules and electrons to produce water, Eq. (5.3).



From the two semi-reactions occurring in the cell, Eqs. (5.2-5.3), the consumption of reactants and the water generation are calculated, Eqs. (5.4-5.6) [127]. The negative signs in Eqs. (5.4-5.5) represent the consumption of those species, while the positive sign in Eq. (5.6) specifies that this compound is generated as a consequence of the operation.

$$S_{O_2} = -\frac{M_{O_2}}{4F} j \quad (5.4)$$

$$S_{H_2} = -\frac{M_{H_2}}{2F} j \quad (5.5)$$

$$S_{H_2O} = \frac{M_{H_2O}}{2F} j \quad (5.6)$$

Where S_{O_2} and S_{H_2} are the oxygen and hydrogen consumption respectively, S_{H_2O} is the water generation. The molar fluxes are calculated using the molar weight of each component, M_i , the Faraday constant, F , and the current density, j .

The maximum usable energy can be calculated using Eq. (5.7) where G is Gibbs free energy, H is the enthalpy, S the entropy, and finally, T is the temperature at which the reaction occurs.

$$G = H - TS \quad (5.7)$$

Therefore, by using the molar values and the variation of enthalpy and entropy, the maximum theoretical performance, η_{max} , can be calculated using Eq. (5.8) where Δg_f , Δh_f and Δs_f are the formation free Gibbs energy, the formation enthalpy and the formation entropy respectively, Eqs. (5.9-5.10).

$$\eta_{max} = \frac{\Delta g_f}{\Delta h_f} = \frac{\Delta h_f - T\Delta s_f}{\Delta h_f} \quad (5.8)$$

$$\Delta h_f = (h_f)_{H_2O} - (h_f)_{H_2} - 0.5 (h_f)_{O_2} = -241.8 - 0 - 0.5 \cdot 0 \quad (5.9)$$

The overall performance can be calculated using liquid water or steam enthalpy, the example shown uses team water formation enthalpy. In the following calculations, steam water enthalpy is used (-241.8 kJ·mol⁻¹) when the temperature is higher than 100 °C and liquid enthalpy of formation if the temperature is lower than 100 °C (-285.8 kJ·mol⁻¹). A relationship between temperature and maximum cell performance can be observed in Fig. 5.2.

$$\Delta s_f = (s_f)_{H_2O} - (s_f)_{H_2} - 0.5 (s_f)_{O_2} = 0.07 - 0.131 - 0.5 \cdot 0.205 \quad (5.10)$$

$$\eta_{max} = \frac{\Delta h_f - T\Delta s}{\Delta h_f} = \frac{\Delta h_f + 0.163T}{\Delta h_f} = \frac{\Delta h_f - 0.163T}{\Delta h_f} \quad (5.11)$$

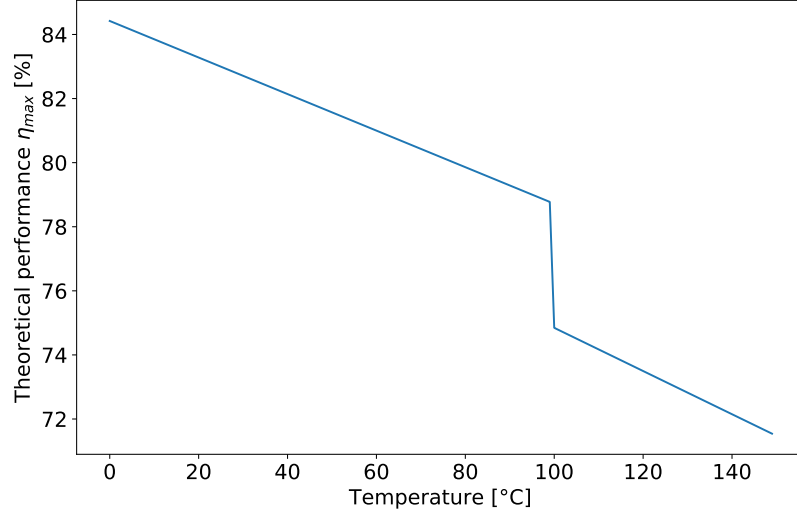


Figure 5.2: Maximum theoretical performance of a PEM fuel cell function of its temperature

Potential and overpotential

The PEM electrical model relates the cell's current density and voltage. The open circuit voltage is described with Nersnt's equation, Eq. (5.12) [128]. Nersnt's equation uses free Gibbs energy value to calculate the cell's open circuit or reversible voltage, E_0 , where n is the number of exchanged electrons, F is the Faraday constant, and Δg_f is the formation free Gibbs energy.

$$E_0 = -\frac{\Delta g_f}{nF} \quad (5.12)$$

Using Gibbs reversible voltage, the thermodynamic potential of the cell can be calculated using the partial pressures of both fuels, P_{O_2} and P_{H_2} , Eq. (5.13), where R is the gases constant.

$$E = E_0 + \frac{RT}{2F} \left(\ln(P_{H_2}) + \frac{1}{2} \ln(P_{O_2}) \right) \quad (5.13)$$

There are other studies that observed higher dependency on temperature than the represented by equation Eq. (5.13) [129]. In this work, the original reversible thermodynamic voltage is considered.

Due to implementation constraints, the cell operation has some performance inefficiencies, which are taken into account as overvoltages that decrease the maximum theoretical performance of the fuel cell. The overvoltages of a PEM fuel cell are described in the following subsections.

Activation overpotential

The activation losses are the consequence of the formation of new chemical bonds and the energy required for that. The Tafel equation represents the activation losses, V_{act} , Eq. (5.14), where j_0 is the exchange current density and j , the current density. This overpotential is more significant at very low current densities.

$$V_{act} = \frac{RT}{2F} \ln \left(\frac{j}{j_0} \right) \quad (5.14)$$

The implementation of this model can be found in Appendix D.1.3.

Ohmic overpotential

Ohmic overpotential is related to the intrinsic protonic resistance of the membrane and the electric conductors, but the membrane resistivity is the main contributor to the ohmic overpotential, Eq. (5.23) [130]. The conductivity of the membrane, σ_{m,T_1} for a given temperature T_1 is described by Eq. (5.16), where σ_{m,T_0} is the reference conductivity at temperature T_0 .

$$\sigma_{m,T_0} = (b_1 \lambda_m - b_2) \quad (5.15)$$

$$\sigma_{m,T_1} = \sigma_{m,T_0} e^{b_3 \left(\frac{1}{T_0} - \frac{1}{T_1} \right)} \quad (5.16)$$

Being λ_m , Eq. (5.17), function of the water activity, a_k , in the anode or cathode. The parameters b_1 , b_2 , b_3 are the membrane conductivity constants, $5.139 \cdot 10^{-3}$,

$3.26 \cdot 10^{-3}$, 1268 respectively [130]. Water activity, Eq. (5.18), depends on the total gases pressure, P , the molar fraction of steam water, X_{H_2O} , and the saturation water pressure at current conditions, P^{sat} .

$$\lambda_m = \begin{cases} 0.043 + 17.81a_k - 38.85a_k^2 + 36.0a_k^3, & 0 < a_k < 1 \\ 14 + 1.4(a_k - 1), & 1 < a_k < 2 \end{cases} \quad (5.17)$$

$$a_k = \frac{X_{H_2O}P}{P^{sat}} \quad (5.18)$$

Alternatively, the water content in the membrane, λ_m , can be calculated using Eq. (5.19) [131]. With the amount of water in each element, the water content in the membrane λ_m can be calculated using Eq. (5.20).

$$\lambda_m = \frac{WU}{IEC \cdot M_{H_2O}} \quad (5.19)$$

$$\lambda_m = \frac{EW}{1000} \frac{W_{wet} - W_{dry}}{W_{dry}} 100 \frac{10}{18} = EW \frac{\rho_{H_2O} \epsilon_m s}{W_{dry}} \frac{100}{18} \quad (5.20)$$

Where IEC is the ionic exchange capacity of the membrane, WU the water uptake, EW is the equivalent weight of the membrane, W_{wet} the weight of the membrane in wet conditions, W_{dry} the weight of the membrane in dry conditions, ϵ_m the porosity of the membrane and s the normalized water content of the membrane.

The membrane's protonic conductivity is highly sensitive to its water content, Eq. (5.20). The temperature also impacts the proton conductivity, Eq. (5.16). As described in subsection 3.2.1 the primary mechanism of protonic conductivity in the membrane is the vehicular mechanism which is the proton flow through an aqueous medium that acts as a proton carrier. Therefore the higher the amount of water, the higher the conductivity.

Fig. 5.3 shows the behavior of the membrane conductivity function of the water content and temperature. The figure shows that the increase concerning temperature for a given water content is fairly linear in the studied range [132].

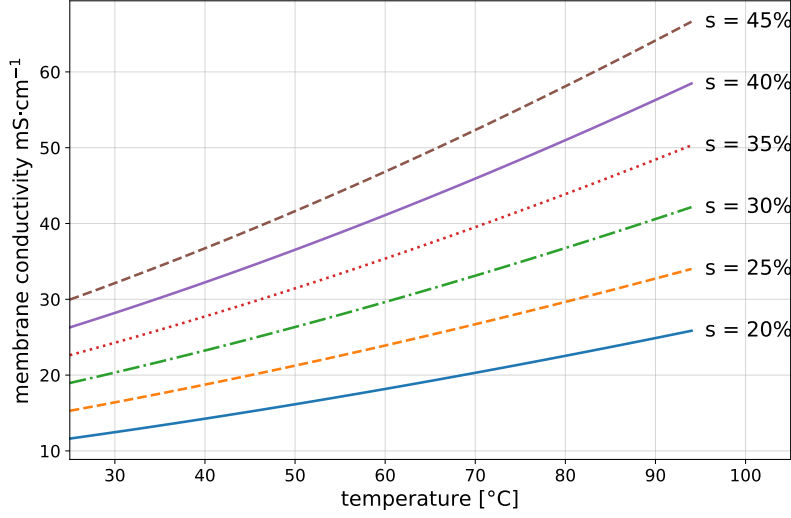


Figure 5.3: Membrane conductivity function of the temperature and normalized water content

In other investigations [119], an alternate model of membrane conductivity is proposed. This alternate model has been used in the research as it provided better fitting, Eq. (5.21).

$$\sigma_{m,T_0} = \sigma_{m,0} (WU - WU^c)^\beta \quad (5.21)$$

The membrane conductivity model proposed, Eq. (5.21), is an exponential model function experimental parameter, β , a reference conductivity at given humidification, $\sigma_{m,0}$, and the ratio between dry and wet membrane weight, WU , and the dry-wet reference ratio, WU_c , Eq. (5.22), which depends on the water content on the membrane. To calculate m_{dry} , the membrane is set into a vacuum oven at 60° C during 12 h, and to calculate m_{wet} , the membrane is immersed in water and then removed with a wiper on the surface of the membrane to account only for absorbed water.

$$WU = \frac{m_{wet} - m_{dry}}{m_{dry}} = \frac{(m_{dry} + s\epsilon\rho_{H_2O}V_m) - m_{dry}}{m_{dry}} = \frac{s\epsilon_m\rho_{H_2O}V_m}{m_{dry}} \quad (5.22)$$

The code implementation of this model can be found in Appendix D.1.4.

Finally, using the membrane conductivity calculated, the membrane ohmic overpotential can be evaluated using Eq. (5.23), where th_m is the membrane thickness and σ_m the actual membrane conductivity, V_m the volume of the bounding box of the membrane, ϵ_m the membrane porosity and s the water content of the membrane.

$$V_{ohm} = \frac{th_m}{\sigma_m} j \quad (5.23)$$

The electric conductivity of the GDL is much higher than the membrane's proton conductivity ($\sim 3500 \text{ mS}\cdot\text{cm}^{-1}$ versus $\sim 75 \text{ mS}\cdot\text{cm}^{-1}$) but also contributes in the overall ohmic overpotential, V_{ohm} , where th_{GDL} is the thickness of the GDL and σ_{GDL} is electric conductivity, Eq. (5.24).

$$V_{ohm} = \left(\frac{th_m}{\sigma_m} + \frac{th_{GDL}}{\sigma_{GDL}} \right) j \quad (5.24)$$

Concentration overpotential

The concentration overpotential, V_{con} , is the limitation on the performance due to the lack of reactants supply but is typically expressed function of the electric current density, j , Eq. (5.25).

$$V_{con} = 3 \cdot 10^{-5} e^{-8j} \quad (5.25)$$

This thesis applies an extended version of concentration overpotential used in [133]. This model considers the concentration of the reactants at each point of the CLs' surface, Eq. (5.26). It is described by the relation H_2 and O_2 reactant concentration, C_X , with the minimum required concentration, $C_{X,0}$, [134]. Typically, the concentration of H_2 is not limiting the reaction in normal operating conditions. Then, anode concentration overpotential is depicted, and the concentration overpotential is calculated using only the O_2 concentration.

$$V_{con} = \frac{RT}{4F} \ln \left(\frac{C_{O_2}}{C_{O_2,0}} \right) + \frac{RT}{2F} \ln \left(\frac{C_{H_2}}{C_{H_2,0}} \right) \quad (5.26)$$

The implementation of this model can be found in Appendix D.1.5.

Operating cell voltage

The operating cell voltage, V_{fc} , is calculated by subtracting the overvoltages, Eqs. (5.14, 5.23, 5.26) from Gibbs reversible voltage, Eq. (5.13), as is shown in Eq. (5.27).

$$V_{fc} = E - V_{act} - V_{ohm} - V_{con} \quad (5.27)$$

The contribution of the cell's ohmic, concentration, and activation losses in the polarization curve is represented in Fig. 5.4. In order to represent this polarization curve, the following parameters have been used: $j_0 = 10^{-3}$ A, $j_n = 10^{-4}$ A, $j_{lim} = 1.25$ A·cm⁻², $E_o = 1.24$ V, $\sigma_0 = 0.01$ S·cm⁻¹, $\beta = 1.025$ and $WU_c = 5.15$ %, $s = 0.25$, $P_{air} = P_{H_2} = 1.5$ atm and $T = 353$ K.

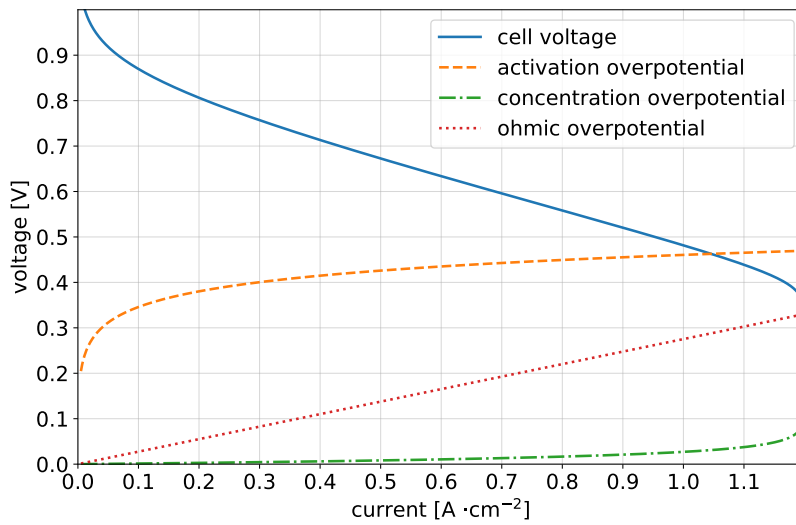


Figure 5.4: Simulation of polarization curve and the contribution of the different overpotentials

Effect of temperature on the polarization curve

The operating temperature has an essential effect on the performance of a PEMFC as it modifies the conductivity of the membrane, Eq. (5.16), the reversible thermodynamic voltage, Eq. (5.13), the activation loss, Eq. (5.14), and the concentration loss Eq. (5.26). Temperature also impacts the evaporation rate of water from the GDL since it changes the steam water content capacity.

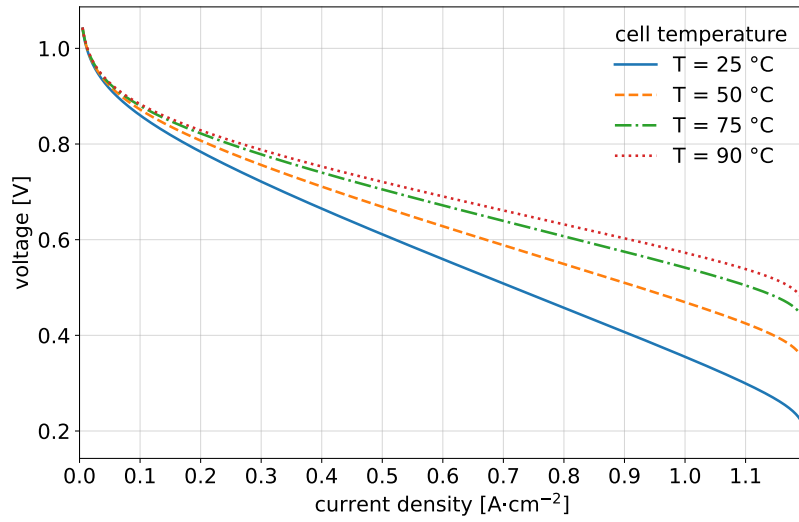


Figure 5.5: Simulation of polarization curve function of the operating temperatures.

In Fig. 5.5, the polarization curve has been shown for different cell operating temperatures. The parameters used to calculate the different polarization curves are $j_0 = 10^{-3}$ A, $j_n = 10^{-4}$ A, $j_{lim} = 1.25$ A·cm⁻², $E_o = 1.24$ V, $\sigma_0 = 0.01$ S·cm⁻¹, $\beta = 1.025$ and $WU_c = 5.15$ %, $s = 0.25$, $P_{air} = P_{H2} = 1.5$ atm. The increase in performance of the fuel cell is linked mainly to the change in the membrane's protonic conductivity with respect to temperature. The cell's temperature needs to be balanced to obtain better performance and prevent side effects. Managing temperature adequately, aside from increasing performance, is required to keep the humidity in an optimum range and decrease mass cross-over. But the use of higher temperatures may increase the possibility of current leakage and reduce the durability of the cell [135].

Effect of gas pressure on the polarization curve

The operating anode and cathode pressure do not significantly impact the fuel cell's performance, considering the pressure is over the minimum required pressure. A change in gas pressures impacts the reversible thermodynamic voltage Eq. (5.13).

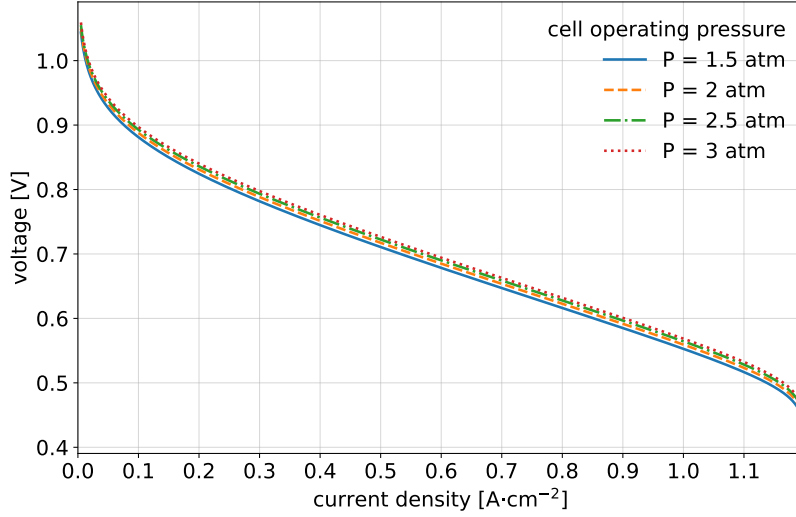


Figure 5.6: Simulation of polarization curve function of the operating gas pressures in anode and cathode

Those simulations are calculated using the following parameters: $j_0 = 10^{-3}$ A, $j_n = 10^{-4}$ A, $j_{lim} = 1.25$ A·cm⁻², $E_o = 1.24$ V, $\sigma_0 = 0.01$ S·cm⁻¹, $\beta = 1.025$ and $WU_c = 5.15$ %, $s = 0.25$, $T = 353$ K, and the same pressure on cathode and anode considering cathode uses air and anode H₂.

Fig. 5.6 shows the effect of gas pressure on the overall polarization curve. The variation in the cell's performance is small compared to the sensibility of other operational parameters. Using high-pressure gas feeding may ensure sufficient fuel partial pressures on the whole fuel cell area. Moreover, despite not having a significant benefit on the performance, higher operating pressures of the cell increases the cross-over increasing the production of peroxide reactants and the probability of membrane breakage. If the increase in pressure is not linked to an increment in the gas flow in the cathode, the higher working pressure may reduce the capability of removing liquid water from the cell [136].

Effect of membrane water load on the polarization curve

Water concentration on the membrane plays a vital role in the cell's performance. In Fig. 5.7 it can be observed the effect of water concentration (from 0%, meaning no water, to 100%, indicating the membrane is fully saturated with liquid water) in the polarization curve in the range within 25% and 40%. The figure shows the important effect of membrane water content on cell performance. Therefore, it is crucial to manage water properly to avoid inefficiencies. The parameters used in the simulations are the following: $j_0 = 10^{-3}$ A, $j_n = 10^{-4}$ A, $j_{lim} = 1.25$ A·cm⁻², $E_o = 1.24$ V, $\sigma_0 = 0.01$ S·cm⁻¹, $\beta = 1.025$ and $WU_c = 5.15$ %.

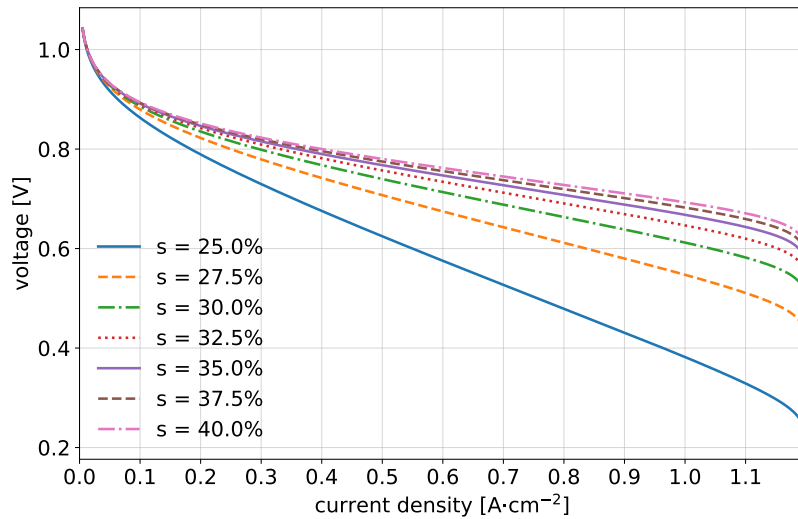


Figure 5.7: Simulation of polarization curve function of normalized water content in the membrane

The lower power is obtained when the water content decreases in the cell. Fig. 5.8 illustrates the power density function of different values of water content in the membrane. The figure shows that by decreasing the water content, the optimum operating power shifts to lower voltages.

This analysis demonstrates the importance of water management in the cell to ensure better cell performance.

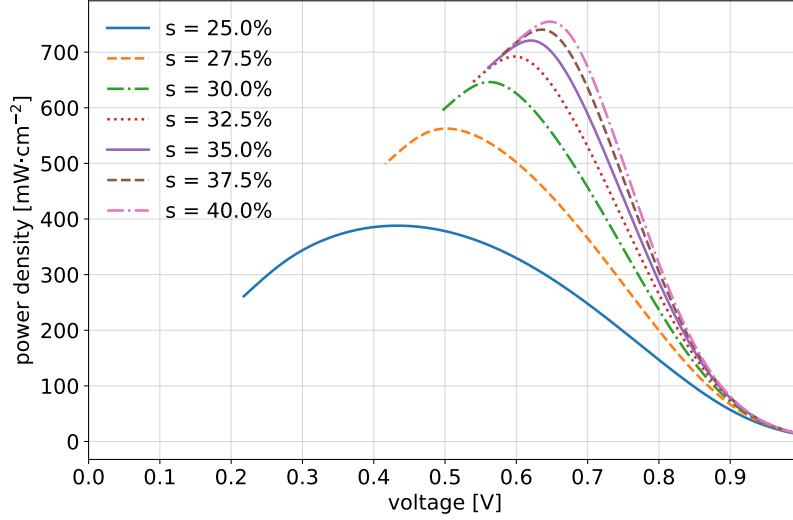


Figure 5.8: Simulation of power density function voltage different values of the water content of the membrane

5.4.2 Membrane water balance

Electro-osmotic drag

The polymeric membrane requires a proper hydration level to operate at optimal conditions. This hydration is obtained by adequate humidification of the gases feeding the fuel cell. In addition, during the fuel cell operation, water is generated in the cathode CL and hydrates the membrane. To ensure uniform hydration, the gas streams are usually humidified.

The membrane is water permeable [137]; therefore, water diffuses from anode to cathode and vice versa. This water exchange is driven by two phenomena a) the electro-osmotic drag, Eq.(5.29), which produces water flow proportional to the protonic current generated, depending on the amount of hydration of the membrane, and b) the back-diffusion, Eq.(5.33), which is a phenomenon produced by the difference on water content between anode and cathode, generating a water flow from the higher to the lower water concentration spatial regions. Those phenomena describe the water behavior in the MEA, which produce a strong interaction between anode and cathode, significantly impacting the cell's overall performance.

The electro-osmotic drag coefficient, n_d , Eq. (5.28), depends on the water

content of the membrane, λ_m . The water content, λ_m , Eq. (5.17), is related to the water activity of the cell, a_k Eq. (5.18), calculated using the steam molar fraction in the flow field, X_{H_2O} , with the actual vapor pressure, P^{vap} , and the saturated vapor pressure, P^{sat} , of water in the gas. The electro-osmotic drag flow, J_{eo} , is calculated using the Faraday constant, F , the current density, j , and the electro-osmotic drag coefficient, Eq. (5.29).

$$n_d = 0.0029\lambda_m^2 + 0.05\lambda_m - 3.4 \cdot 10^{-19} \quad (5.28)$$

$$J_{eo} = 2n_d \frac{j}{2F} \quad (5.29)$$

The code implemented in the model to represent the electro-osmotic drag can be found in Appendix D.1.6.

Water back-diffusion

The water back-diffusion is represented in the model by Darcy diffusion, which depends on the water content, λ_m , Eq. (5.17), of both sides of the membrane. The membrane water diffusion coefficient, considering only the water content in the membrane, is represented by D_λ , Eq. (5.30). This coefficient is corrected with the temperature effect, T , to obtain the actual water diffusion coefficient, $D_{\lambda,T}$, Eq. (5.31). The back-diffusion flow is calculated using Eq. (5.33) [130].

$$D_\lambda = \begin{cases} 1, & \text{if } 2 < \lambda_m \\ 1 + 2(\lambda_m - 2), & \text{if } 2 \geq \lambda_m \geq 3 \\ 3 + 1.38(\lambda_m - 3), & \text{if } 3 \geq \lambda_m \geq 4 \\ 2.562 - 0.33\lambda_m + 0.0264\lambda_m^2 - 6.71 \cdot 10^{-4}\lambda_m^3, & \text{if } \lambda_m \geq 4 \end{cases} \quad (5.30)$$

$$D_{\lambda,T} = 10^{-10} D_\lambda e^{2416(\frac{1}{303} - \frac{1}{T})} \quad (5.31)$$

New models provide a better and more continuous fit to the water diffusivity coefficient in the membrane [122]. The model re-calculates the D_λ by fitting the experimental data to a polynomial curve, Eq. (5.32).

$$D_\lambda = 10^{-10} \epsilon_m^{3/2} \frac{3.842\lambda_m^3 - 32.03\lambda_m^2 + 67.74\lambda_m}{\lambda_m^3 - 2.115\lambda_m^2 - 33.013\lambda_m + 103.37} \quad (5.32)$$

The two different models differ slightly, especially at lower water content in the membrane. In Fig. 5.9 shows how both models compare for the same water content, which shows a difference in terms of the oscillation around 27.5% of water content and the lower membrane water diffusivity as water content increases.

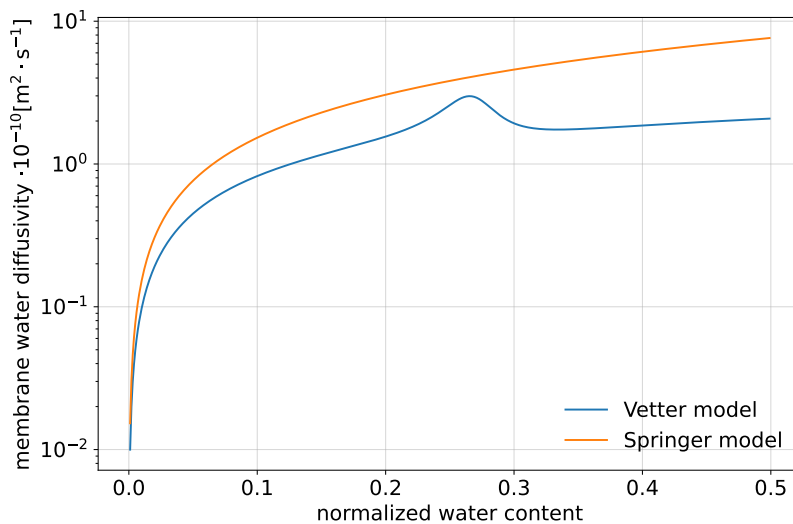


Figure 5.9: Comparison of Springer model [130] and Vetter model [122] at 80 °C

The behavior of the membrane diffusion coefficient with respect to the temperature and the normalized water content can be observed in Fig. 5.10, calculated using Eq. (5.32). As can it be observed, the diffusivity has a peak around 27.5% of the normalized water content. It is also relevant to observe that the diffusivity increases as the temperature increases.

As the back-diffusion plays a vital role in the water balance between the anode and cathode, it is crucial to work within a high range of this parameter to avoid unbalanced water content. Eq. (5.33) shows the back diffusion flux, J_{bd} , calculated

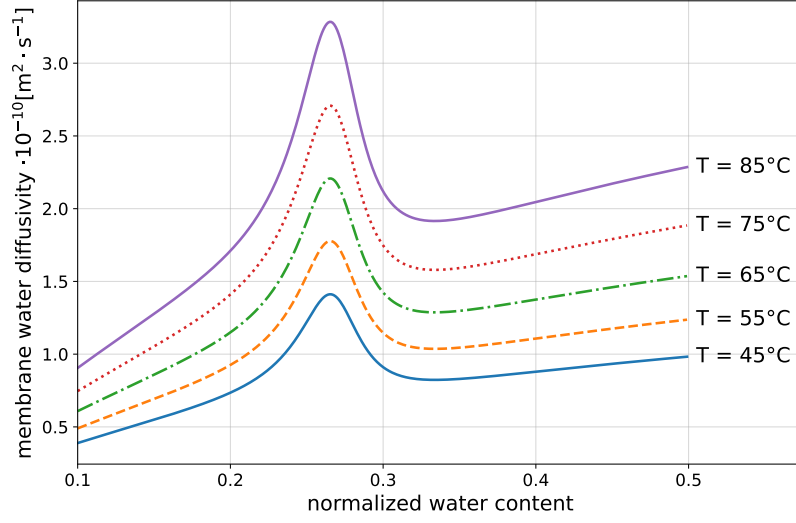


Figure 5.10: Water diffusion coefficient function of the normalized water content and the temperature.

from with the diffusion coefficient, $D_{\lambda,T}$ and the gradient of water content, λ_m , with respect the thickness of the membrane represented by the axis z .

$$J_{bd} = -D_{\lambda,T} \frac{d\lambda_m}{dz} \quad (5.33)$$

The code implemented of the Back diffusion model can be found in Appendix D.1.7.

5.4.3 GDL water and gas diffusion

Gases diffusion

The GDL enables the diffusion of gases from the flow field to the CL. The GDL allows fuel access below the channel's rib zones and provides stiffness to the MEA. Despite being a good electron conductor, the inherent ohmic resistance produces electric loss voltage to the cell.

In the GDL three phenomena occur a) gas or gases diffusion from the channel to the catalytic layers, b) water steam diffusion, and c) liquid water removal.

PEMFC can be fed with pure gases, O_2 in the cathode and H_2 in the anode or with gas mixtures. Gas mixtures are more commonly used in the cathode as air is used as fuel, mainly containing O_2 , N_2 , and steam water.

Gases transport in a porous media can be described by four different models a) Knudsen flow, where it is considered that the collisions of molecules occur mainly between molecule and walls instead of molecule to molecule; b) viscous flow, which considers that the flow is pressure gradient driven where non-laminar flows may occur which may be modeled using Forchermeier term [138]; c) continuum diffusion, where flow is induced by concentration gradient; and d) surface flow, where gas molecules move with the surface where they are absorbed [139].

In this thesis, only Knudsen and diffusive flow are considered. Knudsen diffusivity should be used when the ratio of the mean molecular free path, $\overline{x_{mfp}}$ and the pore diameter, d_p is lower than 10^{-3} , Eq. 5.34 [140].

$$K_n = \frac{\overline{x_{mfp}}}{d_p} \quad (5.34)$$

Knudsen flow is considered since, in the GDL, the porosity and the pore size significantly affect the wall collisions. Therefore the Knudsen correction to the diffusive coefficient must be applied. The continuum diffusion is also considered within the GDL since the pressure gradients are small, and the gases move according to concentration gradients.

The Stefan-Maxwell (S-M) model is typically used when considering multi-component gases. The use of the S-M model requires a high computational effort since it requires computing each element's diffusion coefficient at every time step, as the diffusion coefficient depends on the molar concentrations at that time, Eqs. (5.35, 5.36) where J_i is the i^{th} compound gas flux, \mathcal{A}_{ij} the S-M matrix of fluxes in each coordinate direction, the term \mathbf{C} is the sum of concentrations at each point, C_j the gas concentration of the j^{th} compound and D_{ij} is the binary diffusion coefficient of the i^{th} compound on the j^{th} compound.

$$\sum_j \mathcal{A}_{ij} J_j \nabla \left(\frac{C_j}{|\mathbf{C}|} \right) \quad (5.35)$$

$$\mathcal{A}_{ij} = \frac{1}{|\mathbf{C}|} \begin{cases} \sum_{l \neq i} \frac{-C_l}{D_{il}} & \text{if } i = j \\ \frac{C_i}{D_{ij}} & \text{if } i \neq j \end{cases} \quad (5.36)$$

To reduce the S-M model's computational cost, the multi-component Fick model is used instead. This approach is allowed since the binary values of diffusion coefficients obtained are similar [124] and reduces the computational effort by not re-calculating the diffusion coefficients depending on the gas concentration. In Eq. (5.37), the multi-component Fick model is described.

$$\mathbf{J} = -|\mathbf{C}|D_{ij}\nabla\left(\frac{C_j}{|\mathbf{C}|}\right) \quad (5.37)$$

This simplification allows faster calculations since the diffusion coefficients are constant, as they do not depend on the actual concentration distribution at each element.

Despite being a faster solution than the S-M model, the Fick multi-component is still computationally expensive since it requires computing the overall gas distribution. Therefore a single-component gas assumption is applied in the model. Other authors already use this assumption [141] as it reduces the number of calculations by considering the gas moving as a single component.

The Knudsen diffusivity coefficient is the extra coefficient that considers the effect of the molecules impacting the wall instead of free space diffusion; this is calculated using the gas molecular weight, M_i , and the pore diameter, d_p , Eq. (5.38).

$$D_{K_n} = \frac{2}{6} \left(\frac{8RT}{\pi M_i} \right)^{0.5} d_p \quad (5.38)$$

The actual gas diffusivity in a porous media, which takes into account the diffusivity of the pure gas in free space and the effect of the molecule-to-wall impacts, D_i^* , is defined by the Knudsen coefficient and the single component diffusion coefficient, D_i , the concentration change rate, Eq. (5.39).

$$D_i^* = \left(\frac{1}{D_i} + \frac{1}{D_{K_n}} \right)^{-1} \quad (5.39)$$

The Darcy diffusion model is defined for the gas pressure gradient, P , and the modified diffusion coefficient, D_i^* , Eq. (5.40), where ϵ is the porosity of the medium, τ the tortuosity of the medium defined as the ratio between the length of the path and the straight distance between the start and end of the path.

$$J = -\frac{\epsilon}{\tau^2} \frac{D_i^*}{RT} \nabla P \quad (5.40)$$

Liquid water diffusion

The GDL is formed by a porous media which allows gases and liquid water to move within it. The GDL provides consistency to the MEA while allowing the expel of liquid water and the flow of gases to the catalytic layers.

Liquid transport in a porous media may be calculated using numerical or analytical methods. Within numerical methods, the pore-network approach [142], or Lattice-Boltzman method [143] are the most common methodologies used. Analytically, the capillary pressure equation is used in [144]. Leverett's capillary method is used in this thesis since it has a lower computational cost compared with the previously mentioned numerical methods.

The capillary pressure of water describes liquid water transport at each point of the GDL. The capillary diffusivity depends on the amount of water at each point. Leverett's equation, Eq. (5.41), defines the capillary pressure dependency with respect to water content [110, 145]. Therefore the water flow depends on the amount of water, s , and the capillary pressure in the porous medium, P_c , Eq. (5.42). The capillary pressure is a function of the medium's permeability, K , the static contact angle, θ_s , the liquid surface tension, γ , and the porosity of the medium, ϵ . The liquid flow is due to the difference in capillary pressure and is shown in Eq. (5.43).

$$J(s) = \begin{cases} 1.417(1-s) - 2.120(1-s)^2 + 1.263(1-s)^3, & \text{if } \theta_s \leq 90^\circ \\ 1.417s - 2.120s^2 + 1.263s^3, & \text{if } \theta_s > 90^\circ \end{cases} \quad (5.41)$$

$$P_c = \gamma \cos \theta_S \sqrt{\frac{\epsilon}{K}} J(s) \quad (5.42)$$

The water flow produced due to the gradient of capillary pressure, $q_{H_2O,l}$ is calculated using the permeability of the medium, K , the kinematic viscosity of the fluid, ν , and the relative permeability, k_{rl} , calculated by Eq. (5.44).

$$q_{H_2O,l} = \frac{k_{rl}}{\nu} K \frac{\partial P_c}{\partial x} \quad (5.43)$$

$$k_{rl} = s^3 \quad (5.44)$$

The Leverett equation is nonlinear regarding the water content; therefore, the water removal rate shows nonlinear behavior. As an example, considering the model evaluated in a configuration where the fraction of liquid water has a value of 0.25 (typical value used on the simulations), the diffusion coefficient would be at the order of $10^{-7} \text{ m}^2 \cdot \text{s}^{-1}$ (considering a fiber diameter of $9 \text{ } \mu\text{m}$ and the value of the static contact angle is 130°). The diffusion coefficient is measured for each element flowing through a specific media, and the flow calculation is evaluated [110, 146].

GDLs typically have values between $150\text{-}300 \text{ } \mu\text{m}$ thick (z axis, Fig. 3.1). On the other hand, their width and depth are designed to ensure the coverage of the overall active area of the cell. In the case of the analyzed cells, the width and depth are 50 mm or 100 mm versus the $150 \text{ } \mu\text{m}$ of the GDL. Therefore $z \ll x$ or y . Consequently, it may be assumed that the main component of water flux is in the xy axis. This approach allows for reducing the dimensionality of the diffusion model from a 3D model to a 2D. The z water movement will be analyzed independently in subsection 5.4.5. To solve the liquid water movement model through the GDL, the finite difference method (FDM) is applied. Specifically, the FDM used is the forward time-centered scheme (FTCS) described in subsection 6.4.3.

As shown in Eqs. (5.41-5.44), the capillary pressure is a function of the GDL permeability to water, K , the GDL porosity, ϵ , and the normalized water content,

s , expressed by the Leverett equation, as well as the contact angle of the GDL, θ_s , and the surface tension of water γ . The GDL design parameters that can impact the capillary pressure are K and ϵ .

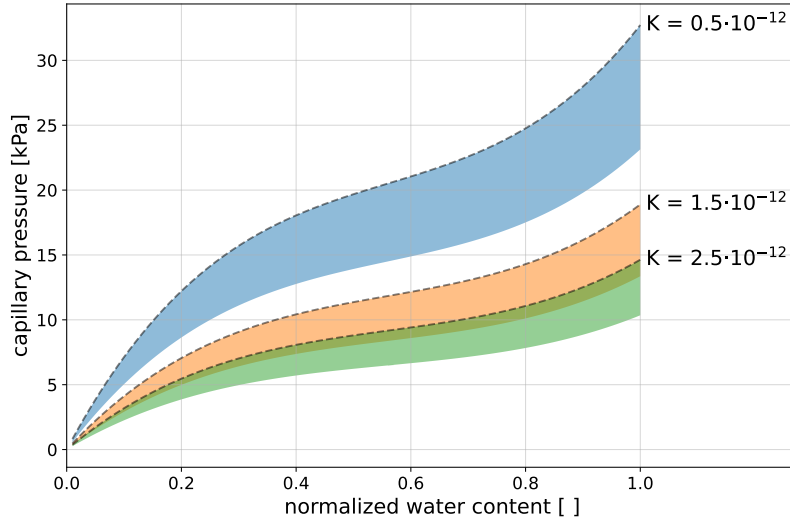


Figure 5.11: Capillary pressure function of a) the normalized water content on the x-axis, b) in the GDL porosity range (40-80%) the colored areas, and c) different values of GDL water permeability, K .

In Fig. 5.11, a sensitivity analysis of water content is performed to observe the relative contribution of some parameters to the overall capillary pressure. The capillary pressure is analyzed within the porosity range of 40% and 80% described by each area fill, where the dashed line corresponds with the 80%. The capillary pressure behavior for different permeability values is shown in the figure with different colors. The permeability values are indicated on the right side of the figure. From the data in Fig. 5.11 is observed that the impact of the GDL porosity on the capillary pressure becomes more relevant as the medium permeability decreases. On the other hand, an increment of a magnitude order in permeability produces an approximate three time increase in capillary pressure.

5.4.4 GDL water evaporation and condensation

Evaporation of water from the GDL occurs when the partial pressure of water in the steam phase is lower than the saturation pressure of water inside the GDL;

otherwise, if higher, steam water from the flow field condenses into the GDL. The water evaporation is described by Eq. (5.45) and condensation by Eq. (5.46) [4, 147]. When condensation occurs, steam water converts into liquid in the GDL, and in evaporation, liquid water from the GDL is converted into steam water. If the partial pressure of steam water in the flow field is at maximum (saturated), the GDL does not transfer water into the flow field in the gas phase.

$$S_{evp} = k_{evp}\epsilon s \frac{\rho_{H_2O}}{M_{H_2O}} (P_{H_2O} - P_{H_2O}^{sat}) \quad (5.45)$$

$$S_{con} = k_{con}\epsilon(1 - s) \frac{X_{H_2O}}{RT} (P_{H_2O} - P_{H_2O}^{sat}) \quad (5.46)$$

The evaporation rate from the GDL to the flow field, S_{evp} , is modeled by Eq. (5.45) where k_{evp} represents the evaporation constant, ϵ the porosity of the media, s the normalized volumetric water fraction in the media, ρ_{H_2O} the density of the liquid, P_{H_2O} and $P_{H_2O}^{sat}$ represent the partial water pressure and the saturated partial pressure of water respectively, and finally, M_{H_2O} the molar weight of water.

Water condensation rate, S_{con} , from the flow field to the GDL is represented by Eq. (5.46), function of the relative humidity in the flow field and the amount of water in the GDL. The parameter k_{con} represents the condensation constant, and X_{H_2O} is the mole fraction of water steam.

Other studies found that the evaporation rate also depends on the moisture content of the porous medium [148]. Over certain moisture content in the GDL (in the study case 40%), the drying rate mainly was constant but dramatically decreased at lower moisture levels, Eq. (5.47).

$$S_{vl,evp} = \begin{cases} sk_{evp}\epsilon \frac{\rho_{H_2O}}{M_{H_2O}} (P_{H_2O} - P_{H_2O}^{sat}), & \text{if } s \leq 40\% \\ 0.4k_{evp}\epsilon \frac{\rho_{H_2O}}{M_{H_2O}} (P_{H_2O} - P_{H_2O}^{sat}), & \text{if } s > 40\% \end{cases} \quad (5.47)$$

In this thesis, this approach has been considered setting the stability evaporation rate at 40%.

The algorithm of the GDL water evaporation and condensation model is described in Appendix 9 and 10.

The evaporation rate is critical in the overall performance of a cell to maintain adequate water content in the GDL and the membrane, which allows the removal of water in the proper amount. When there is lack of evaporation, the water content in the GDL increases, and water is removed in liquid form, subsection 5.4.5. The water evaporation rate may be controlled by GDL design parameters such as the porosity, ϵ . But mainly, the evaporation rate is managed by tuning the cell operating temperature and the relative humidity of the gas feed. Fig. 5.12 shows a sensitive analysis of the three parameters mentioned before and their evaporation rate. For example, Fig. 5.12 shows the evaporation rate considering a GDL of thickness $253 \mu\text{m}$.

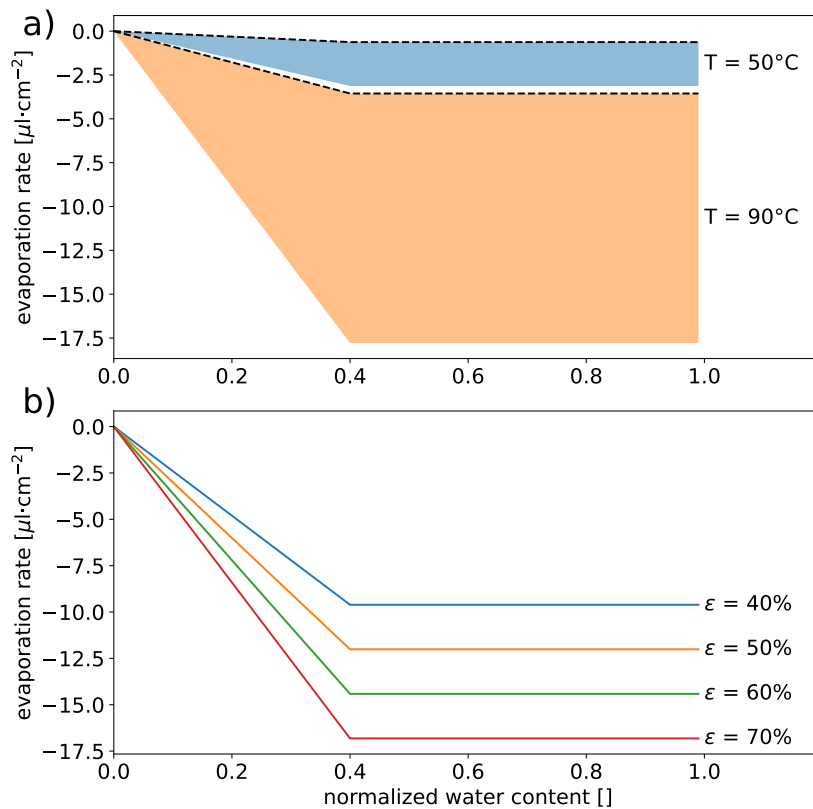


Figure 5.12: a) the evaporation rate function of the RH (the colored area from 50% to 90%, the dashed line) and the temperature and b) the effect of the porosity in the evaporation rate considering RH 50% and temperature 80°C for different normalized water content in the GDL.

Fig. 5.12-a shows the evaporation rate for two given temperatures 50°C and 90°C , the colored range represents the different evaporation rates from 50% to 90%

(dashed line) relative humidity. As can be observed, the impact on the relative humidity is more significant when the temperature is higher, producing higher evaporation rates. The cell operation at lower temperatures results in a lower evaporation rate, producing cell flooding and higher performance in-homogeneity.

Fig. 5.12-b shows the effect of GDL porosity on the evaporation rate, being the evaporation rate higher when the porosity is higher.

5.4.5 GDL liquid water removal

Liquid accumulates inside a porous media until the capillary break-through pressure is reached, then the liquid creates a path along the porous media to be evacuated. The capillary break-through pressure threshold, p_{bt} , depends on the material's physical structure [149, 150]. The liquid water drained from a pore is stopped when the capillary pressure decreases, p_{st} due to the reduction in water amount inside the porous media.

This phenomenon happens when the draining path previously created by the liquid is discontinued [151, 152]. This phenomenon is described using pseudo-code in Alg. 3. The p_{bt} and p_{st} values are obtained experimentally, as they depend on the hydrophobic surface treatment of the GDL, the pore diameter, the pore size distribution, and the thickness of the GDL. The drain is, for simplicity, assumed to occur at a constant flow rate, q_{drain} , multiplied by the current water content in the pore, Eq. (5.48). In Fig. 5.13, an example of the relationship between the capillary pressure and the actual normalized maximum water content in the pore, s , is represented. In Fig. 5.13 is also shown the capillary break-through pressure, p_{bt} , plus the steady decayed water capillary pressure, p_{st} .

The drainage flow, S_{drain} , can be described using Eq. (5.48), where q_{drain} is a reference flow when the p_{bt} is surpassed.

$$S_{drain} = q_{drain}s \quad (5.48)$$

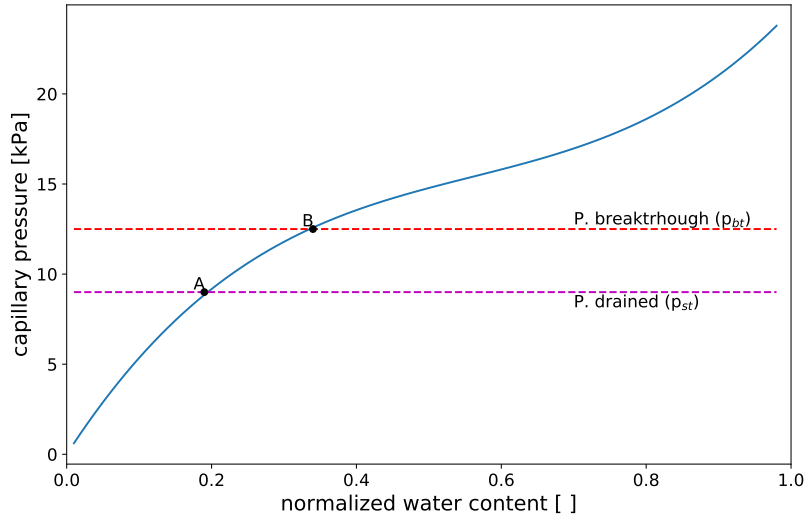


Figure 5.13: Example of the relationship between actual pore water content and capillary pressure in a given GDL with the maximum water capillary pressure breakthrough, p_{bt} , and the stable decayed capillary pressure, p_{st} .

The water break-through only occurs in the cell under stream-saturated conditions. Typically for a current density of $0.7 \text{ A}\cdot\text{cm}^{-2}$, the water generation is $65 \text{ nL}\cdot\text{s}^{-1}\cdot\text{cm}^{-2}$ and the evaporation rate ranges from 2000 to $12000 \text{ nL}\cdot\text{s}^{-1}\cdot\text{cm}^{-2}$ [153], therefore under non-saturated conditions the evaporation rate is capable of removing the water generated during the operation. But under saturated conditions, the evaporation rate is null; therefore, the water content in the GDL is solely removed via break-through producing sudden drops over the surface of the GDL, reducing the water content inside the GDL.

This phenomenon occurs when a saturated gas stream is fed into the cell's flow field or when the gas stream becomes saturated due to the evaporation occurred inside the cell.

The liquid water removal in the GDL algorithm is explained in Appendix D.2.2.

5.5 Flow field model

In this section, a description of the flow field model is presented.

The objective of the flow field model is to represent the flow of multiple species that feed the catalytic layers and the water liquid droplets' movement along the

flow field pattern. Furthermore, the exchange of species within the flow field and the GDL is considered. The phenomena considered in the flow field model are:

- The pressure losses are due to the effect of gas flow and liquid water movement, the impact of the geometry of the channels, and the result of the water droplets acting as an obstacle to the gas flow.
- The variations in gas concentration.
- The variation of RH.

The model is considered a pseudo-2D because a 1D model in the axis of the length of the channel is mapped over the 2D plane of the MEA. This simplification enables the evaluation of the impact on RH and gas concentration in the fuel cell plane while providing a fast-solving methodology.

5.5.1 Gas pressure drop along the flow field

The gas flow through a duct produces a pressure drop due to the friction with the walls. The pressure losses due to the flow of gases in a channel are represented by Darcy-Weisbach's equation, Eq. (5.49). It describes the pressure losses on a channel, ΔP , for a defined length, L , in a tube defined by its hydraulic diameter, D_h , with a gas flow of density, ρ_g , at a certain gas speed, u_g . In order to consider the humidity, the density of the air is calculated as a mix of the dry air density and water content per free flow volume.

$$\frac{\Delta P}{L} = f \frac{\rho_g u_g^2}{2D_h} \quad (5.49)$$

The Darcy friction coefficient, f , is calculated in the laminar regime and turbulent flow using the Colebrook-White expression, Eq. (5.50), which depends on the relative roughness of the tube, e_r and the Reynolds number, Re .

$$f = \begin{cases} \frac{64}{Re}, & \text{if } Re < 2300 \\ \left(-\log \left(\frac{e_r}{3.7D_h} + \frac{2.51}{Re\sqrt{f}} \right) \right)^{-1}, & \text{if } Re \geq 2300 \end{cases}, \quad (5.50)$$

The methodology is valid for straight channels with uniform section. In order to consider the turns on the channels and the obstacles in the gas path, the equivalent length method is used. The equivalent length method is a simplification strategy to describe a pressure drop of a feature, such as a corner, a restriction, or others, in terms of transforming this feature into an equivalent tube length. Experimental tables are used to calculate the equivalent tube distance for a given geometry, and its changes [154]. The tables allow calculating the equivalent length, L_e , as a function of the hydraulic radius of the tube. This method allows using Darcy-Weisbach's equation to represent other channel geometries.

The presence of droplets in the channel impacts the gas pressure. This phenomenon is taken into account by considering the droplets as static obstacles for the gas flow model in the flow field, reducing the flow section of gas, which increases the pressure losses. This approach was also used in [155], simplifying the pressure drop calculation due to the presence of water droplets on the channel.

Since the droplet is an obstacle in the gas flow, the gas must flow around the droplet. Consequently, the effective channel section is reduced, Eq. (5.51).

The cross-sectional area of a droplet is described in section 5.5.3 in Eq. 5.64, A_d . The speed of the gas flowing by the side of the droplet increases as a consequence of the effective section reduction. The gas speed passing by a droplet, u_{ef} , may be expressed by Eq. (5.52) for rectangular channels.

$$A_{ef} = w_c h_c - A_d \quad (5.51)$$

$$u_{ef} = \frac{\dot{m}_g}{\rho_g} \frac{1}{w_c h_c - A_d} \quad (5.52)$$

Where w_c and h_c are the width and the height of the flow field channel, which by subtracting the droplet cross-sectional area, A_d , the effective section, A_{ef} , where the gas may flow through is obtained. To calculate the gas speed passing by the droplet, \dot{m}_g is the mass flow of the gas, and ρ_g is the density of the gas.

This strategy simplifies the calculation of the pressure losses while also considering the presence of a liquid droplet, interfering with the gas flow in the flow field and increasing the pressure drop.

5.5.2 Concentration variation of species in the flow field

As gases flow along the flow field, their concentration varies, due to electrochemical reactions, since the reactants are consumed and water is generated. The consumption of reactants produces a decrease in the overall channel pressure as the mass in the gas is reduced (section 5.4.1). The evaporation of the water generated in the cathode (subsection 5.4.4) produces variations in the RH of the channel. The presence of liquid water on the surface of the channel also affects the RH when droplet evaporation occurs (subsection 5.5.4). In Fig. 5.14, a scheme of a) the liquid water evaporation phenomenon from a droplet, b) the liquid water evaporation from the GDL, c) the condensation phenomenon from the stream in the flow field to liquid water into the GDL; and d) the reaction consumption for the i^{th} gas component is shown.

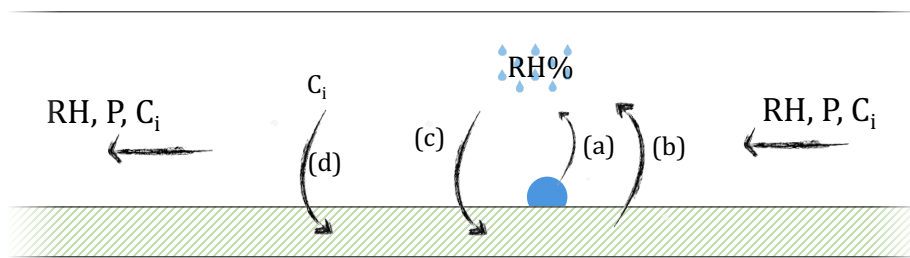


Figure 5.14: Scheme of phenomena involved the variation of concentration of species in the flow field. The phenomena described are a) evaporation from a droplet; b) liquid water evaporation from the GDL; c) steam condensation into liquid water in the GDL; and d) consumption of reactants

The variation of species concentration in the channel and the GDL are calculated for each cell area. The following subsections describe the change in RH and fuel concentration.

Relative humidity

Relative humidity increases or decrements along the flow field path due to the evaporation or condensation of water from and into the GDL. To update the values of the relative humidity of the channel, the values of evaporation and condensation are calculated (subsection 5.4.4) by taking into account the channel's flow and the current RH (Φ).

Relative humidity, Φ , depends on the steam saturated pressure, $P_{H_2O}^{sat}$ and the actual steam pressure, P_{H_2O} or the total amount of water mass in the steam phase m_v^{sat} and m_v respectively, Eq. (5.53). The mass evaporation flow rate depends on the volumetric flow of gases, Q_g , Eq. (5.54).

$$\Phi = \frac{P_{H_2O}}{P_{H_2O}^{sat}} = \frac{m_g}{m_g^{sat}} \quad (5.53)$$

$$\dot{m}_v = m_g^{sat} Q_g \Phi \quad (5.54)$$

$$m_{x_i}^g = m_{x_{i-1}}^g + m_{evp} - m_{cond} + m_{d,evp} \quad (5.55)$$

In Eq. (5.54) \dot{m}_v represents the actual mass of steam water given a flow rate, Q_g , and a relative humidity, Φ . By applying sequentially Eqs. (5.53-5.55) and then recalculating the relative humidity using Eq. (5.53), the humidity evolution along the channel is calculated. Where in Eq. (5.55) m_{evp} is the evaporated mass of water from the GDL, calculated from Eq. (5.47); m_{cond} is the water condensation from the flow field to the GDL calculated from Eq. (5.46); and $m_{d,evp}$ the evaporated water from the droplet present on the flow field calculated from Eq. (5.82).

Water removal via evaporation can be observed via the change in the RH along the channel path. The actual RH along the flow field is the parameter that drives the amount of water removed via evaporation. In Fig. 5.15 1D simulation of a linear channel is performed to observe how the RH along the channel changes depending on the gas flow and the operating temperature. The simulation considers

0.4 normalized water homogeneously distributed along the channel, an initial RH of 50% in a flow field of $1 \times 1 \text{ mm}^2$ cross-section with a current density of $0.7 \text{ A}\cdot\text{cm}^{-2}$.

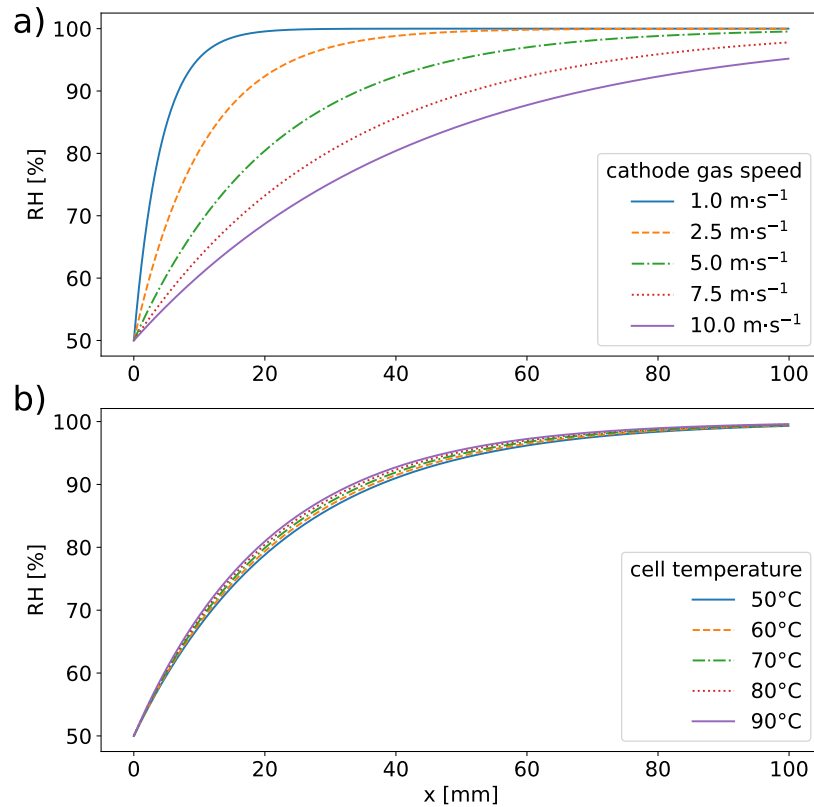


Figure 5.15: RH evolution along the linear channel of 100 mm length with respect to a) different cathode airflow speeds and b) the operating temperatures

Fig. 5.15-a shows how higher gas flows have greater humidity carrying capacity (also it can be observed in Fig. 5.16-a as the water content in the gas stream in [g] of water per [m³] of gas). Higher gas stream speed will produce more even humidification but also a faster drying of the GDL, especially near the inlet where the RH is the lowest.

Regarding RH changes along the channel concerning the temperature, no differences are shown in Fig. 5.15-b. This is because the evaporation rate is calculated using the actual vapor pressure and the saturation pressure, which evolves with the temperature at the same rate the carrying capacity does. Therefore no expected changes on the RH profile, which changes in temperature are expected. But, as illustrated in Fig. 5.16-b, the carrying capacity increases as temperature

increases; consequently, the drying capacity of the cell increases. Lower drying capacities, especially at low flow rates, will produce RH saturation, and therefore the water excess in the cell would be removed in liquid form, section 5.4.5.

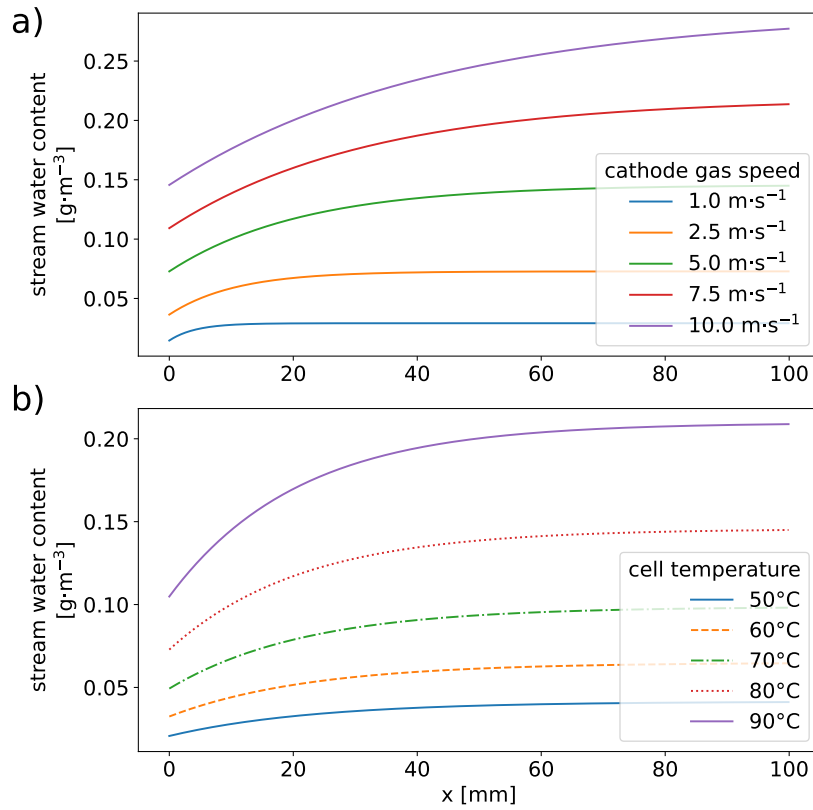


Figure 5.16: Water content evolution along the linear channel of 100 mm length with respect to a) different cathode airflow speeds and b) the operating temperatures

Gases concentration

The fuel gases are consumed along the flow field path; therefore, their concentration evolves along the cell are modified. The gas concentrations on the flow field are calculated using the total mass of fuels in the flow field and their consumption along the cell.

Considering C_i the molar concentration of the i^{th} gas component, the flow of moles, n_i , can be obtained from the total gas flow, Q_g , and the total pressure of the flow field, P_{tot} , Eq. (5.56).

Consider that S_i represents the fuel consumption, by definition, is negative in Eqs. (5.4, 5.5).

$$\dot{n}_i = \frac{C_i P_{tot} Q_g}{RT} + S_i \quad (5.56)$$

5.5.3 Droplet movement model

Water expelled from the GDL accumulates in the form of liquid water droplets over the surface of the GDL. Those droplets move along the channel forced by the gas flow. The movement of a droplet along a channel due to gas dragging force is widely studied in literature [123, 125, 156, 157]. Those droplets may move at different speeds due to their different volumes; consequently, one or more drops can be close enough to clutter themselves in a single drop.

To ensure gases properly feed the catalytic layer, the flow fields of PEM fuel cells are typically designed with parallel channels, either in the shape of serpentes, multi-parallel serpentes, or others. In these designs, a water droplet is forced to turn on each corner of the channel to keep advancing to the cell's gas outlet. Those corners increase the adhesion forces of the droplet with the GDL surface or the walls of the channel, which reduces the droplet speed and may cause extreme cluttering and drops coalescence, which may lay to channel clogging. When a droplet is moving along the channel, it may a) only be sliding over the GDL surface or over one channel wall, b) sliding over the GDL surface and one or more walls of the channel, c) clogging the channel. For each case, the adhesion forces will be different. An approximation model to evaluate drop movements in those cases is being proposed.

This section presents a modified and simplified version of the model described in [123]. The simplification aims to reduce the number of calculations required to solve each step of droplet movements in the model simulation.

Droplet movement over one surface

The model described in [123] describes the movement of droplets over one surface in three parts: a) the geometrical description of the droplet with its receding and advancing angles, which depend on both the contact angle and droplet deformation, b) the dragging forces model and c) the adhesion forces model. These different parts are described in the following subsections, which will conclude by solving the overall droplet dynamics model.

The droplet dynamics is defined by Eq. (5.57) where m_d is the droplet mass, $x_{d,CM}$ is the position of its center of masses and F_{adh} and F_{drag} are the adhesion and dragging forces respectively. These forces depend on the relative position of the droplet's gravity center with respect to the front point of the droplet (A), Fig. 5.18. The model considers that the gravity force ensures contact with a known surface. Depending on the cell's orientation, this surface may be a channel wall or the GDL surface. By general rule, the developed model will consider that the surface on which the droplets move is the GDL.

$$m_d \ddot{x}_{d,CM} = F_{adh} - F_{drag} \quad (5.57)$$

Eqs. (5.58-5.59) describe the dragging and adhesion forces. In Eq. (5.58), ρ_g represents the density of the gas, u_g the gas speed, C_D the aerodynamic coefficient, and A_d the droplet cross-sectional area.

$$F_{drag} = \frac{1}{2} \rho_g u_g^2 C_D A_d \quad (5.58)$$

The adhesion force is calculated by the integral over the contact line, the perimetrical line of the interface between the surface and the droplet, Eq. (5.59).

$$F_{adh} = -\gamma \int_0^l \cos \theta(l) \cos \psi(l) dl \quad (5.59)$$

Where $\psi(l)$ represents the angle with respect to the center of the droplet over the surface, the azimuth, l the length of the circular perimeter, γ the surface tension, and θ the contact angle, Fig. 5.17 [158].

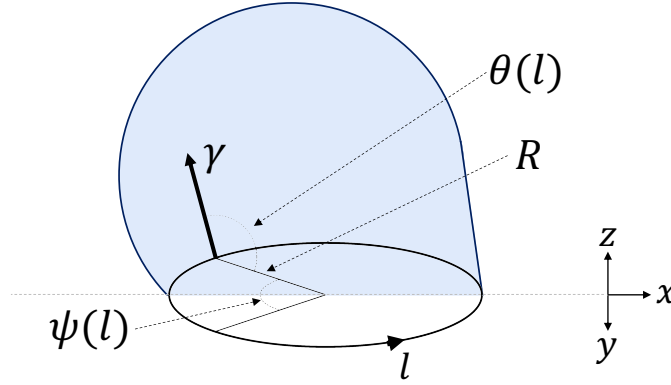


Figure 5.17: Scheme of adhesion force of a droplet deformed by gas flow

These forces depend on the droplet's geometry, as described in the following subsections.

Droplet geometrical model

The geometrical model of a moving droplet is described with the advancing angle, θ_A , the receding angle, θ_R its volume, V_d , and its static contact angle, θ_S , Eq. (5.60). In Fig. 5.18, the effect of the gas flow applied over a water droplet over a hydrophobic surface is shown.

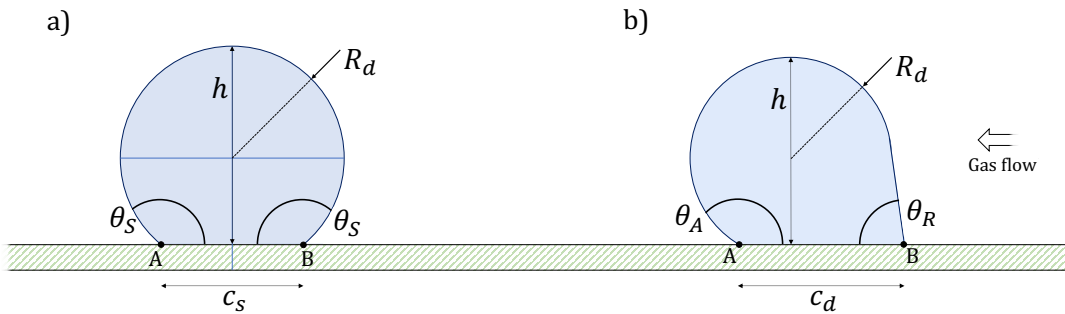


Figure 5.18: Gas flow effect on a droplet geometry over a hydrophobic surface a) when the gas flow is zero (static) and b) when the gas flow is positive (dynamic)

The chord length, the distance on the longitudinal axis of the drop in contact with the surface, is the key parameter on the geometrical model as it is considered constant.

The static chord length, c_S , is derived from droplet the volume using Eq. (5.61) and is described by the static droplet radius, R_d as shown in Fig. 5.18. The chord length is a characteristic parameter that remains constant at any droplet deformation. The term c_D will be used to define the dynamic chord, calculated using the Eq. (5.62).

$$V_d = R_d^3 \left(\frac{4}{3}\pi - \frac{\pi}{3} (1 + \cos \theta_S)^2 (2 - \cos \theta_S) \right) \quad (5.60)$$

$$c_S = 2 \sin(\theta_S) \left[\frac{V_d}{\frac{4}{3}\pi - \pi (1 + \cos(\theta_S))^2 \cos(\theta_S)} \right]^{\frac{1}{3}} = 2 \sin(\theta_S) R_d \quad (5.61)$$

$$c_D = \frac{R_d}{\sin(\theta_R)} (1 + \sin(\theta_A) \sin(\theta_R) - \cos(\theta_A) \cos(\theta_R)) \quad (5.62)$$

In addition, the droplet area (the sectional area perpendicular to the gas flow), A_d , and the droplet perimeter (contact line between the droplet and surface), P_d , can be described using Eqs. (5.63-5.65) where A_1 is used as an intermediate variable to shorten Eq. (5.64).

$$A_1 = \theta_A + \theta_R - \sin(2\theta_A) + \sin(\theta_A - \theta_R) \quad (5.63)$$

$$A_d = \frac{R_d^2}{2 \sin \theta_R} \left(A_1 \sin \theta_R + \sin^3 \frac{\theta_A - \theta_R}{2} \sin \frac{\theta_A + \theta_R}{2} \right) \quad (5.64)$$

$$P_d = R_d(\theta_A + \theta_R) + 2 \frac{R_d \sin\left(\frac{1}{2}(\theta_A - \theta_R)\right)}{\sin(\theta_R)} \sin\left(\theta_A + \frac{1}{2}\theta_R\right) \quad (5.65)$$

From Eqs. (5.60, 5.62) the relation between θ_A and θ_R can be obtained for any value of droplet deformation shape, droplet volume, and static contact angle.

The droplet height from the bottom to the top, h_d , Eq. (5.66), is also important and only depends on the droplet radius and its advancing angle.

$$h_d = R_d(1 - \cos \theta_A) \quad (5.66)$$

Adhesion forces

A droplet over a surface has an attachment force consequence of the surface tension of the liquid and the area in contact with this surface that acts upon any other external force that produces the movement of the droplet.

By integrating Eq. (5.59), using a cylindrical approximation [159, 160], under the consideration of a spherical droplet, the adhesion forces are described by the difference of receding, θ_R , and advancing, θ_A , angles and the width of the droplet, t_d , Eq. (5.67).

$$t_d = \frac{V_d}{P_d} = R_d \frac{\frac{4}{3}\pi - \pi(1 + \cos(\theta_S))^2 \cos(\theta_S)}{\theta_S - \frac{\sin(2\theta_S)}{2}} \quad (5.67)$$

Therefore the droplet adhesion force is described by Eq. (5.68), where R_d and γ represent the radius and the surface tension of a spherical liquid droplet, respectively. The k_{adh} is a friction constant that depends on the droplet shape. The value of k_{adh} varies between $\frac{\pi}{2}$ and $\frac{\pi}{4}$ depending if the values are obtained analytically or through finite element [125]. The droplet width is represented by t_d and γ , the surface tension of the droplet's liquid.

$$F_{adh,S} = k_{adh}\gamma t_d (\cos \theta_R - \cos \theta_A) \quad (5.68)$$

Contact line adhesion force

The contact line adhesion force depends on the velocity of the droplet over the surface [161] and is defined as shown in Eq. (5.69) using the term $F_{adh,D}$ to differentiate it from the static contribution $F_{adh,S}$.

$$F_{adh,D} = C_{CL} t_d u_d \quad (5.69)$$

Where C_{CL} is the contact line force constant, t_d is the droplet width, and u_d is the droplet speed. This force component is not typically considered, since models, as presented in [160], aim to calculate the detachment force, and only the static adhesion force, $F_{adh,S}$, is used. The model presented in this thesis considers the dynamic forces, including the droplet velocity effect.

Drag force

Due to the pressure created by the gas flow acting on a droplet, a force appears in the flow direction, the drag force. This force depends on the droplet's relative speed with respect to the air and the area of the droplet, A_d .

The dragging force, Eq. (5.70), is driven by the density of the medium, which is pushing the droplet, ρ_g . This density may vary due to the relative humidity and the gas temperature. The dragging force is also a function of the gas velocity perpendicular to the droplet, u_g , and the aerodynamic coefficient of the droplet C_D .

$$F_{drag} = \frac{1}{2}\rho_g u_g^2 C_D A_d \quad (5.70)$$

Some authors used CFD techniques to study the impact on C_D due to the channel dimensions and the gas's velocities, proposing a polynomial relationship Eq. (5.71) [125, 162, 163].

$$\begin{aligned} F_{drag} = & 5.81 - 4.82Re_{h_c-h_d} + 1.67Re_{h_c-h_d}^2 \\ & - 0.29Re_{h_c-h_d}^3 + 0.03Re_{h_c-h_d}^4 - 8.66 \cdot 10^{-4}Re_{h_c-h_d}^5 \\ & - 1.43(\theta_A - \theta_R) e^{-0.959Re_{h_c-h_d}} \end{aligned} \quad (5.71)$$

Where $h_c - h_d$ represents the height difference between the channel and the flow field, Re is the Reynolds number, and θ_A and θ_R are the advancing and receding angles. In the simulations shown in this thesis, the C_D value used is 0.5 since it is considered that the droplet has a spherical shape [159] and simplifies the calculations required.

Droplet dynamic movement simplification

One of the objectives of the model presented is to allow a fast simulation procedure for PEMFCs' water management. For single droplet studies, the model presented by [159] is accurate but computationally expensive when the simulation contains multiple simultaneous droplets. To reduce the computational effort, some approximations have been conducted:

- The water droplets will be subject to a slight deformation with respect to a defined point.
- The adhesion force may be considered the sum of individual single contacts. When the droplet is in contact with multiple surfaces with the same hydrophobic characteristics.
- The droplets do not split while advancing.

The simplification of the geometrical deformation model of the droplet will be assumed to be within a limited range for its static position ($\Delta\theta$). With this assumption, the dragging and adhesion forces can be reduced to droplet volume dependent and the droplet speed; therefore, geometric calculations can be avoided.

The droplet deformation is limited within a range of $\Delta\theta$. This difference only is caused by the effect of the gas flow inside the channel and the droplet speed. Therefore the adhesion force ($F_{adh,S}$ and $F_{adh,D}$ combined to F_{adh}) will only depend on the droplet size, $t_d(V_d)$, the gas speed, u_g and the droplet speed, u_d , as shown in Eqs. (5.72-5.73). In Eq. (5.73), $k_{v,d}$ has to be adequately adjusted to represent the droplet deformation in a given hydrophobic surface.

$$F_{adh} = 2\gamma t_d \Delta\theta \quad (5.72)$$

$$\Delta\theta = k_{\theta 0} (\pi - \theta_S) + k_{v,d} u_d \quad (5.73)$$

As described in work [161], the overall dynamic force depends on the droplet's static portion and the droplet's velocity component. In the model presented, $k_{\theta 0}$

represents the static adhesion force related to the actual static contact angle, and $k_{v,d}$ depends on the channel type and the contact angle of each particular surface. Therefore, the simplified model used to represent the droplet movement dynamics is described by Eq. (5.74).

$$m_d \ddot{x}_{d,CM} = \frac{1}{2} \rho_g u_g^2 C_D A_d - 2\gamma t_d (k_{\theta 0} (\pi - \theta_s) + k_{v,d} u_d) \quad (5.74)$$

The algorithm which represents the droplet advancing model can be found in Appendix D.3.

Variables sensitivity of droplet dynamics model

In the previous section 5.5.3, the model to represent the dynamic movement of a droplet was presented. In this section, an analysis of the droplet speed function of droplet volume is studied. In Fig. 5.19, the effect of the gas speed on the droplet speed and the droplet volume is shown. In this example, it is considered that the droplet travels along the channel only in contact with the GDL surface.

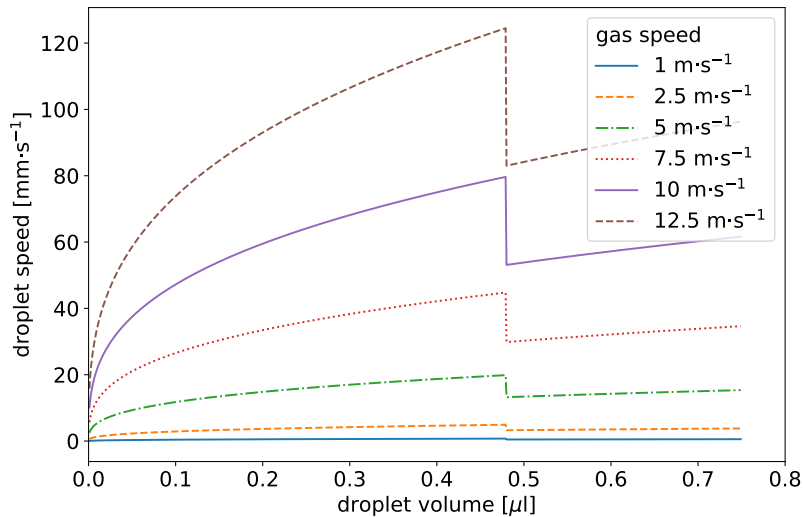


Figure 5.19: Steady state droplet advance speed function of droplet volume and gas speed

The example of Fig. 5.19 is simulated considering a channel width and height of $1 \times 1 \text{ mm}^2$. As observed, the droplet advancing speed is low for very low gas speeds,

making it difficult to remove the liquid droplets from the flow field. For higher gas velocities, a higher droplet advancing speed is achieved. As the droplet size increases, the height increases, the area of the droplet exposed to the gas stream increases, and the droplet friction increases due to an increase in the contact area. In Fig. 5.19, the sudden drop in droplet speed, around a droplet volume of $0.475 \mu\text{l}$, is due to this value being the critical size of the droplet where its diameter is equal to the channel width. Therefore, the droplet is in contact with three walls instead of one.

Fig. 5.20 analysis of the droplet speed function of the contact angle for a gas speed of $5 \text{ m}\cdot\text{s}^{-1}$. As can be observed, the difference in contact angles does not have a more significant impact on the steady droplet speed, but it does in the critical droplet volume, in which the droplet becomes in contact with three walls instead of one, increases as the contact angle increases.

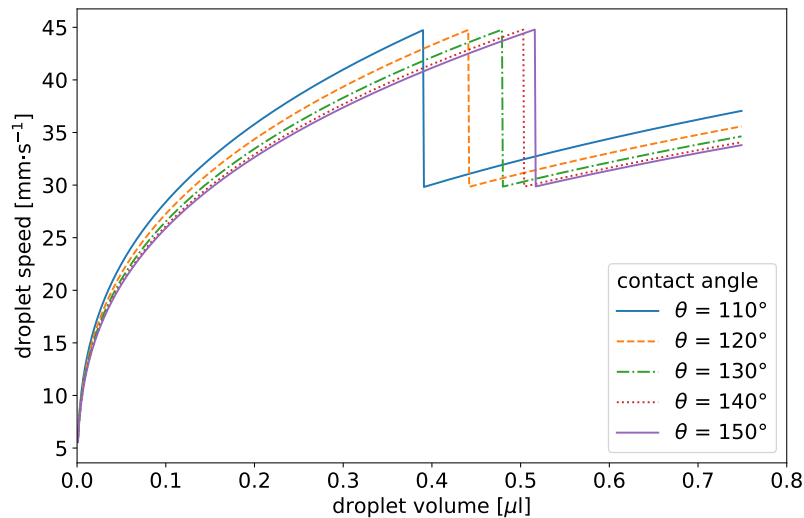


Figure 5.20: Steady state droplet advance speed function of droplet volume and contact angle

Droplets clattering

In the model presented, multiple droplets are considered, which may move simultaneously along the flow field. As described in subsection 5.5.3, the forces that a droplet receives depend on its volume; therefore, droplets with different sizes will move at different speeds. Due to those speed differences, despite droplets

appearing at any point over the surface of the GDL, they may collide at a specific moment. When this happens, droplets will clutter into a single bigger droplet. This phenomenon is also called droplet coalescence.

The coalescing model of multiple droplets into a single bigger droplet can be explained by considering two droplets of different sizes, R_i , separated by a distance d as shown in Fig. 5.21 [162]. At this point, the two droplets will not coalesce into one.

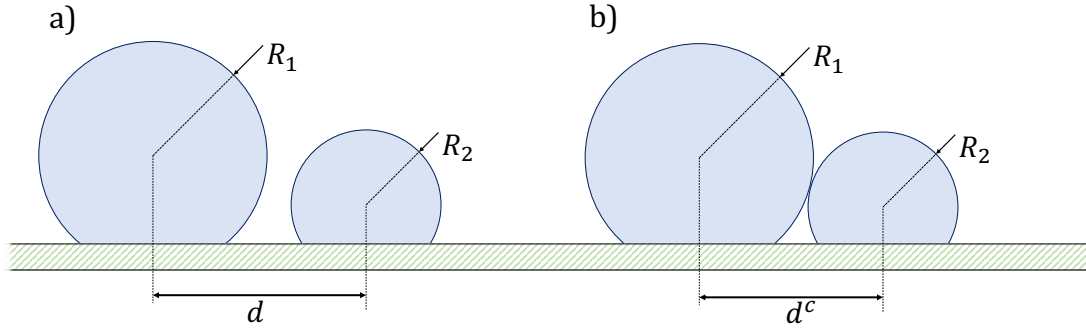


Figure 5.21: a) droplets at a distance which will not coalesce, b) droplets at the critical coalescence distance

In Fig. 5.21-a, the droplets 1 and 2 with their respective radiuses, R_1 and R_2 , being $R_1 > R_2$, and considering the droplets spherical, therefore using the static contact angle θ_S , the droplets will contact when the distance between droplets centers, d , which is equal to the sum of both droplets radiuses $R_1 + R_2$, becoming the critical distance, d^c , Eq. (5.75).

$$d^c = (R_1 + R_2) \leq |R_1 \cos \theta_S| + |R_2 \cos \theta_S| \quad (5.75)$$

In the model, a droplet with the combined volume will replace the previous droplets when this occurs. The position of this new droplet is calculated by assuming the equilibrium of forces, forming the new droplet at the averaged volume-weighted distance. The position of the cluttered droplet with respect to droplet 1 is defined by Eq. (5.76).

$$d^n = \frac{R^3}{R_1^3 + R_2^3} d \quad (5.76)$$

Droplet movement over multiple surfaces

The previously presented model describes the behavior of a droplet over one surface inside a channel. A droplet may contact more than one surface in a real flow field. Some authors have studied multiple surface contact of the droplets in the flow field [164]. Furthermore, the contact angle may differ depending on the surface hydrophobic chemical treatment of each wall of the channels (for example, GDL with PTFE).

The previously presented model has been extended to account for multiple contact surfaces.

A model simplification is applied to simulate the impact of multiple surface contact, considering that the droplet is in punctual contact with each surface. This simplification provides a significant reduction in the computational cost. Otherwise, a new geometrical model deformation would be required. Then, the adhesion force model presented is valid considering the number of walls and their respective contact angle.

$$F_{adh} = K_{n,walls} \sum_{i=0}^{n_{walls}} F_{adh,i} \quad (5.77)$$

As shown in Fig. 5.22, the contact surface of the droplet with the wall is lower on the simplified model than on the original model presented in [160]. To compensate for this effect, a multiplying factor has been added to the adhesion forces, $K_{n,walls}$. For simplicity, the algorithm implemented considers that the droplet is always located in the center of the channel. With this approach, the droplet may be in contact with a) a single wall, the GDL surface, b) 3 walls simultaneously if the channel height, h_c , is higher than the channel width, w_c , or c) 4 walls, if the width of the channel is equal or lower than its height, $h_c \leq w_c$. Therefore depending on the droplet's diameter and the channel's dimensions, 1, 3, or 4 contact surfaces of the channel with the droplet will be considered.

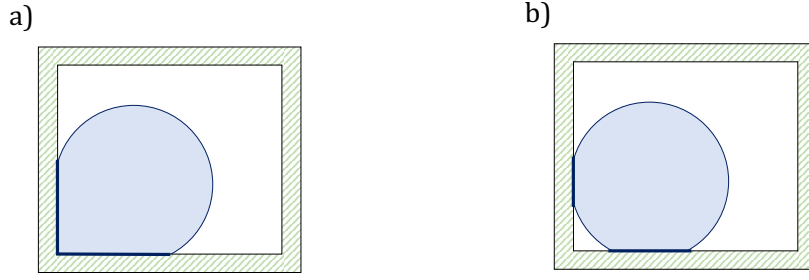


Figure 5.22: Scheme of a droplet contacting with two perpendicular surfaces of the channel, a) real contact and b) simplification

5.5.4 Droplet water evaporation

Water droplet evaporation kinematics is widely studied in [165]. This model allows analyzing how a droplet evaporates while moving due to the airflow function of its velocity. A modification of this model is used to account for droplet evaporation, correcting the equivalent area factor, $k_{d,evp}^*$, in the model, Eq. (5.78). The correction uses the ratio of the actual droplet area exposed to the gas flow, A_d , and the area of a free droplet, $A_{d,free}$.

$$k_{d,evp}^* = \frac{A_d}{A_{d,free}} \quad (5.78)$$

In the previously mentioned study [165], the evaporation is calculated as the change in diameter of the free-falling droplet with respect to time, Eq. (5.79). The evaporation rate depends on the droplet exposed area, which is calculated using the droplet diameter, D_d , some experimental parameters, a_{evp} and b_{evp} , which depend on ambient conditions and liquid properties, and $u_{a,d}$, which is the relative velocity between the gas flow and the droplet. The original equation presented describes the time evolution of the droplet's diameter, Eq. (5.79).

$$\dot{D}_d = \frac{a_{evp}}{D_d} \left(1 + b_{evp} \sqrt{D_d u_{a,d}} \right) \quad (5.79)$$

Parameters a_{evp} and b_{evp} are temperature dependant, and they are represented by Eqs. (5.80-5.81). Where η is the gas viscosity at T_g , M_{H_2O} is the molar weight of water, ΔP^{vap} is the difference in vapor pressure from the surface of the droplet

to the ambient, ρ_{H_2O} is the liquid water density, ρ_g is the gas density, R is the gases constant, T_g is the gas temperature, γ the liquid surface tension, $D_{v,f}$ is the diffusion coefficient for steam molecules in the saturated film around the drop [165].

$$a_{evp} = \frac{4\gamma M_{H_2O} D_{v,f} \Delta P^{vap}}{\rho_{H_2O} R T_g} \quad (5.80)$$

$$b_{evp} = 0.276 \left(\frac{\rho_g}{\eta D_{v,f}^2} \right)^{1/6} \quad (5.81)$$

Considering the droplet as a perfect sphere, the Eq. (5.79) can be converted into volumetric evaporation rate, $S_{d,evp}$, as shown in Eq. (5.82).

$$S_{d,evp} = \left(\frac{1}{2} \frac{a_{evp}}{D_d} \left(1 + b_{evp} \sqrt{D_d v_{a,d}} \right) \right)^3 \left(\frac{4}{3} \pi - \frac{1}{3} \pi (1 + \cos \theta_S)^2 (2 - \cos \theta_S) \right) \quad (5.82)$$

5.5.5 Droplet water re-absorption

Section 5.4.5 described how liquid water is expelled from the GDL to the flow field when the water content in the pores of GDL exceeds the water capillary pressure. The water drained appears as droplets in the flow field over the surface of the GDL.

Once over the surface of the GDL, these droplets can be gradually re-absorbed in steam form into the GDL if some conditions are met, such as low water content in the GDL and sufficient liquid volume in the channel.

The condition of low water content in the GDL is more easily met on the anode side since the consequence of the electro-osmotic drag produces a flow of water from the anode to the cathode, the anode tends to be dryer. This effect makes water droplet re-humidification a possibility for fuel cells. The re-absorption model can be mathematically described as shown in equation (5.83).

$$J_a = \delta_{V,d} D_{ra} (s_{min} - s_{r,i}) \quad (5.83)$$

5.6 Conclusions

This chapter has described the models which allow the analysis of the performance of a pseudo-3D PEM fuel cell considering the water management in the flow field. The models are oriented to allow the simulations with low computational cost.

The submodels presented in the chapter are:

- The electrochemical model relates the gas fuel pressures, the operation temperature, and the species concentration with the current density and voltage of the cell.
- The MEA model also accounts for water diffusion due to the electro-osmotic drag and back-diffusion in the electrolyte. The MEA model also describes the GDL water and gas diffusion in the plane of the GDL. Furthermore, the MEA model considers the water evaporation and condensation from the GDL and the liquid water removal.
- The flow field model can represent the variations in RH and gas concentrations as well as the pressure drop consequence of the movement of the gas and the fuel consumption.
- The droplets' movement in the flow field model allows to simulate the effect of liquid water on the channel and how excess water is removed when dragged by a gas flow.

The complete model allows to calculate the total amount of water and gases and their distribution along the GDLs and membrane, the RH, liquid water, and fuel concentration along the flow field, and the spatial cell's performance. Also, the model can dynamically represent the variables of the cell.

In the next chapter, chapter 6, the numerical implementation of the submodels and the simulation procedure that allows the solver to work efficiently are presented.

6

Numerical implementation and simulation procedure

Contents

6.1	Introduction	101
6.2	Simulation methodology	102
6.3	Simulation procedure	106
6.4	Submodels numerical implementation	110
6.4.1	Iterative solving	111
6.4.2	Flow field discrete model	112
6.4.3	Finite time centered scheme	113
6.4.4	Droplet re-absorption numerical implementation	116
6.4.5	Liquid water removal from the GDL	117
6.5	Conclusions	118

6.1 Introduction

In the previous chapter 5, the equations that represent the behavior of the different physical phenomena are described. The models can be implemented in various forms to obtain different physical representations as described in section 4.3. In this chapter is presented the global simulation methodology used to implement a fast pseudo-3D model and the numerical implementation of specific models.

The simulation methodology section describes how the models of different dimensionality are interconnected among them and which is the solving procedure.

The numerical procedures section describes the most characteristic algorithms used to solve specific parts of the models, such as the iterative solving method used, the flow field algorithm using a pseudo-2D model, the diffusion algorithm, the liquid droplet re-absorption, and liquid water removal from the GDL.

6.2 Simulation methodology

A simulation methodology has been developed aimed at the reuse of the submodels that constitute the complete model, the flexibility of using different types of compilers and programming languages for the simulation of each submodel to optimize the computational cost. The proposed simulation methodology uses a set of independent submodels connected sequentially, allowing each submodel to be calculated independently since the submodels have an entity by themselves, providing the interface to connect the submodels through the variables exchanged. The variables of the submodels are calculated in sequence, and the results of the variables at the current time step are exchanged with the other submodels for the next time step.

This type of modeling has the advantage that each submodel can be individually validated and then integrated into the overall structure.

The models are implemented in two programming languages, Python and C++. The lower computational effort models have been implemented in Python 3.7, using the standard libraries, providing flexibility and simplicity in the development stage of the modeling implementation.

On the other hand, high computational cost submodels, such as gases and water diffusion on the GDL or the electrochemical reactions, have been implemented in C++ language since a large number of spatial discretization elements have to be computed. In addition, the iterative algorithms implemented for the dynamic simulation procedure require a faster computation to reduce the simulation time.

The combination of these two strategies enables the implementation of faster simulations of the complete model with the flexibility provided by Python language for the lower computational effort submodels and the high performance provided by compiled C++ algorithms.

Fig. 6.1 shows a high-level schema of the simulation methodology where it can be observed which are the submodels implemented in Python and which in C++ (with the red dashed rectangle).

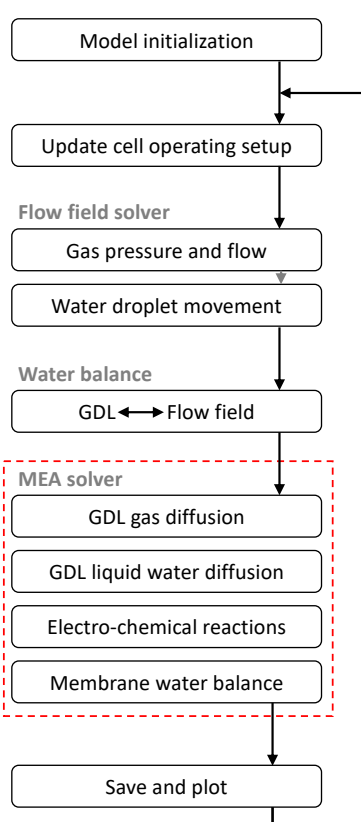


Figure 6.1: Simulation flow chart with marked in the dashed red rectangle the submodels implemented in C++

The simulation solver is divided into stand-alone submodels, which are linked together. Those submodels are grouped into main functions or represent a particular physical layer of the cell and are solved sequentially.

The simulation procedure is composed of a 6-step solver (Fig.6.1):

1. Initialization. This stage creates the data structure required to initialize the submodels. Divides the plane xy into its mesh, calculates the shape of the

channels, groups the mesh elements into regions, and associates its regions to a channel. Moreover, it initializes all the variables. This process is only performed once at the start of the simulation.

2. Update cell operating setup. The simulation methodology proposed enables to obtain the dynamic results of the studied variables. Therefore, some time-dependent conditions, such as a change in the inlet gas's RH, flow rate, and droplet injection in the flow field, among others, may be established to be modified during the simulation time.
3. Flow field solver. This model updates the pressure gradients along the channel, the species concentration, and the position and size of the droplets.
4. Water Balance. This stage simulates the exchange of water between the GDL and the flow field of the cell and the water phase change between liquid and steam. To correlate both models, a region grouping strategy is used. This strategy correlates a group of elements from the GDL to a group of elements from the flow field to perform the exchange of species (described in subsection 6.4.2).
5. MEA solver. The MEA solver is composed of four main procedures:
 - GDL gases diffusion. The GDL is represented by a 2D planar model. This procedure calculates the gas flow along the GDL for the current time step in the plane xy .
 - GDL water diffusion. As in gas diffusion, the water diffusion procedure calculates the liquid water flow in the GDL in the plane xy .
 - Electrochemical reactions. The current and voltage of each spatial point of the cell are evaluated. The electrochemical reaction is calculated by each discretization element of the membrane, which shares the discretization mesh with the GDLs.

- Membrane water balance. This stage calculates the water exchange between the cathode and anode's GDL, solving for back-diffusion and electro-osmotic drag submodel. The membrane is discretized with the same number of elements as the GDLs; therefore, there is a 1-to-1 relationship between an element of the cathode and the anode GDLs. This solver iterates over all the elements in the xy plane.
6. Save data and plot. The last stage of the simulation solver is responsible for saving the current time step data and plotting the results if required. In order to save computational time, this stage is not executed at every simulation step.

By iterating on previous simulation stages, the dynamic of the water behavior and other cell variables can be calculated.

Compiling part of the simulation procedure using C++ programming language is particularly necessary when simulating cells with larger surface area or smaller spatial discretization.

The model can simulate the cell in two operating modes a) galvanostatic mode (constant current) and b) potentiostatic mode (constant voltage).

In galvanostatic mode, the resistance of the external electric load has to vary during operation. Therefore, in this operation mode, the electro-chemical reactions are simulated multiple times in each iteration step, calculating the voltage that obtains the desired overall current in the cell. In this case, reducing the number of discretized elements in the simulation becomes critical as the cell is solved multiple times to reach a solution.

In potentiostatic mode, the solution is more direct since, with a constant voltage, the current generated at each spatial point of the cell can be calculated in a single iteration.

6.3 Simulation procedure

To analyze the xy cell homogeneity of the cell's variables, a spatial meshed discretization in the xy plane is performed. A compromise solution has been achieved in the proposed simulation spatial discretization mesh size and time step between obtaining simulations with low computational cost and stable simulations with accurate results. A smaller mesh size or time step may imply a high computational cost simulation without clear benefits on the quality of the simulated results [166].

The most demanding simulation procedure regarding the mesh discretization size (requires a small mesh size to obtain accurate simulations) is the submodel representing the gas diffusion in the GDL, for future references this mesh will be called xy -mesh or planar-mesh. This simulation procedure is calculated using the finite difference method (FDM), subsection 6.4.3. FDM discretizes the total spatial and temporal domain into smaller segments in which the solution is approximated by solving the linear finite differences equations using the nearby nodes values. These methods are typically designed to use equally spaced meshes, simplifying the calculations.

In the aim to reduce the computational effort, the flow field models use a dedicated 1D mesh which will be referenced as linear-discretization. The linear-discretization is a uni-axis path divided into small length elements, dL , where each channel element has values of pressure, species concentration, resistivity, the droplets' discrete position, or other variables. The advantage of using a 1D model is that the interactions of each element, L_i , are only with the precedent and succeeding elements, reducing the total number of elements and the number of interactions between them. This linear-discretization is later converted into a pseudo-2D model by assigning the position of each L_i element to a 2D plane.

The complete pseudo-3D model combines two different models, the MEA and the flow field model, which use two different space discretizations. Fig. 6.2 shows an illustrative representation of the a) xy -mesh, b) the linear- discretization, and c) the

linear-discretization converted into a pseudo-2D. Therefore, the models previously described have two types of discretization

1. *xy*-mesh. The finest mesh (element size) is used in the MEA simulation procedure to describe:
 - The electrochemical model.
 - Electro-osmotic drag and back-diffusion.
 - Water movement inside the GDL.
 - Gas diffusion inside the GDL.

This 2D discretization is the smaller element used in the overall simulation solver and, therefore, is the procedure involving the largest number of discretization elements. The proper discretization size must be small enough to ensure the solver's stability, as explained in section 6.4.3.

2. Linear-discretization. Linear discretization is used for models applying to the flow field or to the interface between the flow field and the MEA, those models are:
 - Flow field gases balance.
 - Water droplets movement.

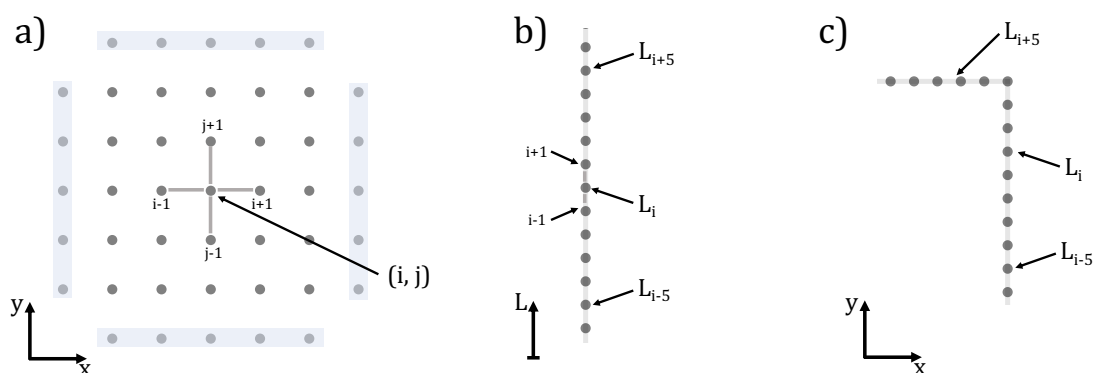


Figure 6.2: Illustration showing a) the MEA *xy*-mesh, b) the linear-discretization, and c) the linear-discretization converted into a pseudo-2D approach.

As the xy -mesh and the linear-discretization have different sizes, and the elements may not correlate one-to-one, a supra mesh called regions is created. The regions mesh groups elements from xy -mesh and the linear-discretization to relate those spaces physically. The region's element supra-set is the discretization used to represent the water and species balance between GDL and the flow field.

A discretization region represents the same physical spatial area. The elements corresponding with a region have similar state values that can be averaged and create an artificial central node. The element variables' averaged values are exchanged with the corresponding region at the interface.

The objective of using the regions is to connect the flow field and the MEA models, which are only applied to areas with a channel. The rest of the MEA nodes are not interconnected with the linear-discretization and are used for internal MEA model calculations. Therefore, no regions are created to represent those areas. In Fig. 6.3, an illustration of the xy -mesh and the linear-discretization together with regions that group elements from both numerical spaces are shown.

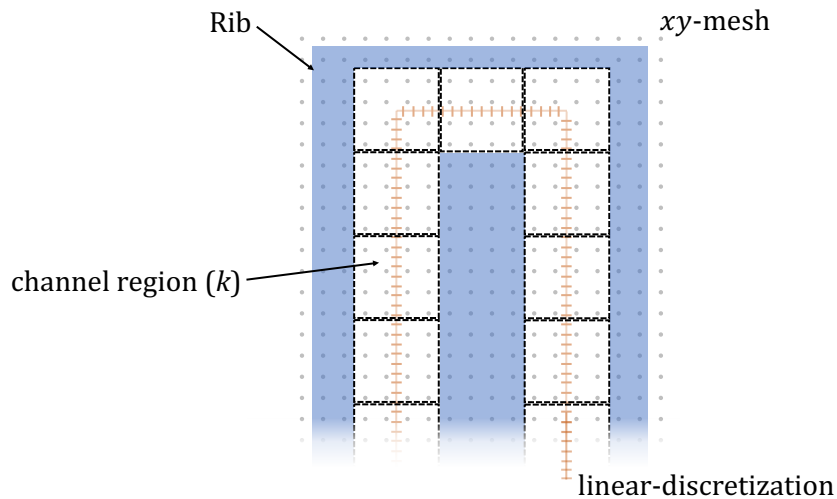


Figure 6.3: Scheme of grouping GDL discretization elements into flow field discretization regions

The complete pseudo-3D model is composed of five levels, depicting the catalytic layers, the five levels are: a) cathode flow field, b) cathode GDL, c) membrane, d) anode GDL, and e) anode flow field. The PEM fuel cell is, in terms of physical

structure, symmetrical as described in section 3.2, therefore to describe the interrelation of physical models, the generic terms flow field, GDL and membrane will be used if the inter-relation applies to both sides, for instance not specifying cathode GDL to the cathode flow field, otherwise anode and cathode will be specified. Fig. 6.4 shows the five levels of which the model is composed and the two possible interconnections (A) from the flow field to GDL using regions, and (B) in the MEA using elements of both GDL and membrane discretization.

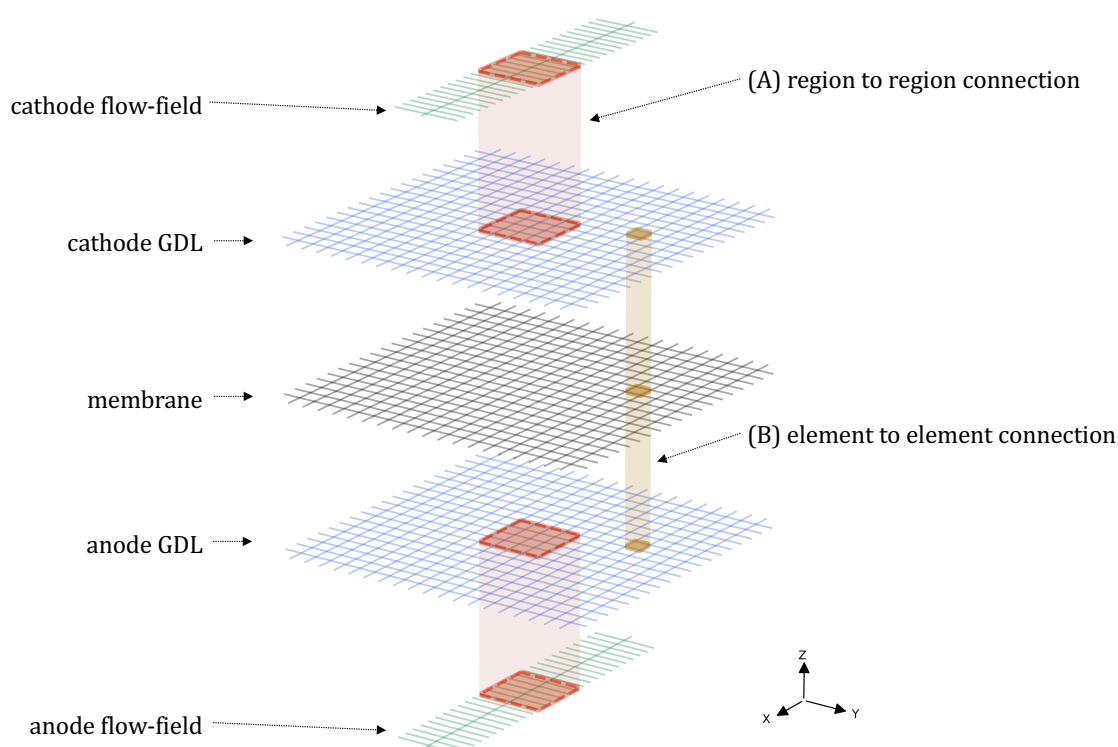


Figure 6.4: Illustration representing the two kinds of discretization, the xy -mesh and the linear-discretization with the regions used in the complete model

Interconnection (A) connects two models with different types of discretization. Therefore an intermediate element, the region, is used to connect those two meshes. A region, as described in section 6.3, is a group of discretization elements that are close enough to consider the state variables have similar values. The region discretization is absolute for all models, is in the same xy position, and has the same size. Each model's elements inside the region will depend on their discretization size. The flow field to GDL interconnection (A) shares:

- The fuel gas partial pressure transported from the flow field to the GDL.
- The steam water transported from the flow field to the GDL.
- The evaporation and condensation of water from and to the flow field to the GDL.
- The liquid water removed from the GDL to the flow field.
- Position of the liquid droplets on the flow field to the GDL.

This exchange of state values is done by updating the corresponding model element-value list or reading a file containing the actual element-value list.

Interconnection (B) connects the state values of both GDLs with the membrane. The membrane and GDL models are computed in C++ and are calculated using all the elements; therefore, the interconnection is performed element-to-element, in here the interconnection shares:

- The water amount transported from cathode GDL to anode GDL by electro-osmotic drag and back diffusion.
- The water content diffused from the GDL to the membrane.
- The partial pressure of the gases that feed the catalytic layers.

With those two interconnections, independent discretizations are adequately connected to compute the cell's overall performance.

6.4 Submodels numerical implementation

This section presents some particular features of numerical calculation methods applied in the simulation of the submodels.

6.4.1 Iterative solving

Some submodels are solved directly by substituting the values of the current state on the equation modeling the phenomenon. For instance, the actual voltage of a spatial point in a cell can be obtained by the water content, the gas concentration, the current density, and the physical parameters of the cell Eq. (6.1).

$$V = E(P_{H_2}, P_{O_2}) - V_{act}(j) - V_{ohm}(s, j) - V_{con}(j) \quad (6.1)$$

Although obtaining the current density of a point by the voltage, water content, and gas concentration cannot be solved by inverting the previous equation. Therefore, numerical methods are required. An iterative algorithm is a method to find a specific value by setting a seed and calculating from this starting point through successive approaches. A seed must be a known solution of the model. From this point, iterative models change the value, in this case, the current density, to observe how the voltage changes and consequently reduce the error with respect to the target voltage.

The chosen iterative method is the binary search algorithm. This method is simple and robust in finding a solution for a continuous and monotonic function or a sorted list of values. The algorithm's starting point is the limits within the solution that must exist (upper lu_0 and lower ll_0). For instance, in the case of finding the root of a number, N , the limits may be considered the number itself and 0. With those limits, the approximated solution may be the middle point of lu_0 and ll_0 , ml_0 . With this value, the function is evaluated, therefore, in the example of the root of a number $ml \cdot ml = res$. The result obtained, res , is compared with the number target value the root is sought. If $N > res$, the guess is too small, the limits must be updated to $lu_1 = lu_0$ and $ll_1 = N$, and a new ml_1 is obtained. If $N < res$, the limits update in the opposite direction, updating the upper limit to the current tested point $lu_1 = N$ and $ll_1 = ll_0$.

For simplicity, it is typically sought for the difference between our tested value minus our target to minimize the difference to zero, $0 = f(x) - y_0$. The main procedure is described below using the example of \sqrt{x} , Alg. 1.

Algorithm 1 Pseudocode of the binary search algorithm for the example of the root search of the $f(x) = \sqrt{x}$

```

 $x_i$ ;                               /* Value the root of needs to be found*/
 $x_{max} \leftarrow x_i$ ;                /* max and min ranges on the binary search*/
 $x_{min} \leftarrow 0$ 
while  $error < error_{min}$  do
   $x_i \leftarrow (x_{max} - x_{min})/2 + x_{min}$ ;          /* Current test point*/
   $x2 \leftarrow x * x$ ;                               /* Test point evaluation*/
  if  $x2 > x_i$  then                                 /* Is test point is greater than target */
    |  $error \leftarrow |x_{max} - x_{min}|$   $x_{max} \leftarrow x_i$ 
  else if  $x2 < x_i$  then                             /* Is test point is lower than target */
    |  $error \leftarrow |x_{max} - x_{min}|$   $x_{min} \leftarrow x_i$ 
  else  $error \leftarrow 0$ ;
end

```

This method has been applied in the different algorithms:

- Calculating current density for a given voltage when the cell operates in galvanostatic mode using Eq. (5.27).
- Calculating the current density of a mesh element when the cell operates in potentiostatic mode using Eq. (5.27).

6.4.2 Flow field discrete model

The flow field model, as described in section 5.5, is a linear 1D model in the direction perpendicular to the channel section. The flow fields in a fuel cell are in the plane xy ; therefore, the 1D flow field model must be adapted to a 2D model. To use the 1D model in a 2D plane, an element mapping (assignment of some nodes of one discretization as relative nodes to another discretization) for the 1D flow field model to the xy GDL mesh is required.

In subsection 5.5.1, a method was explained to relate the turns of the channel in the flow field and the gas pressure drop.

The overall flow field is uniformly discretized in length by dl . This discretization enables setting different characteristics to each flow field element, such as contact angle, gas speed in the element, and friction forces, which are used to calculate the droplet dynamics.

As an example of the 1D to 2D mapping strategy, Fig. 6.5 shows a scheme of the same channel represented in 1D and 2D. In Fig. 6.5-a, a channel turn of a 2D flow field is represented. Its equivalent model in a 1D dimension is shown in Fig. 6.5-b. To properly represent the 2D channel in 1D, the equivalent length method described in section 5.5 is used.

In subsection 5.5.1, a method was explained to relate the turns of the channel in the flow field and the gas pressure drop.

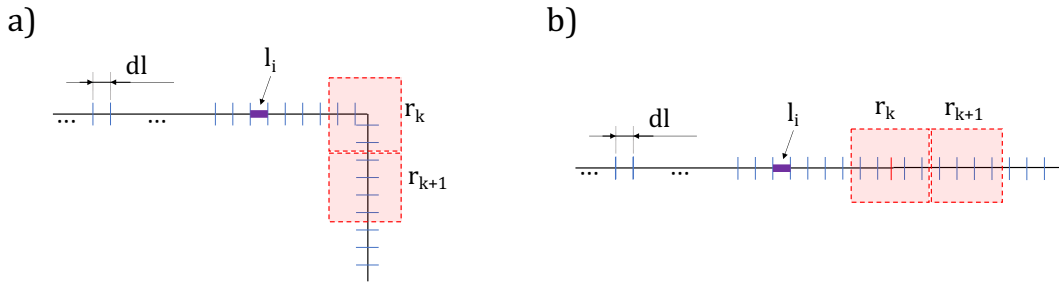


Figure 6.5: Representation of a) flow field's channel turn in the 2D plane with the used discretization l_i , and the regions r_k , as explained in section 6.3, and b) the same channel (a) using the 1D discretization

The equivalent length method is used to calculate the effect of a channel turn represented with a 1D model. The 1D model is mapped over a 2D surface. This mapping allows connecting the interface of the flow field and the GDL discretization elements, the regions. The regions cover the channel area of the xy plane. This discretization is shared among all the z layers of the model. Each discretized component will have its nodes assigned to specific regions, which are used to relate the physical phenomena from one layer to the other. For example, this shared discretization allows connecting the 1D droplet position, RH, and gas pressure values of a region to the GDL actual geometric point.

6.4.3 Finite time centered scheme

To solve the diffusion equation, multiple numerical schemes have been developed. The most known scheme for its simplicity is the Forward Time Centred Scheme (FTCS), based on the Finite Difference Method (FDM) [167]. FTCS is a single-step, fully explicit, first-order time and second-order space accurate scheme, $O(x^2, t)$.

There exist other schemes, such as the Crank-Nicholson scheme. The Crank-Nicholson scheme is an implicit method divided into two steps. It is both time and space second-order accurate, $O(x^2, t^2)$, which provides faster solutions since it allows the usage of a bigger number of elements and reduces the number of operations. For simplicity, the FTCS scheme is used in this thesis.

To apply FTCS, an equally spaced mesh is required to enable a constant space interval between an element and its contiguous, dh , as shown in Fig. 6.6.

The FTCS scheme is described using Eq. (6.2).

$$\frac{C_k^{t+dt} - C_k^t}{dt} = D \frac{C_{k-1}^t - 2C_k^t + C_{k+1}^t}{dh^2}, \quad (6.2)$$

Where t is the current time step, $t + dt$ is the next time step. The element k is the current discretization element being evaluated, and $k - 1$ and $k + 1$ are the two contiguous elements on the i^{th} axis, being i the axis x , y or z in a 3D model. C is the concentration of the specie diffused on the k^{th} element and D the diffusion coefficient in the porous media.

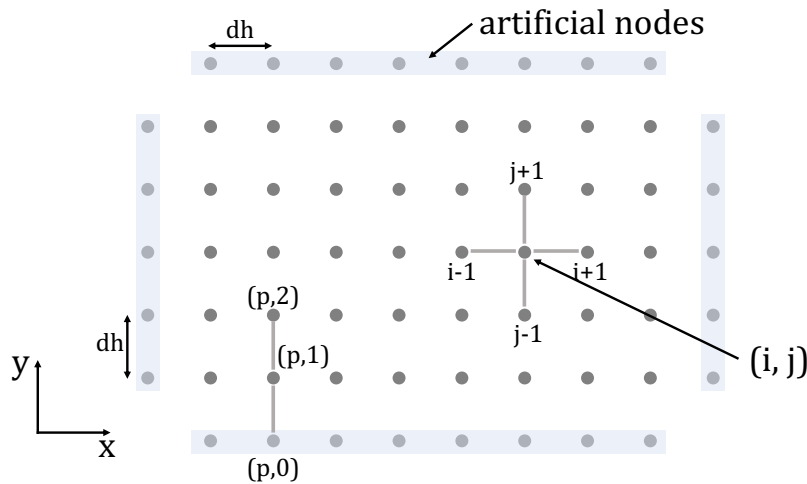


Figure 6.6: Example of FDM mesh using artificial nodes for Neumann boundary condition using the FTCS approach.

The time interval may vary along the simulation period even though the maximum time step is limited to satisfy stability conditions. This maximum

time step is related to the space interval used, dh , and the diffusion coefficient, D , as shown in Eq. (6.3).

$$\frac{2D}{dh^2}dt \leq 1 \quad (6.3)$$

Two types of boundary conditions may be applied to a diffusion model the Dirichlet and the Neumann boundary conditions.

1. Dirichlet boundary conditions are set when the state variable (concentration in this case) at this point is known and is a constant state condition.
2. Neumann boundary conditions are used when the gradient of the variable (the concentration flow in this case) is the value specified on the boundary. To calculate the Neumann conditions, artificial nodes are created, and with them, a gradient to an inner element is set to ensure a known flow is applied when computing the FTCS algorithm.

To evaluate a boundary condition, it is considered the flow on the boundary is f_b . To force this flow, the artificial node value is set as a function of an inner element. For example, to set a flow value between the nodes $(p, 2)$ and $(p, 0)$ from Fig. 6.6, the condition it would be Eq. (6.4).

$$C_{p,0} = C_{p,2} - 2dhf_b \quad (6.4)$$

The pseudocode of implementing the FTCS scheme is illustrated in Alg. 2 where C is the list of concentrations for each element, N , where each element contains the element number of the preceding and succeeding element, DB is a dictionary of the element number and the Dirichlet boundary value, NB is a dictionary of the element number and the Neumann boundary value, α is the diffusivity, dh the spatial discretization, dt the temporal discretization and t_{max} the maximum time to be simulated. The C++ code of the FTCS algorithm implemented in the GDL gas diffusion model is shown in Appendix D.2.1.

Algorithm 2 Pseudocode of FTCS algorithm implemented

Input variables

 $C, N, DB, NB, \alpha, dh, dt$ $t_i \leftarrow 0$ **while** $t_i < t_{max}$ **do**

Update Dirichlet boundary nodes

for n_i, v_i in DB **do** | $C[n_i] = v_i$ **end**

Update Neumann boundary nodes

for n_i, f_b in NB **do** | $C[N[n_i][0]] = C[N[n_i][1]] - 2f_b dh$ **end**

Iterate over all axis

for x_i **do**

| Iterate over all nodes

for n_i in N **do** | $C[n_i] = \alpha dt \frac{C[N[n_i][0]] - 2C[n_i] + C[N[n_i][0]]}{dh^2} + C[n_i]$ **end** **end** $t_i = t_i + dt$ **end**

6.4.4 Droplet re-absorption numerical implementation

The liquid water re-absorption from a droplet is a continuous process while the droplet is advancing. To represent the absorption smoothly, the temporal discretization of the movement and the calculations of the re-absorption must be small enough to avoid a false discrete result. If large temporal discretization is used, only the punctual absorptions would be observed since the droplet may advance multiple regions during the time step. In order to create a smooth path of absorption, the time step must be reduced to ensure the droplet advances less than a single region at every time step. The model becomes computationally expensive when reducing the time step. A new averaged trajectory strategy has been proposed to solve this problem and reduce the computational cost. It is considered a droplet with a given speed, v_d , in the flow field as represented in Fig. 6.7. During the time interval a) t_i to b) t_{i+1} the droplet has advanced from m to n elements of the linear-mesh, passing over all elements, h , between the flow field path from m

to n . Each element may have different normalized water content, s_m to s_n . The proposed method consists of calculating the average water in all the regions from m to n , $\bar{s}_{m \rightarrow n}$ and distributing the average water absorption rate to each individual element, $J_{a,h}$, according to their water content, s_h , Eq. (6.5), where $J_{m \rightarrow n}$ is the re-absorption flow calculated using the average water quantity in all the elements the droplet has moved over, $\bar{s}_{m \rightarrow n}$, Eq. (5.83).

$$J_{a,h} = \frac{s_h}{\bar{s}_{m \rightarrow n}} J_{m \rightarrow n} \quad (6.5)$$

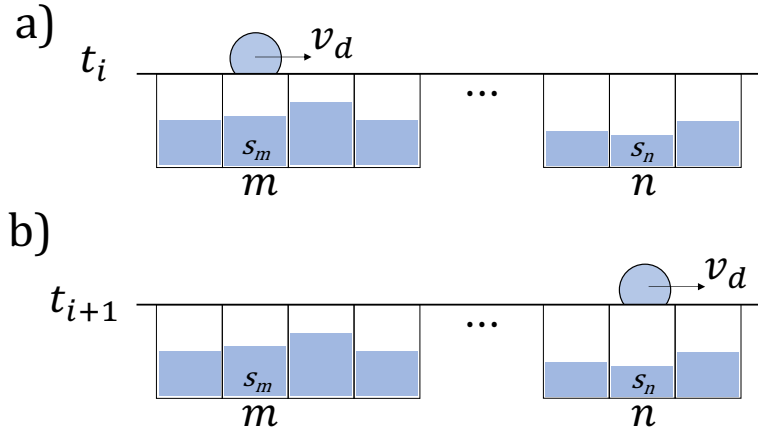


Figure 6.7: Droplet positions in a 1D channel at a) initial time and b) after a time step interval. The rectangles below the surface represent the amount of water in the GDL at each region

A smooth realistic pattern is obtained by applying the method proposed for water re-absorption. Accordingly, as a consequence of the total re-absorption flow, $J_{m \rightarrow n}$, the droplet volume is reduced during its advance. Re-absorption quantities are small compared with the droplet volumes. Therefore, for sufficiently small time intervals, it may be considered that the droplet volume is constant during each time iteration. This simplification is applied to enable updating droplet volume less frequently and reduce the computational effort of simulation.

6.4.5 Liquid water removal from the GDL

The pseudocode in Alg. 3 represents the algorithm used to calculate the drain of liquid water from GDL to the flow field. The algorithm uses a state variable called

drain to indicate if the region was draining on the previous time step, as there is a hysteresis between the start draining, p_{bt} , and the stop draining, p_{st} , by only observing the capillary pressure is not possible to calculate the draining flow.

Algorithm 3 Algorithm used to model the liquid water draining from the GDL to the flow field

```

drain ← 0
while simulating do                               /* during the simulation */
  if drain = 1 then                                 /* calculate drain */
    |  $S_{drain} = q_{drain}S$ 
  else
    |  $S_{drain} = 0$ 
  end
  if  $p_c > p_{bt}$  then                               /* start draining */
    | drain ← 1
  else if drain = 1 then                            /* when to stop draining */
    | if  $p_c < p_{st}$  then
    | | drain ← 0
end

```

6.5 Conclusions

This chapter presents the specific numerical implementation of the different sub-models and which type of discretization is used in each. The overall simulation methodology stages that allow the fast computation of the complete solver have been described and presented in a flow chart. Finally, the interface between the physical models have been explained, showing how the different elements are connected and which variables they exchange.

In the next chapter, chapter 7, the model presented in previous chapters 5-6 is validated with experimental data to corroborate the temporal and spatial response of the model using transient experiments to evaluate its dynamic response as well as stationary setups for the spatial current distribution.

The model is later used, in chapter 8, to perform studies by the massive simulation to evaluate the impact of different flow field geometry configurations, membrane and GDL thicknesses, and stoichiometry ratios. Those configurations are evaluated under temporal stability and spatial homogeneity in the plane xy .

7

Model experimental validation

Contents

7.1	Introduction	119
7.2	Temporal stability analysis	120
7.3	Experimental data and simulation	122
7.3.1	Different relative humidity conditions	123
7.3.2	Drying and humidification cycles	126
7.4	Model performance on validation setups	131
7.5	Conclusions	133

7.1 Introduction

In the modeling and simulation process of physical systems it is required the validation of models using experimental data. The objective of the validation procedure is fitting of the model's parameters to detect malfunctions.

The process is necessary to obtain accurate behavior of simulations with experimental data. In addition, it is particularly useful in the model design process as it provides feedback to understand the deficiencies that need to be corrected.

There are two stages in the validation procedure to perform before obtaining any simulation results: a) the stability and convergence of the results and b) the capacity

to represent the experimental data. This section shows how the two validation stages applied to the developed models have been performed.

The temporal stability is performed in the first stage of validation. The objective is to find the maximum stable time step in which results are consistent and accurate. The temporal stability analysis has been performed within the range of operation using stable conditions from real experimental data of the PEMFCs. The use of the maximum stable time step in the simulation has particular interest since it will allow longer simulated times with less computational time.

In the second validation stage, the model was adjusted and contrasted with experimental data. In this chapter, the details of each type of validation are explained.

7.2 Temporal stability analysis

The procedure of simulation consists of an iterative process for each time step. Each simulation iteration is the sequence of the submodel simulations, which are solved independently.

Due to the strategy implemented, the time step selected for each submodel has been small enough to have a stable and consistent behavior. Consequently, a proper analysis of the stability of the solver is performed.

In this section, the sensibility of the solver stability against the time step size is studied. This experimental setup uses a 25 cm² modeled cell with a single serpentine 1x1 mm² channel. The cell operates in galvanostatic mode at 0.7 A·cm⁻² and the gas streams are 1100 cm³·min⁻¹ of air at 21% of O₂ in the cathode, and 200 cm³·min⁻¹ at 100% of H₂ in the anode at 1.5 atm both channels.

In this validation procedure, the cell's steady state and transient performance are evaluated. The validation of the transient performance is analyzed using drying and humidification cycles. The RH cycle experiment used in the validation is a square function applied on the cathode from 100% to 50% with a duration of 250 s. The RH cycle is shown in Fig. 7.1.

To study the temporal stability, 0.5 s, 1 s, 2 s, and 5 s time step sizes are tested. This range of time steps has been chosen since lower values will make

the solver too slow to be practically usable. A larger time step will reduce the result accuracy of simulated time-dependent variables, such as the position of water droplets in the flow field channel.

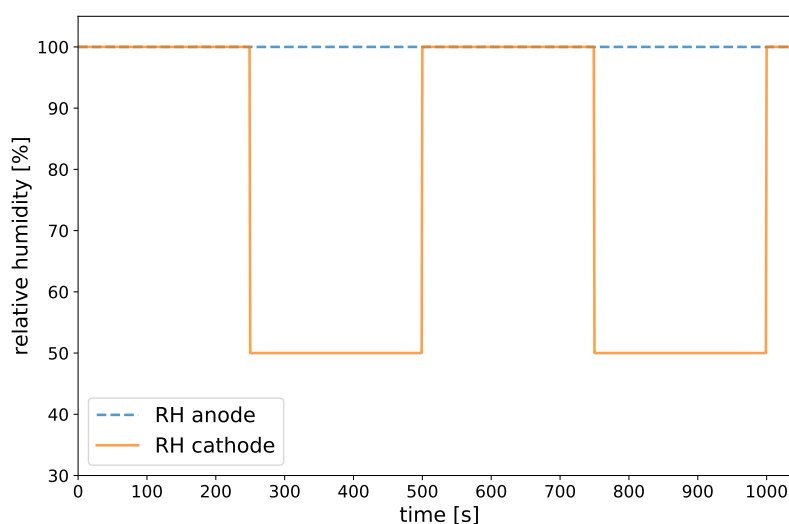


Figure 7.1: Humidification cycle used in validation procedure

The overall voltage of the cell comparing the effect of time step size in the simulation of the RH cycles experiment is shown in Fig. 7.2.

In Fig. 7.2-a, the transient voltages response are shown with no significant differences. But in Fig. 7.2-b, the differences between each time-step (1 s, 2 s, and 5 s) with respect to the 0.5 s time-step are plotted in absolute value, showing the error between them.

Despite representing the same transient phenomenon, the responses obtained show worse accuracy when the time step increases. Also, the convergence of results is achieved for time steps smaller than 1 s. Therefore, the 1 s time step has been chosen as the default time step since this balanced value allows stable and accurate simulations to be obtained with the minimum computational cost.

After analyzing the stability of simulations, it can be stated that the model is stable enough to perform validation with experimental data.

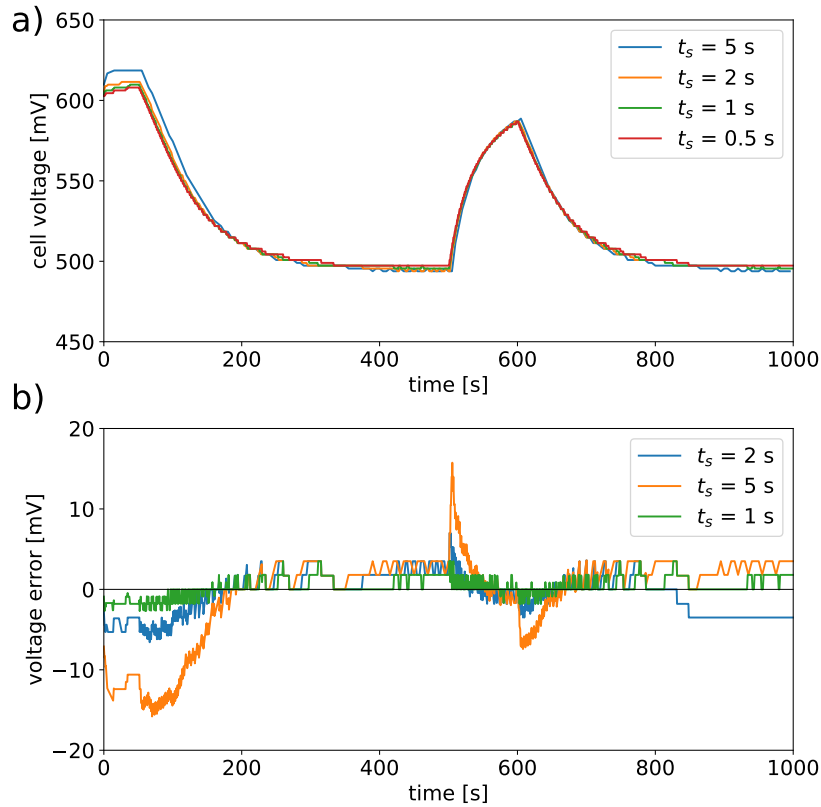


Figure 7.2: Effect of different time step sizes in the RH cycles simulation. a) Voltage response for 5, 2, 1, and 0.5 s and b) voltage error between each time step size response and the 0.5 s.

7.3 Experimental data and simulation

The experimental validation has been performed using two different experimental setups to evaluate both the spatial uniformity and the transient response of the cell.

Both experiments represent the dynamic behavior of the cell, where water management plays an important role, and the local current density values have been acquired by using segmented cells. The use of segmented cells is useful to be able to adequately represent the spatial performance of the cell in the model.

These features of the experiments are very appropriate for validating the models. The unknown parameters of the models have been fitted to obtain similar results to that obtained in the real experiments.

The two sets of experiments used for validating are:

1. Different relative humidity conditions. Based on the experimental data from [5], a cell with 23 parallel serpentine channels of $0.8 \times 0.8 \text{ mm}^2$ is studied. Different constant humidification values on the anode and cathode flow fields inlet are evaluated to investigate the spatial current density pattern on the 141 cm^2 cell.
2. Drying and humidification cycles. This validation has been performed using data from [4] data, where a cell with a single parallel serpentine channel of $1 \times 1 \text{ mm}^2$ has been studied in a 25 cm^2 cell. The cell operates in a potentiostatic mode, and low cathode humidification is set constant (RH 100% in the anode and 6% in the cathode). During this process, electrolyte drying occurs on the cell until $40 \mu\text{l}$ during 5 s of liquid water is inserted in the anode channel to humidify the cell. The liquid water is partially absorbed during this phase, humidifying the cell and increasing the water content, which changes the overall current density.

The model parameters have been fitted to accurately represent the behavior of the two experiments used to validate the model. The following subsections expose a detailed explanation of the validation experiments.

7.3.1 Different relative humidity conditions

In this subsection, the spatial performance of the cell using the experimental data from [5] and the simulation are compared. These experiments are focused on analyzing the effect of extreme operational conditions using different RH gas anode and cathode inlet setups. Those simulations use an $11.6 \times 11.6 \text{ cm}^2$ cell area of 23 parallel serpentine channels. The segmented cell (9x10 segments) was used to acquire the local current density. The cell flow field design is presented in Fig. 7.3.

The cell distribution has been replicated as shown in Fig. 7.3, and the reproduced configurations are shown in Tab. 7.1.

In [5], multiple experiments with different RH settings were performed. In this work is observed the impact on current density distribution due to RH variations.

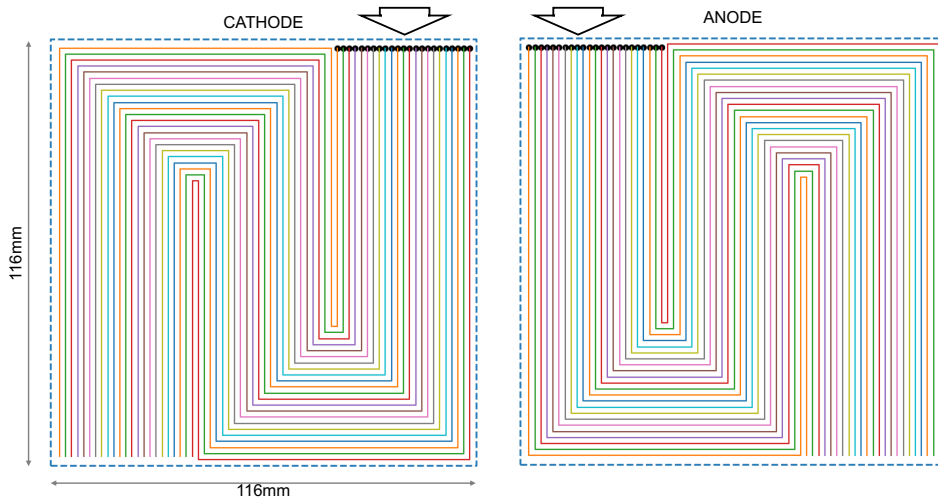


Figure 7.3: Parallel serpentine flow field, 23 channels, 0.8 mm channel width, 1 mm rib width, 3 loops. Segmented cell divided into 9x10 segments.

Parameter	Value
Cell temperature [°C]	80
Pressure [atm]	1.5
j [$\text{A}\cdot\text{cm}^{-2}$]	0.70
Anode flow rate [$\text{cm}^3\cdot\text{min}^{-1}$]	850
Cathode flow rate [$\text{cm}^3\cdot\text{min}^{-1}$]	3320
Anode H_2 [%]	100
Cathode O_2 [%]	21
Anode-cathode gas flow	Counterflow
# ch.	23
$\text{RH}_{c,a}$ [%]	100 - 6,100
θ_S [rad]	130
Membrane	Nafion XL
Gas Diffusion layer	Sigracet 25 BC

Table 7.1: Main parameters used on the simulation

To validate the model presented in this thesis, only four experiments presented in [5] have been selected. Three obtain stable solutions and one unstable, as shown on Tab. 7.2. The simulations are performed in galvanostatic mode, at $0.7 \text{ A}\cdot\text{cm}^{-2}$, which is stabilized around 0.635 V. These values vary slightly depending on the experiment due to the humidification level.

The results of the simulations compared with the experimental results are analyzed qualitatively in Fig. 7.4.

Test	HR _a	HR _c	Simulation stability
S.1	100	100	yes
S.2	50	50	yes
S.3	20	50	yes
S.4	50	20	no

Table 7.2: Stability of simulations with different RH in anode and cathode used in the model validation procedure

The simulated results show similar behaviors from the experimental data regarding average performance value and current density distribution. All simulations show a peak current density area in the center of the cell. This performance may be a consequence of the combined fuel concentrations (O₂ and H₂); this is later analyzed in Fig. 7.5). Simulation S.4 clearly shows how the instability, due to the lack of humidification, creates a high current density spot on the left side of the cell, similar to the performance observed empirically.

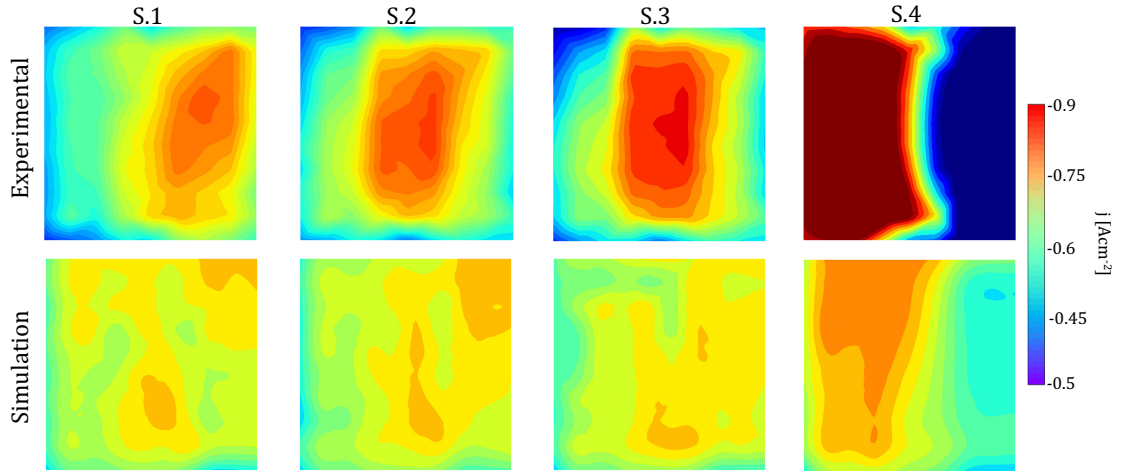


Figure 7.4: Spatial current density comparison of the experimental and simulation results for the RH in the setup shown in Tab. 7.2

Fig. 7.5 shows the simulated O₂, H₂ concentrations in the flow field of experimental data S.3. In this representation, it can be observed that the non-uniformity is mainly caused by the fuel concentration (shown in the figure) evolution.

Not only the spatial distribution of current density is important, but also the overall cell performance. Tab. 7.3 shows the average values of the cell stabilization being \bar{W}^s the normalized average water content in the cell, and \bar{v}_s and σ_v^s the

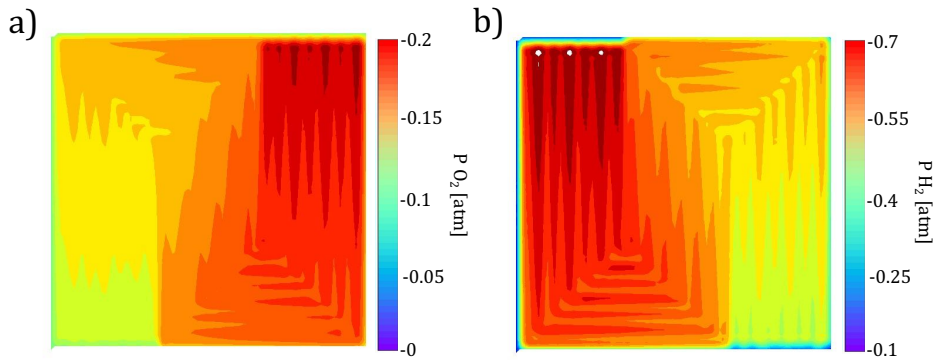


Figure 7.5: Simulated results of partial pressure of a) Oxygen in the cathode and b) Hydrogen in the anode of simulation S.3

voltage and its standard deviation respectively. The stabilization values match very well the experimental results.

Value	Simulation			Experimental	
	\bar{v}_s [mV]	σ_v^s [mV]	\bar{W}^s [-]	\bar{v}_s [mV]	σ_v^s [mV]
S.1	650	1.07	0.373	645	5.38
S.2	648	1.64	0.369	645	4.93
S.3	647	1.357	0.365	635	5.21
S.4	-	-	-	-	-

Table 7.3: Comparison of voltage stability in the experiments and the simulations used in model validation using different RH setups

7.3.2 Drying and humidification cycles

In this section, the dynamic performance of the cell has been validated by considering water humidification, drying, and liquid water re-absorption time cycles. For this purpose, data from [4] has been used to compare the results obtained with the model simulation. The experiments conducted in [4] showed an interesting dynamic behavior involving transitions within high-performance and lower-performance states due to the cell's humidification. In the experiments, the water content distribution in the cell is analyzed using neutron imaging. The overall current density and voltage values are compared in the validation analysis to ensure the cell performs at equivalent operating points. The cell's flow field used in the experiment and simulations is a $1 \times 1 \text{ mm}^2$ single serpentine $5 \times 5 \text{ cm}^2$ design as shown

in Fig. 7.6. The MEA border is drawn in a dashed blue line, and the center line of the channel is in a solid orange line.

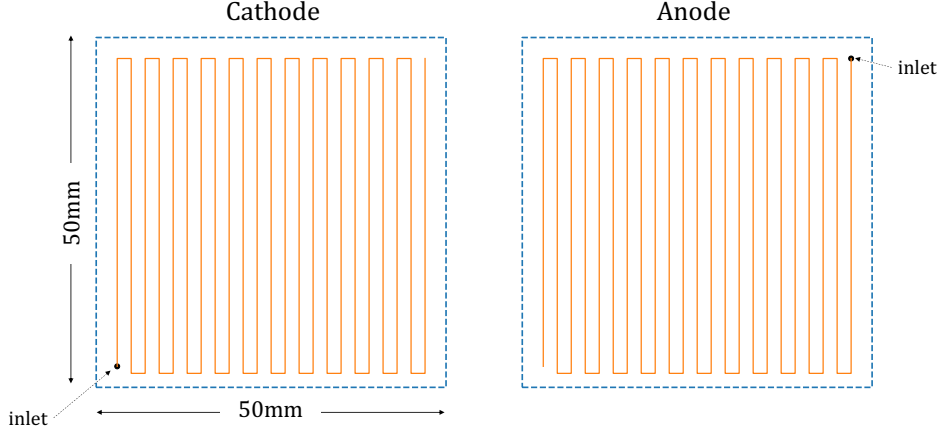


Figure 7.6: Flow field (single serpentine cell, $1 \times 1 \text{ mm}^2$ section) used in the validation of drying and re-humidification cycle experiment

The experiments start setting the cell into steady state operating mode. The experimental setup is obtained by feeding the cell with 100% RH gas in the cathode and anode. After 200 s, the RH gas cathode is dropped to 6% for 400 s, drying the cell. Passed the 400 s of drying conditions, $8 \mu\text{l}\cdot\text{s}^{-1}$ of liquid water is inserted during 5 s, a total of $40 \mu\text{l}$, in the anode flow field inlet as water droplets. Those conditions are maintained for 500 s until a new insertion of liquid water. The cycle then repeats. Fig. 7.7 illustrates the cycle previously described where on the left axis, the RH inlet levels for anode and cathode are represented, and in the right axis, the water liquid flow injected in the anode inlet.

The cell setup parameters are shown on Tab. 7.4, where dt is the temporal discretization time step, and dx is the MEA xy -mesh discretization, w_c and h_c are the width and height of the channel, $\#ch$, is the number of parallel channels, $\text{RH}_{c,a}$ the RH levels of the cathode and anode, and the θ_S the contact angle of GDL's surface.

The physical membrane parameters used in the simulation are obtained from the specification of Nafion XL [168]. Considering the membrane is $27.5 \mu\text{m}$ thick, the specific weight of $55 \text{ g}\cdot\text{cm}^{-2}$, and a conductivity is higher than $50.5 \text{ mS}\cdot\text{cm}^{-1}$ and $72.0 \text{ mS}\cdot\text{cm}^{-1}$, through plane and in-plane, respectively.

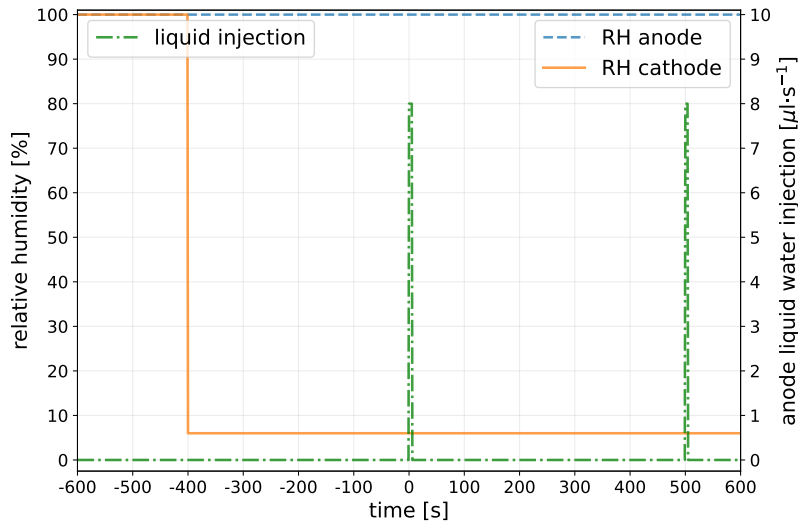


Figure 7.7: RH inlet levels and liquid water injection flow on the drying and humidification cycles simulation validation.

Parameter	Value
dt [s]	1
dx [mm]	0.2
w_c [mm]	1
h_c [mm]	1
#ch. [-]	25
RH_c [%]	100
RH_a [%]	100, 6
θ_S [deg]	130

Table 7.4: Parameters used on the experimental simulations where dt is the time step, dx the MEA XY spatial discretization, w_c the width of the channel, h_c the height of the channel, #ch. the number of channels, RH_x the cathode or anode humidity, θ_s the contact angle of the GDL.

The experimental and simulated results are first compared qualitatively. Fig. 7.8 shows a spatial comparison of the experimental and simulation results in terms of water content and current density.

The first column of the figure shows the water content in the cell from the experimental setup using neutron imaging [4]. The second column represents the total water content in the cell in-plane obtained from the simulation, and the third column is the simulated current density. The simulation results show a good fit both temporal to the experimental data both dynamically and spatially, regarding

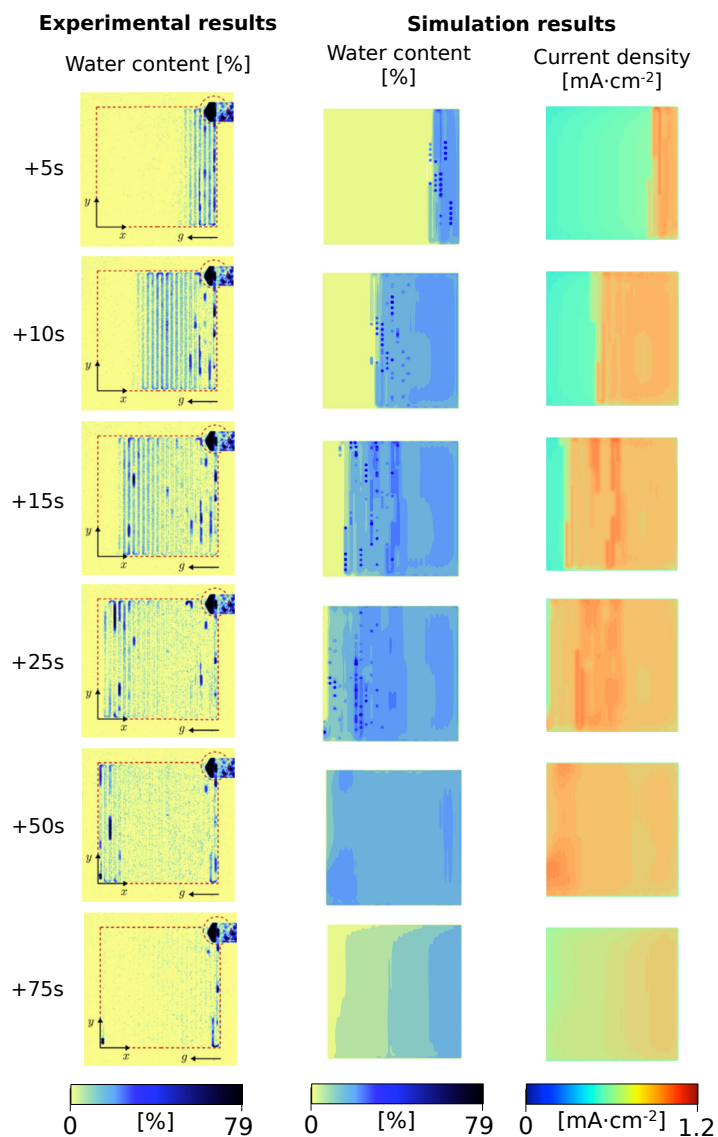


Figure 7.8: Spatial distribution of water content during droplet injection in experimental and simulation, and the spatial distribution of current density in the simulation

water in the cell and current density.

As the cell operates in potentiostatic mode, the dynamic response of the overall current density is compared between experimental and simulation in Fig. 7.9, between brackets the time after droplet insertion and the total time. The results show a good fit with the experimental data, both dynamically and spatially, regarding water in the cell and current density.

In simulation results, the liquid water injected into the anode channel is rapidly

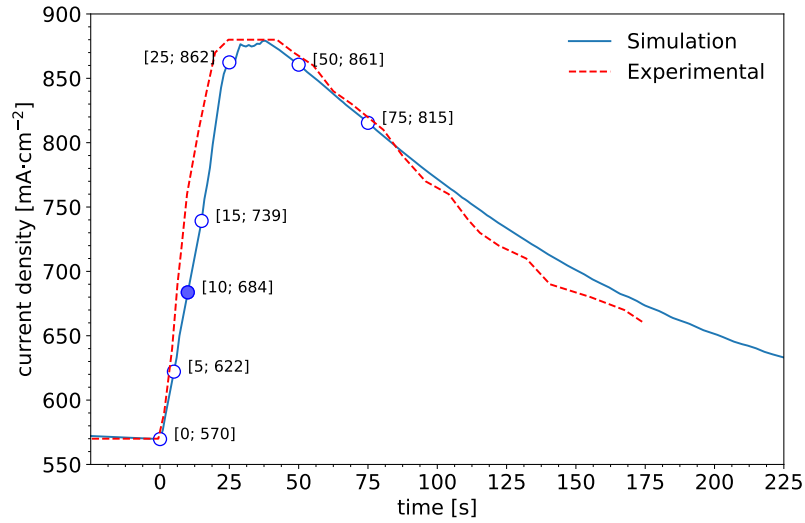


Figure 7.9: Comparison on average current density between data and simulation

absorbed due to the low presence of water on its GDL. The droplet liquid water is absorbed in steam form into the GDL. Direct liquid infiltration does not occur in high hydrophobic GDLs. The electro-osmotic drag keeps the anode dry enough to continue absorbing water and increasing the humidification of both sides. This phenomenon is observed in Fig. 7.10, where the cell's total amount of water is represented. Fig. 7.10-b presents the water transfer rates due to back diffusion and electro-osmotic drag and the total water transfer rate, calculated as the difference between back diffusion and electro-osmotic drag contribution. During the hydration phase (0-30 s), the water flow to the cathode GDL increases until the anode flow field droplets are removed from the cell since the back-diffusion compensates for the water content difference until the drying phase is reached again.

The RH in the anode is kept to 100% during all the simulations, and therefore no evaporation occurs. In the GDL, accumulated water due to the absorption of liquid water droplets is solely removed via diffusion to the cathode and evaporation on the cathode side. The portion of water, non-absorbed in steam phase into the GDL, remanent in the droplets still in liquid form, is removed as a consequence of the gas flow in the channels.

The model is discretized through the xy -plane, which allows to observe the distribution of water content in the cell's components. In Fig. 7.11-a the water

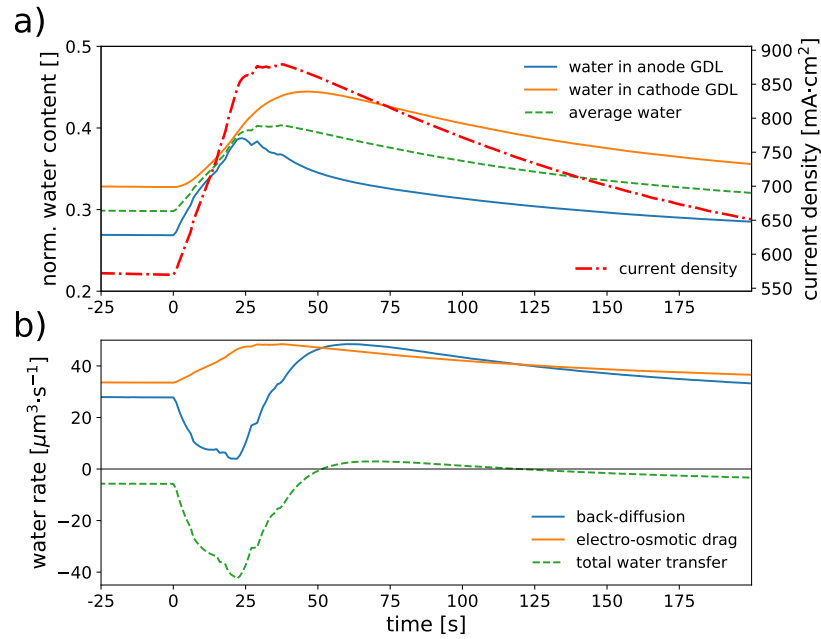


Figure 7.10: Dynamic performance of a) amount of water in each side of the cell with the current density, and b) different water transfer rate contribution and the total water transfer rate

content in the time instant 10 s after the droplet insertion of the simulation experiment is shown in the three spatial axes. Fig. 7.11-a also shows a section with the average water content of the anode and cathode's GDL and flow fields.

Fig. 7.11-b shows a time delay between the highest water content value in the cathode GDL and the water content peak in the anode GDL. This phenomenon is a consequence of the water diffusion dynamics between the anode and cathode sides.

The results of the simulation show how the liquid water injected into the anode flow field is rapidly absorbed, in the steam phase, due to the low hydration level in the anode GDL. The electro-osmotic drag keeps the anode dry enough to continue absorbing water and increasing the hydration level of both sides.

7.4 Model performance on validation setups

The model validation has been performed with two different cell setups. A cell with 141 cm² membrane area, 23 parallel channels of 0.8x0.8 mm² cross-sectional operating at 0.7 A·cm⁻² in galvanostatic mode with 1.5 atm of air in the cathode and pure

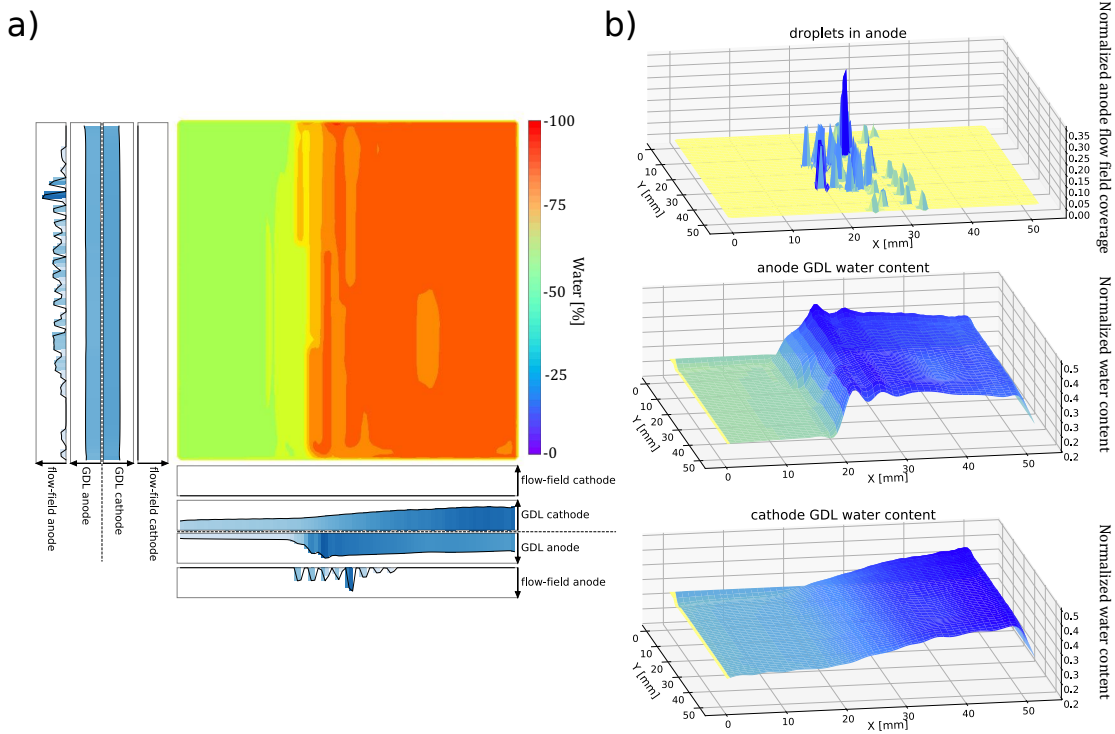


Figure 7.11: Simulation results at experiment time 10 s after droplet injection (blue marker on Fig.7.9) a) Water content in the cell in the three spatial axes, b) in-plane water content distribution in the anode flow field, and in the anode and cathode GDLs.

hydrogen in the anode operating at 80°C . The cell used Nafion XL as membrane and Sigracet 25 BC as GDLs and another cell with 25 cm^2 membrane size, with $1\times 1\text{ mm}^2$ section area of the single serpentine flow field. The first cell operates in a steady state regime, and the second dynamically in drying-humidifying cycles. A third cell with a 100 cm^2 with 11 parallel channels of $1\times 1\text{ mm}^2$ cross-sectional area with constant RH has also been used to evaluate the computational performance of the model.

Despite of the experiments performed in each active area are different, the objective is to evaluate the range of computational time of each submodel with respect to the cell configuration.

The spatial discretization in these cells' configurations differs in order to have an integer number of elements in each channel. Consequently, the total number of elements per cell is 23406 (for the 25 cm^2 cell), 162796 (for the 100 cm^2 cell), and 264192 (for the 141 cm^2 cell) in the plane xy .

The model has been executed in a 6 core Intel® Xeon® processor E5-2620 v3, with 64Gb of RAM and SSD under Windows10. The python code and the C++ program run in single-core mode. The different working points (drying or steady state) produce different amount of droplets to be removed, which may impact the simulation time. In a similar manner, solving for constant-current instead of constant-voltage mode increases the simulation time of the electro-chemical part as it has to be solved iteratively.

Tab. 7.5 shows the execution time of a 1 s simulation time step for the different configurations. This time is not constant and may fluctuate slightly during the simulation. On those simulations, on average, each time step lasted 4.16 s, 23.57 s, 35.37 s for the 25 cm², 100 cm², and 141 cm² cells, respectively. Therefore for a simulated time of 100 s, the execution lasts 7 min (410 s), 39 min (2357 s), and 58 min (3490 s); for a 1000 s of simulated time the execution time takes up to 68 min (4100 s), 392 min (23570 s) and 581 min (34900 s) respectively.

As it can be observed, the most costly part is the channel section where the droplets movement is calculated. The gases and water diffusion, the PEMFC calculations, and the water balance between the anode and cathode are computed fast as they are implemented in C++. Moreover, it can be observed that there are two types of models, a) the ones that the simulation time increases with the number of elements such as GDL diffusion, water, and membrane balance, and b) the ones that are independent of the cell dimension and may depend on the channel length, such as the channel solver.

7.5 Conclusions

In this chapter, the physical representation of the phenomena described in the model has been validated with experimental data. Also, the stability of the simulations has been analyzed.

To validate the stability of the simulation, a drying/re-humidification cycle has been tested as it can provide a dynamic behavior representation of the cell. Different time step values have been tested, and the cell voltage response has been

	25 cm ²	100 cm ²	141 cm ²
Update parameters	0.04	0.06	0.06
Channel solver	0.98	7.53	14.19
Water balance	0.26	2.28	4.12
GDL gas diffusion	0.05	0.7	0.6
GDL water diffusion	0.35	0.5	0.5
Electrochemical reactions	0.05	1.4	1.8
Membrane water balance	0.5	2.4	5.9
Save data	1.93	8.7	8.2
Total	4.16 s	23.57 s	35.37 s

Table 7.5: Computation time to simulate of one time step (1 s) for 25 cm², 100 cm² and 141 cm² cell surface.

analyzed. It has been shown that for time steps below 1 s, the model is stable and has a small transient behavior error.

The validation of the model was performed with two sets of experimental data. The steady-state performance of the model has been validated by the spatial current density distribution under different humidification configurations using a 23-channel segmented cell (subsection 7.3.1). The dynamic response of the drying/re-humidification cycle experiment in a single serpentine cell has been validated using neutron imaging (subsection 7.3.2).

The next chapter shows that the model is used to conduct a detailed analysis of the effect of various cell design and operational parameters on the spatial and temporal uniformity of the cell's performance.

8

Analysis of simulation results

Contents

8.1	Introduction	135
8.2	Experimental investigation	136
8.3	Uniformity general study (Exp₁)	140
8.4	Serpentine and parallel channel design (Exp₂)	148
8.5	GDL thickness (Exp₃)	149
8.6	Membrane thickness (Exp₄)	153
8.7	Temperature (Exp₅)	156
8.8	Co-flow and counter-flow (Exp₆)	159
8.9	Conclusions	160

8.1 Introduction

Previous chapters described the different equations driving the solver presented, chapter 5, how those models are interconnected and implemented in order to obtain a fast and reliable pseudo-3D model, chapter 6, and chapter 7 presented the model validation using two sets of experimental data, one with a 5x5 mm² cell with liquid water injection in the anode to produce humidification cycles using neutron-imaging to measure the water distribution. Another experiment uses an 11.6x11.6 mm² cell with different RH conditions to observe the current density distribution using the segmented cell method.

This chapter performs a set of simulation experiments to evaluate the performance of different cell configurations. These experiments intend to provide insights into how operational and design parameters impact the cell's temporal stability and spatial homogeneity to influence future fuel cell designs. The parameters evaluated are the flow field configuration (serpentine and parallel), channel/rib ratio, stoichiometric ratio, GDL thickness, membrane thickness, cell temperature, and co-flow and counter-flow effect. This study is applied in a cell with a $10 \times 10 \text{ cm}^2$ active surface.

8.2 Experimental investigation

In the previous section 7.1, the presented model has been validated with two different cell configurations. The computational performance has also been evaluated and optimized, allowing for achieving intensive model simulation using short simulation times. This optimization of the simulation time is necessary to conduct the systematic experimentation of the proposed parameters performed in this thesis since the number of simulations completed is considerable.

The model developed is used to study the impact of different cell configurations in terms of performance spatial homogeneity and temporal stability since these characteristics are related directly to cell durability (section 2.1). Cell performance uniformity evaluates the homogeneity of current density in the MEA plane (xy) in steady state.

It has been studied that cells that exhibit spatial non-uniform performance behavior suffer from uneven aging of the MEA component [74]. The temporal stability of the cell is evaluated by analyzing the dynamic voltage transitions of the overall performance under constant current demand. An unstable voltage of a cell shows changes dynamically in the performance, which accelerates its degradation [169].

Different cell configurations have been simulated to study various parameters' contributions to the cell spatial homogeneity and temporal stability on a cell of

around 10x10 cm². In the following list, an overview of the multiple experiment configurations is described:

1. Uniformity general study (Exp₁). In this general study, three parameters are studied simultaneously, a) the ratio channel/rib, b) the stoichiometry ratio, and c) the number of parallel serpentine channels. Those parameters are variations from the stable known cell condition configuration extracted from [5].
2. Serpentine and straight parallel channels (Exp₂). Previous studies have been performed with serpentine configurations. Exp₂ studies the performance of a 10x10 cm² cell area using parallel straight channels. Multiple stoichiometry ratio values are also analyzed to find the better stable performance setup of the cell.
3. GDL thickness (Exp₃). Using the setup of the most uniform performance obtained in the experiment set (Exp₁), s1.27, the effect of different values of GDL thicknesses in the temporal stability and spatial uniformity have been evaluated.
4. Membrane thickness (Exp₄). With the configuration s1.27 from the general study, multiple membrane thicknesses have been tested.
5. Temperature (Exp₅). Using setup s1.27, different operating temperatures have been tested to understand the impact of the cell temperature on the overall performance of the device.
6. Co-flow and counter-flow (Exp₆). With the setup s1.27 from the general study, a comparison of results using it in co-flow or counter-flow has been performed to observe how the spatial distribution of the current density profile evolves.

The simulations have been analyzed with respect to the a) spatial analysis evaluating the average and the standard deviation of the current density distribution

and b) the temporal analysis evaluating the average and standard deviation of different variables along the 250 s - 1000 s time range.

The spatial homogeneity, using the variable x as a reference, its average is calculated at the time step t , $\overline{x_t^h}$, using Eq. (8.1), and its standard deviation, $\sigma_{x,t}^h$ by using Eq. (8.2). Where m is the number of points of the xy -plane and $x_{t,i}$ the value of x at the i^{th} point at t time step. The values obtained depend on the spatial discretization size; in this case, a 1 mm on both axis. Therefore, typically a cell will contain 10000 measurement elements, m .

$$\overline{x_t^h} = \frac{1}{m} \sum_{i=1}^{i=m} x_{t,i} \quad (8.1)$$

$$\sigma_{x,t}^h = \sqrt{\frac{1}{m-1} \sum_{i=1}^{i=m} (x_i - \overline{x_t^h})^2} \quad (8.2)$$

To avoid any punctual numerical errors, the data used in the analysis of the spatial behavior disregards the lower and higher 5% of the spatial analyzed values, Eq. 8.3.

$$x^* = \{x_i, \forall x_i \in (p_{5\%}, p_{95\%})\} \quad (8.3)$$

Despite the spatial SD deviation being a proper variable to compare similar cells' performance where slight differences want to be observed, using the range, $R_{x,t}^h$, Eq. (8.5), performs better to distinguish between cells operating at very different homogeneity values.

$$x_{min}^*, x_{max}^* = \{x_i, \forall x_i \in (p_{5\%}, p_{10\%})\}, \{x_i, \forall x_i \in (p_{90\%}, p_{95\%})\} \quad (8.4)$$

$$R_{x,t}^h = |\overline{x_{max}^*} - \overline{x_{min}^*}| \quad (8.5)$$

The range, in this case, is calculated from the spatial analyzed values, averaging a window of the lower and higher values. In this case study, the window is 5%; with

those averages, the range from them is calculated, Eq. (8.4) being x_{min}^* and x_{max}^* a list of values of the 5% lower and higher values and therefore \bar{x}_{min}^* and \bar{x}_{max}^* their averages. By doing that, the range is not represented by the maximum and minimum values, which could be caused by a sudden drop produced in this time step, but by a range of values. This procedure helps identify spatial non-uniformity more robustly.

To analyze the cell stability in the temporal axis considering a variable x its the average, \bar{x}^s , is calculated using Eq. (8.6), and the standard deviation (SD), σ_x^s is calculated using Eq. (8.7) during the experiment time, T . The simulations have been temporally discretized with a time step of 1 s.

$$\bar{x}^s = \frac{1}{T} \sum_{t=1}^{t=T} x_t^h \quad (8.6)$$

$$\sigma_x^s = \sqrt{\frac{1}{T-1} \sum_{t=1}^{t=T} (x_t^h - \bar{x}^s)^2} \quad (8.7)$$

Using the previous definitions, the parameters evaluated in the uniformity analysis of the cell are listed in Tab. 8.1.

The total surface area of the cell used in the simulations has approximately 100 cm². This value has been chosen to enable the use of multiple channel configurations while simulating a cell smaller than the 141 cm² used for validation to reduce the simulation time.

All the simulations are performed at constant current demand (0.7 A·cm⁻²) during 1000 s (except the unstable, approximately 16 min), which is considered enough time to reach a steady state and evaluate non-homogeneities or cell stability for constant current demand. The range analyzed for temporal stability is within 250 s - 1000 s to reduce transient stabilization effects. The current density chosen is set to obtain approximately 0.65 V to operate around the maximum power point. The cell operates at a temperature of 80° C. The inlet gas pressure is set to 1.5 atm both in the cathode and anode.

Symbol	definition	variable
\bar{j}^h	average current density	spatial
σ_j^h	current density variability	spatial
R_{jt}^h	current density range	spatial
\bar{v}^s	average voltage	temporal
σ_v^s	voltage variability	temporal
R_v^s	voltage range	temporal
\bar{p}_t^s	average power density	temporal
σ_p^s	power density variability	temporal
\bar{r}_e^s	average evaporation rate	temporal
σ_{re}^s	evaporation rate variability	temporal
\bar{r}_w^s	average liquid water removal rate	temporal
σ_{rw}^s	liquid water removal rate variability	temporal
\bar{W}^s	average normalized water content in cathode or anode	temporal
σ_W^s	normalized water content in cathode or anode variability	temporal
\bar{P}^s	average pressure drop	temporal
σ_P^s	pressure drop variability	temporal
\bar{u}_g^s	average gas speed	temporal

Table 8.1: Stability and homogeneity parameters table

The simulations are performed at constant gas humidity in the inlet of the flow field. The RH 50% is used as standard humidification since the cell becomes stable in conditions over 40% [148].

The membrane parameters used are the same that in the validation stage, NafionXL [168], with the same polarization equation parameters. The GDL physical parameters used are the Sigracet 25 BC commercial GDL. The component's thickness and properties are considered homogeneous and isotropic in all the simulations.

Cathode and anode gas flows are set to be counter flow. In the figures in this thesis, the gas cathode inlet is on the bottom left, and the anode inlet is on the top right.

8.3 Uniformity general study (Exp₁)

Multiple parallel serpentine flow field designs reduce the gas speed compared with a single serpentine inside the channel, resulting in a lower pressure drop, which may affect the water removal capacity.

Moreover, the aim to uniform the fuel partial pressure within the cell is to obtain a more homogeneous performance and, therefore, reduce its aging. This study analyzes multiple cell configurations to understand how each parameter impacts the cell's performance uniformity. The configuration parameters varied during the study are:

1. Stoichiometric ratio. Using as basis values, known and stable stoichiometry values (for the anode $\lambda = 1.2$ and the cathode $\lambda = 2$). The stoichiometric ratio, R_{st} , is multiple to the previously defined stoichiometric values.
2. Ratio (w_c/w_r). Ratio between the channel width (w_c) and the rib width (w_r). This parameter is referred to as the ratio C-R.
3. Number of parallel serpentine channels. The simulations use different numbers of parallel channels in the flow field, varying between 5 and 11.

Tab. 8.2 shows the range of values for each parameter used in this study, R_{st} , #ch, and w_c/w_r .

Regarding the stoichiometry ratio, three multipliers have been chosen (1, 1.3, and 1.7) since it is considered that 1 is the minimum multiplier to ensure homogeneity and stable performance experimentally validated by experimentation in [5].

The number of parallel channels has been selected to have between 4 and 9 turns. A turn is the U shape in the serpentine channel, produced when changing the channel direction formed by two corners. With this range of turns to be studied, the number of channels range is 5 to 11.

Concerning the channel/rib ratio, multipliers have been chosen from the central point (1, where the channel and the rib have the same width) and a value 25% higher and lower, creating channels of 0.75, 1, or 1.25 mm width. The $w_c + w_r$ is constant to 2 mm. Therefore if a channel is 0.75 mm, the rib is 1.25 mm width. Channel height is not part of the design of experiments, and it is set to 1 mm.

Due to the different number of channels, the width of the cell may vary slightly to allow the flow field configuration to fit in. Fig. 8.1 shows the 4 configurations tested. The flow rate will be adjusted to compensate for the size variations of the cell as a consequence of the number of channels and keep a similar stoichiometry.

Parameter	Values
R_{st}	1, 1.3, 1.7
#ch.	5, 7, 9, 11
$w_t = w_c + w_r$	2
$ratio = w_c/w_r$	3/5, 1, 5/3

Table 8.2: Parameters and values used in Exp_1

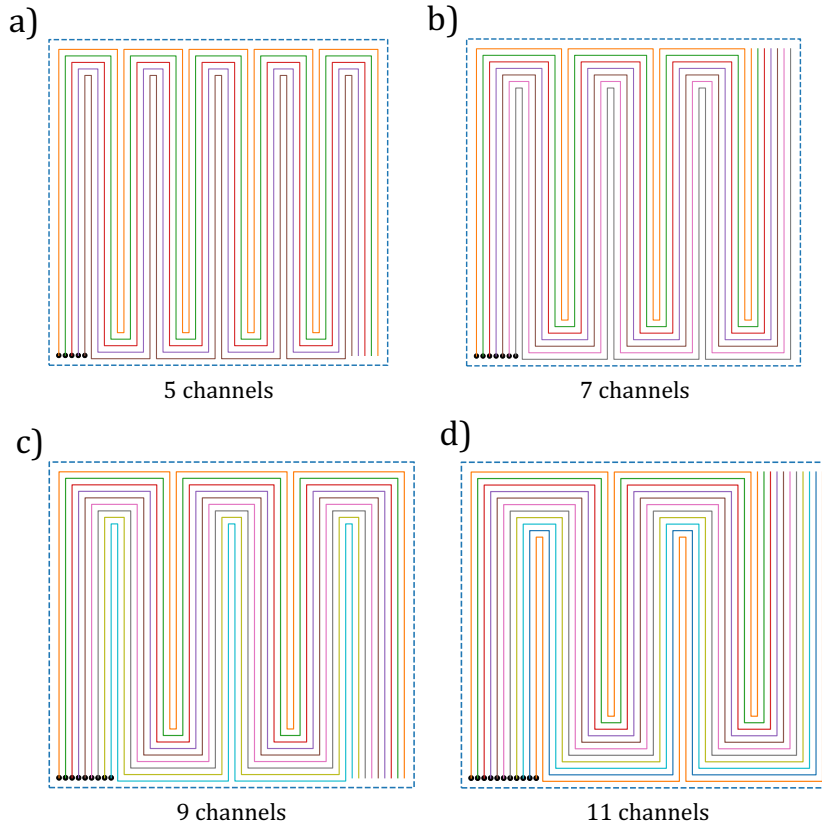


Figure 8.1: Representation of 4 parallel serpentine flow field designs used in the uniformity study. From left to right, number of parallel channels and MEA surface a) 5 channels, 10x10.4 cm, (s.4, s.8, s.12, s.16, s.20, s.24, s.28, s.32, s.36) b) 7 channels, 10x10.2 cm (s.3, s.7, s.11, s.15, s.19, s.23, s.27, s.31, s.35), c) 9 channels, 10x11.2 cm (s.2, s.6, s.10, s.14, s.18, s.22, s.26, s.30, s.34), and d) 11 channels, 10x11.4 cm (s.1, s.5, s.9, s.13, s.17, s.21, s.25, s.29, s.33).

All the possible parameter combinations from Tab. 8.2 produce a total experimental data set of 36 simulations numbered s1.1 to s1.36. The simulations were executed in the order they were numbered since the results are not dependent on the simulated order.

The study in Exp_1 is focused on finding the most suitable configurations with minor temporal instability and spatial in-homogeneity while reducing fuel consumption.

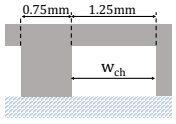
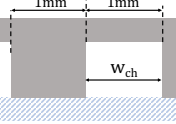
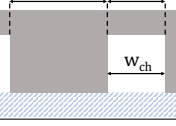
	ID #	w_c/w_r	# channels	R_{st}
	s1.1-s1.4	5/3	11,9,7,5	1.0
	s1.5-s1.8	5/3	11,9,7,5	1.3
	s1.9-s1.12	5/3	11,9,7,5	1.7
	s1.13-s1.16	1	11,9,7,5	1.0
	s1.17-s1.20	1	11,9,7,5	1.3
	s1.21-s1.24	1	11,9,7,5	1.7
	s1.25-s1.28	3/5	11,9,7,5	1.0
	s1.29-s1.32	3/5	11,9,7,5	1.3
	s1.33-s1.36	3/5	11,9,7,5	1.7

Table 8.3: Design table of simulated experiment varying parameters: channel-rib width ratio, w_c/w_r , number of channels in the flow field, # parallel channels, and stoichiometry ratio, R_{st} .

The analysis of the results shows that the cell reaches a flooding state in simulations s.1, s.2, s.3, and s.5 since the channels are clogged with liquid water. Configurations s.1, s.2, s.3, and s.5 use wider channels and lower stoichiometry ratio configuration, which causes lower gas speeds inside the flow field. Low gas speed reduces the capability of removing water droplets from the channel [170], which produces flooding in the channels. The flooding effect in the flow field produces computational instability in the simulation, causing simulation interruption in several cases. These simulations have been omitted from the study.

On the other hand, the simulation experiment s1.6, despite being stable, performs at levels far from the other simulations. Therefore s1.6 has also been removed from the study.

The other simulations from Exp₁ obtain stable results. Fig. 8.2-a shows the results of voltage SD, Fig. 8.2-b shows the spatial current density range in the plane xy , Fig. 8.2-c shows the variation of power density between all the different configurations with respect to the cathode gas speed. The results from Fig. 8.2-c show that the power density variation among them is slight; therefore, the simulations compare equivalent performing cells. Fig. 8.2-a shows a relationship between the temporal stability represented by the temporal voltage variability, σ_v^s ,

and the cathode gas speed, $\bar{u}_{c,g}^s$, showing an increase on stability with the cathode gas speed. The crosses and the arrows represent the simulations with values out of range or computationally unstable. The cell setup with a higher number of parallel channels and a smaller stoichiometry ratio produces lower gas speed through the channels, reducing the cell's capability to remove liquid water from the flow field.

Also, higher gas flow speed increases the evaporation rate since the capacity of steam absorption is higher. The combination of both phenomena produces a more temporal stable cell. Still, also, higher gas speeds may cause non-homogeneity along the cell, as is analyzed in the spatial performance section.

Unstable temporal performance on steady-state conditions is relevant since the MEA suffers local transitions from low to high-performance states, increasing the degradation. The temporal analysis shows that using higher gas speed obtains more stable cell performance.

Fig. 8.2-b shows the relationship of the spatial current density SD, σ_j^h , with respect to the cathode gas speed $\bar{u}_{c,g}^s$. The figure shows that the simulation setups with higher gas speeds obtain higher spatial in-homogeneity performance.

The impact on the voltage SD, σ_v^s , concerning the number of channels, the w_c/w_r relation, ratio C-R, and the stoichiometry is illustrated in Fig. 8.3. The temporal stability of the cell's performance becomes more stable from the data obtained when the values of the stoichiometry ratio increase. These results show the consequence of the increasing gas speed in the channels, which eases the liquid water removal from the flow field. Moreover, it can also be observed, especially on low stoichiometry ratios, that the lower the ratio C-R the more stable the performances. This result is similar when reducing the number of parallel channels composing the flow field.

Fig. 8.4 shows the values of current density SD related to the ratio C-R and the number of channels grouped by stoichiometry. The grey bars represent the unstable computational simulations; therefore, these results are not used for analysis. The results show the effect of narrower channels, in which the 3/5 ratio performs better in spatial homogeneity than the 5/3 and 1 ratio C-R setup.

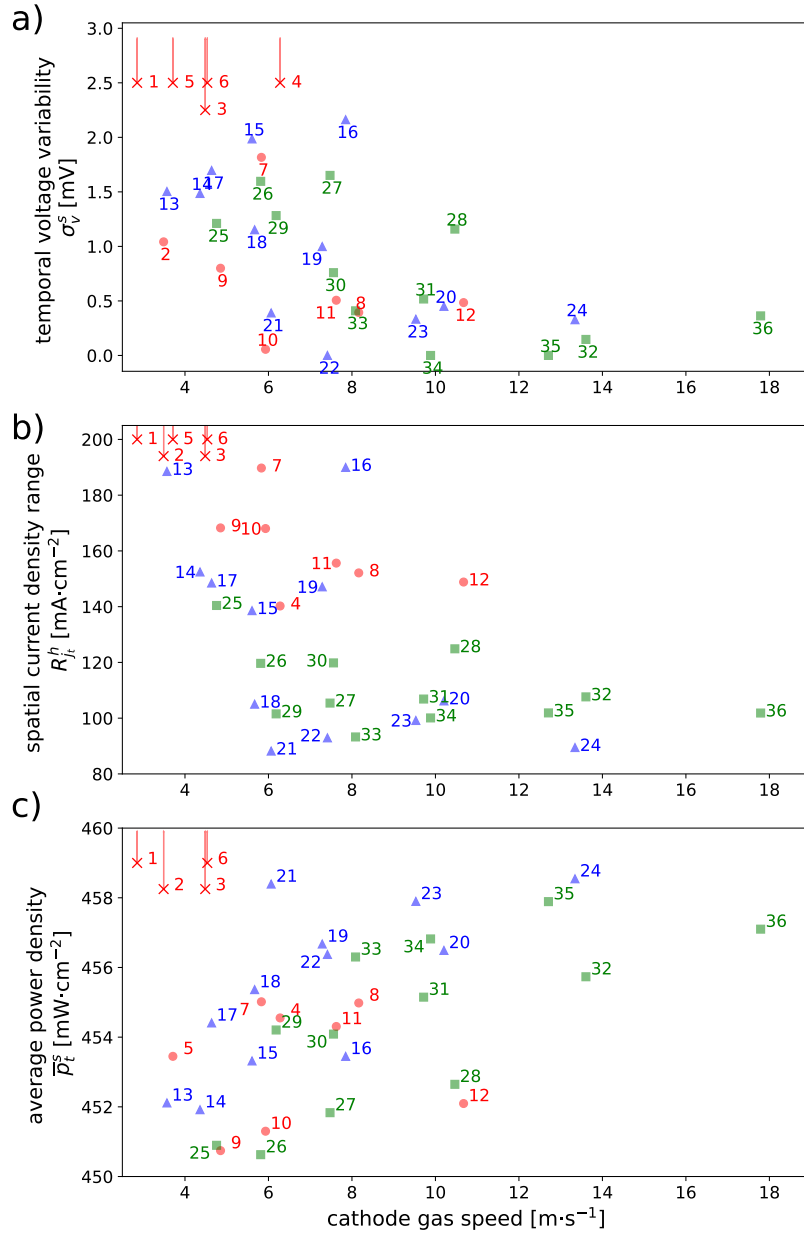


Figure 8.2: Relationship of a) voltage SD, σ_v^s , b) spatial current density SD, $\sigma_{j_t}^h$, and c) average power density, \bar{p}_i^s , of the different simulation setups with the cathode nominal gas speed

The time evolution of RH, the gas's partial pressure from inlet-outlet, and the presence of liquid droplets in the flow field influence spatial homogeneity. Therefore, higher flows increase the spatial homogeneity, reducing $\sigma_{j_t}^h$. However, the spatial homogeneity does not always improve when increasing the stoichiometry ratio using a lower number of channels or ratio C-R, as shown in Fig. 8.4. Nevertheless, increasing

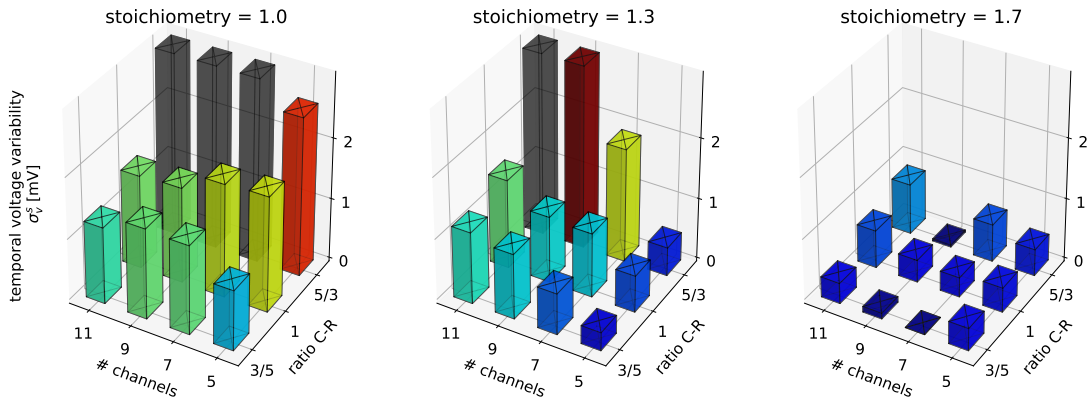


Figure 8.3: Voltage SD related to the number of channels, ratio C-R, and stoichiometry ratio

the stoichiometry ratio improves the cell performance homogeneity, especially on high C-R ratios and numbers of channels. An experimental setup with low stoichiometry ratios is more efficient in terms of fuel consumption. In the range of configurations simulated, the designs with 7 channels perform better than the rest in terms of spatial and temporal uniformity, especially when low stoichiometry ratios are used.

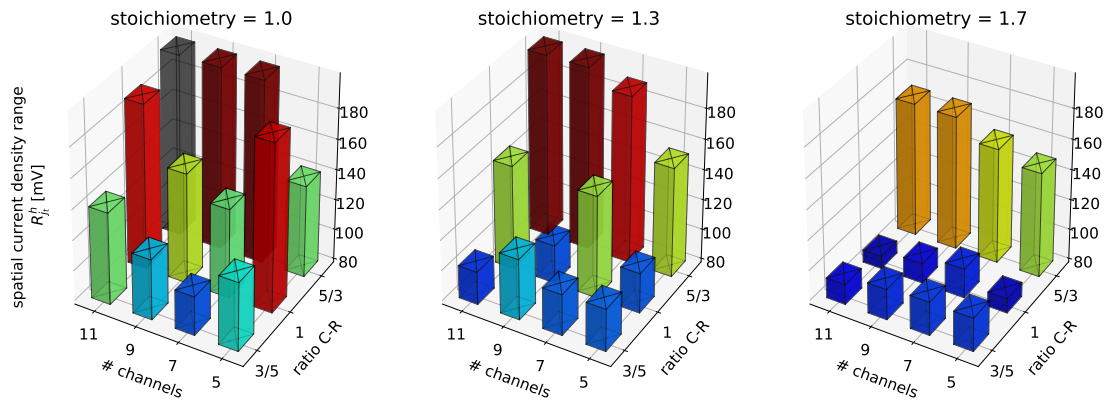


Figure 8.4: Spatial current density SD at the time 500 s related to the number of parallel channels, the ratio C-R, and the stoichiometry ratio.

Due to the gas flow field geometry with parallel serpentine channels design, the RH of the gas increases along the channels, from inlet to outlet, creating a pattern on the cell. As the number of channels is reduced, the length of each channel and the number of turns increases. When using a high number of parallel channels, the channel has similar segment lengths in vertical and horizontal directions (see

Fig. 8.1). But, a cell with a low number of parallel channels has most of the segments of the channel in the vertical direction. Fig. 8.5 shows a comparison of a specific channel in a 3-channel (not considered in the experimentation) compared to a channel of 11-channel parallel serpentine designs.

Therefore, when a lower number of parallel channels is used, in Fig. 8.1 from left-to-right gas direction (inlet to outlet), a non-uniformity effect on RH is observed in the design presented.

Furthermore, a lower number of parallel channels design produces longer channel paths for the same fuel cell size, increasing the distance a liquid water droplet must travel to be expelled.

From the results presented, a balance between the number of parallel channels (7 or 9 in the simulated range) is essential to ensure a proper spatial homogeneity of cell performance.

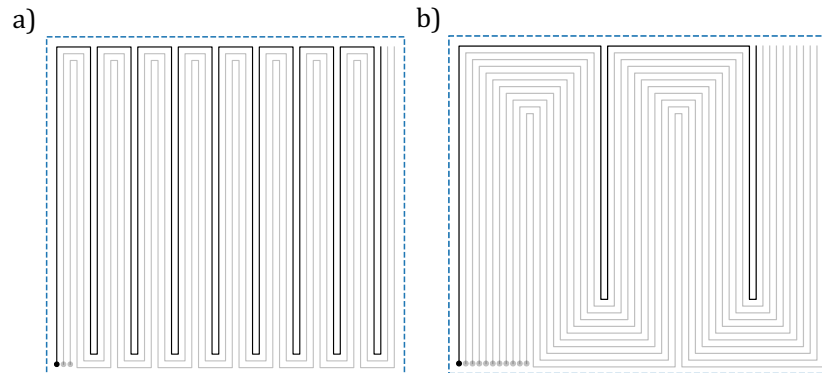


Figure 8.5: Comparison of a) a low number and b) a high number parallel channel in serpentine design for approximately the same cell size

Fig. 8.6 shows the spatial current density and water content for two different simulations setup; s1.35 uses 7 parallel channels, a ratio C-R $3/5$, and a stoichiometry ratio of 1. This simulation setup is compared with simulation s1.11, which uses 7 channels, a ratio of C-R $5/3$, and a stoichiometry ratio of 1.7. In the figure, visual differences in spatial homogeneity performance can be observed.

From the simulations, in terms of outlet pressure in the cathode or the anode, no distinctive trends are observed in the temporal analysis.

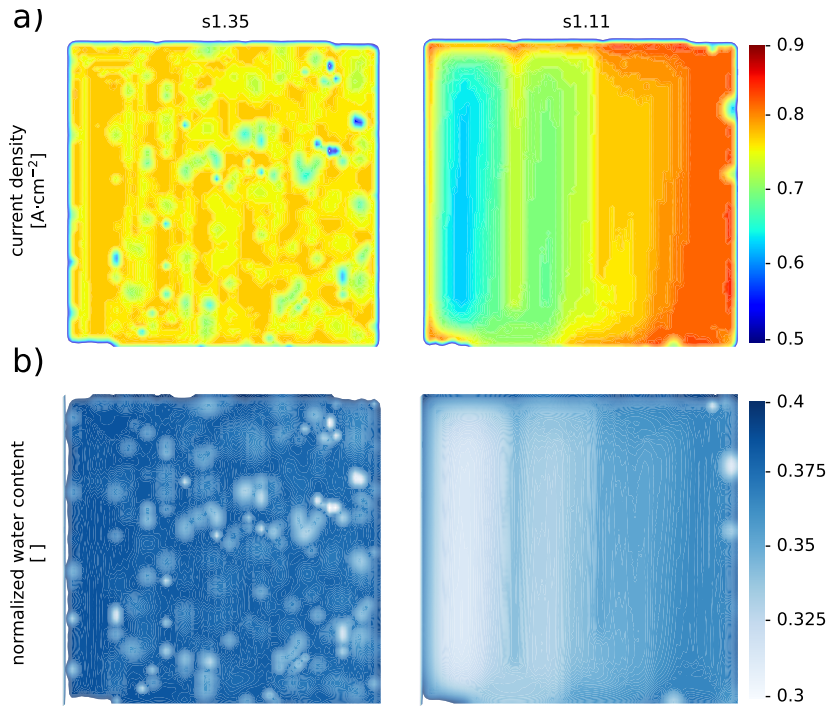


Figure 8.6: Spatial current density and water content comparison between simulation s.11 and s.35 at the time step 500 s. Seven parallel serpentine channels and 1.7 cathode stoichiometry are used in both configurations. The C-R width ratio is 5/3 for s.11 and 3/5 for s.35

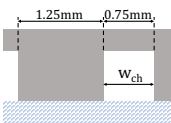
8.4 Serpentine and parallel channel design (*Exp₂*)

Parallel straight channels design is analyzed in this section compared with parallel serpentine channel design. One of the advantages of a straight channels design is that it has a linear liquid droplet removal path, which eases this process. The straight channel flow field design intends to avoid drops cluttering on each channel turn.

A cell of 10x10 cm² area and 0.75 mm channel width has been designed to simulate the parallel straight channels configuration. The configuration simulated has 48 parallel channels. The effect in the performance for four different gas flow values has been evaluated, Tab. 8.4.

It is observed that there is an agreement between the simulation results obtained from the parallel and the serpentine parallel channels designs. The effect of gas speed inside the channel is a critical factor in the uniformity performance of the cell since this experimental parameter has an essential impact on the homogeneity

and stability of the cell to remove liquid water. Higher stoichiometry ratios are required compared to the parallel serpentine design to remove the liquid water from the flow field. Despite having much shorter channels (10 cm long compared to the 7-channel design, which has an average channel length of 67.5 cm), the reduction of gas flow is relevant enough to prevent liquid water from being removed. The system energy efficiency is reduced with the experimental configuration of the straight parallel channel employed since it would require a fuel recovery system to make the solution economically feasible.



	ID #	w_c/w_r	# ch.	R_{st}
	s2.1	3/5	48	1
	s2.2	3/5	48	2
	s2.3	3/5	48	2.5
	s2.4	3/5	48	3

Table 8.4: Parameters used in the simulations of parallel straight channels design, Exp₂

Fig. 8.7 shows a) the spatial current density and b) the average water content on the cell using a stoichiometry ratio of 3. The figure shows a spatial current density gradient from the bottom to the top. However, the gas flow is set to counter-flow. This effect is due to the increase in RH along the cathode channel and liquid droplets, most commonly located at the gas outlet of the cathode. The fuel consumption is not limiting the performance of this cell since the gas concentration is three times higher than the stoichiometry used in the parallel serpentine channels design. Only the result of Fig. 8.7 is shown because the other configurations of the Exp₂ did not reach stable solutions due to water excess in the cell.

8.5 GDL thickness (Exp₃)

GDL thickness is a crucial design parameter in the PEMFC. The general criteria intend to keep the minimum thickness necessary to have a water reservoir and allow gases to flow under the rib while easing the liquid water removal. Increasing the GDL thickness allows the gases to faster reach below the ribs. But the liquid and steam water removal will become more difficult due to the longest z path. As

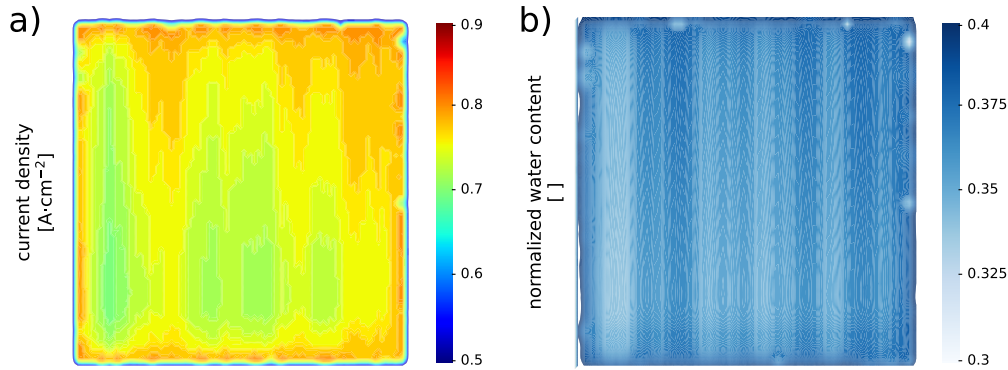


Figure 8.7: Parallel straight channel with stoichiometry ratio 3 a) spatial current density map and b) water content distribution

thickness increases, more water (in absolute terms) is required to reach the capillary pressure breakthrough, p_{bt} . This phenomenon may delay the liquid water expelling, but the average amount of water content per element, the normalized water content, should be similar from simulation to simulation. Thicker GDLs also allow better water diffusion in the xy plane, homogenizing the water content and diluting the effect of the flow field pattern. This effect will ease the water removal from below the ribs. On the other hand, higher GDL thickness implies higher electrical resistance. The GDL electric conductivity is considered constant at least $3500 \text{ mS}\cdot\text{cm}^{-1}$ [171].

In this study, a wide range of GDL thicknesses have been evaluated. Tab. 8.5 shows the configurations tested to evaluate the impact of GDL thickness.

	ID #	w_c/w_r	# ch.	R_{st}	GDL $_{th}$ [μm]
	s3.1	3/5	7	1	500
	s3.2	3/5	7	1	400
	s3.3	3/5	7	1	300
	s1.27	3/5	7	1	253
	s3.5	3/5	7	1	200

Table 8.5: Parameters used in simulations of GDL thickness analysis, Exp_3

The normalized water content (mm^3 of water per mm^3 porous media of GDL) variation within tests is below a 2.5% which has no apparent impact on cell voltage, less than 5 mV, Fig. 8.8. Therefore, the impact of the cell operating voltage on the range of GDL thicknesses studied is not significant. Despite it, it is observed

a difference in evaporation rate which occurs when the GDL thickness varies. Furthermore, the change in evaporation is related to a decrease in voltage variability, σ_v^s . These three effects can be observed in Fig. 8.8.

Other studies [172, 173] observed a more significant effect on the operational point variation due to a change in the thickness of the GDL.

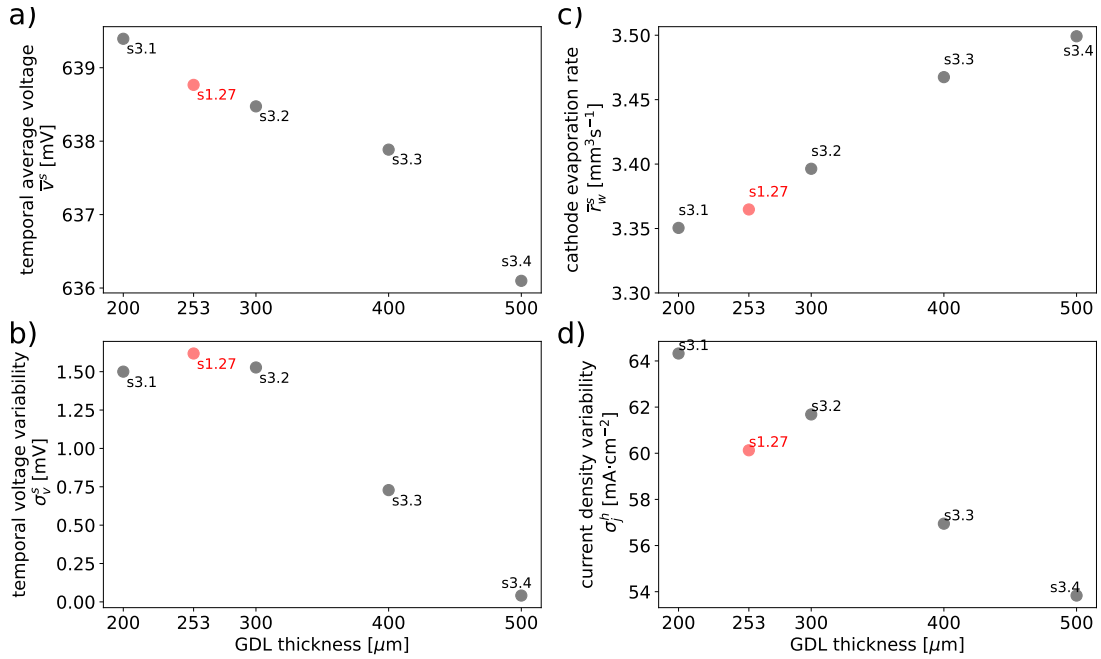


Figure 8.8: Cell performance of different GDL thicknesses (Exp₃) a) temporal average voltage, b) temporal voltage stability, c) evaporation rate, and d) spatial current density variability

The GDL thickness augment increases the evaporation rate, and similarly, the variability of the evaporation rate decreases, as is shown in Fig. 8.9, where the temporal water evaporation rate is represented for each GDL thickness. This effect results from the liquid water reservoir capacity in the GDL. The thicker the GDL thickness, the higher the water volume before it reaches the pressure break-through limit. Other studies [152] related the pressure break-through with the GDL thickness in absolute value. In this thesis, it has been used the normalized water content since it does not depend on GDL thickness.

The impact on absolute water capacity in the GDL can also be observed by analyzing the water break-through behavior via the evaporation rate. The time

from the experiment starting to the first liquid water removal, which corresponds to the first drop in evaporation rate from the GDL, increases when the GDL thickness increases, Fig. 8.9. This effect has also been observed in other PEMFC modeling studies that also used the multiphase Lattice-Boltzman method [174].

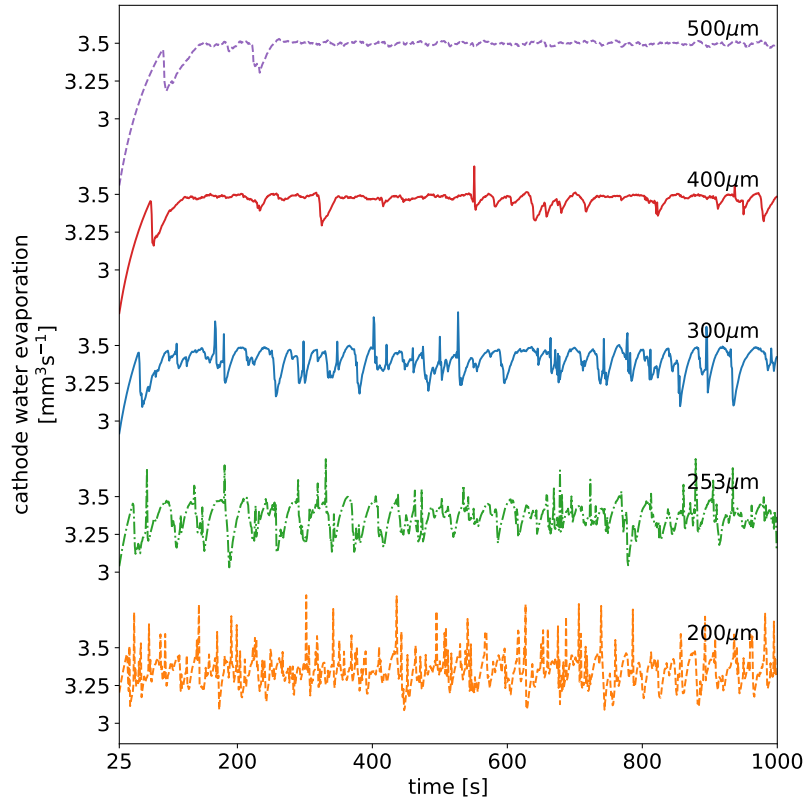


Figure 8.9: Dynamic response of water evaporation rate of the cathode GDL for different GDL thicknesses

In this model, the GDL is not discretized in the z axis; therefore, the water content in this axis cannot be analyzed.

As stated in other studies [174], thicker GDL may have a negative effect on the cell performance since it will accumulate liquid water near the catalytic layers, especially on the cathode, blocking the access of gases.

A spatial current density variability reduction, σ_j^h , is observed as the GDL thickness increase.

This effect can be observed visually in Fig. 8.10 where the spatial current density of three different GDL thicknesses is plotted. This effect is related to

the capacity of liquid water and gases to flow beneath the rib to the channel to ease the water removal.

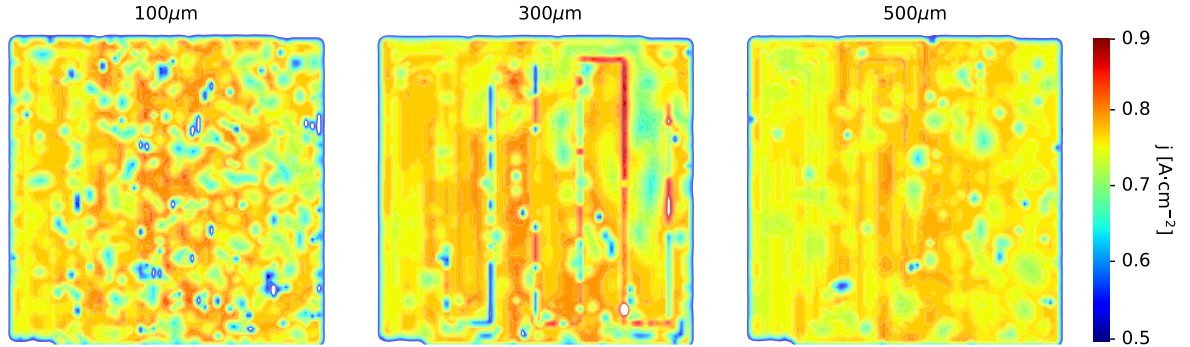


Figure 8.10: Spatial current distribution for three different GDL thicknesses at 500 s experiment time

8.6 Membrane thickness (Exp₄)

The membrane thickness is a relevant parameter of the overall cell performance. In this study, the membrane thickness has been modified in a range to an upper and a lower value to understand the impact of this parameter on the overall cell performance. The conductivity of the membrane, which causes the most significant impact in the ohmic overpotential, only varies depending on the membrane thickness and water content in the simulations. The electrolyte density is considered constant independent of the thickness; therefore, the dry weight of the electrolyte will increase and decrease dependently on the thickness, Eq. (5.20).

An analytical analysis is performed to understand the sensitivity of the membrane thickness parameter in the simulations. As mentioned in the membrane description (section 3.2.1), one of the attributes of this component is to be an electronic insulator to avoid short circuits. Reducing the membrane thickness reduces the electric resistance between the anode and cathode GDLs. An electrical short-circuit could occur in the case of a very thin membrane. Moreover, lower membrane thicknesses increase the probability of gas crossover or membrane breakage [175].

The effect of different membrane thicknesses within a range of water content (in this case, from 30% to 40%) in the polarization curves is analyzed.

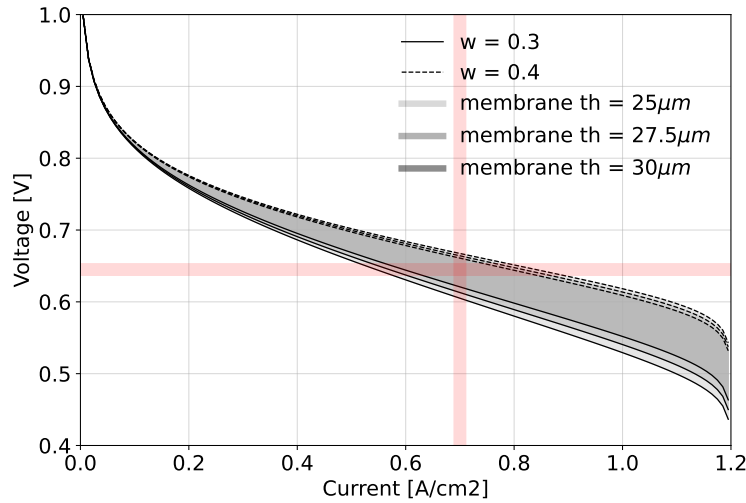


Figure 8.11: Polarization curves function of the membrane thickness within a membrane water content range of 30% and 40%.

The result of this analysis can be observed in Fig. 8.11, where the three different shaded areas represent the behavior in the range of water membrane content for the different membrane thicknesses. It is observed that if the thickness decreases, the variability within the cell performance becomes higher for the same water content range (from 30% to 40%).

To complete this study, three simulations have been performed. Previous, the configuration s1.27 (with a membrane thickness of 27.5 μm) has been simulated and compared against other simulations with 25 μm and 30 μm membrane thickness as shown on Tab. 8.6.

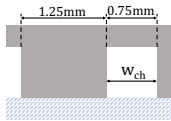
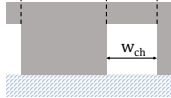

ID #	w_c/w_r	# ch.	R_{st}	m_{th} [μm]
	s4.1	3/5	7	25
	s1.27	3/5	7	27.5
	s4.3	3/5	7	30

Table 8.6: Parameters used in experiment simulations of membrane thicknesses, *Exp₄*

An increase in membrane thickness produces an increase in overpotential, as it is shown in Fig. 8.12, which reduces the power density of the cell.

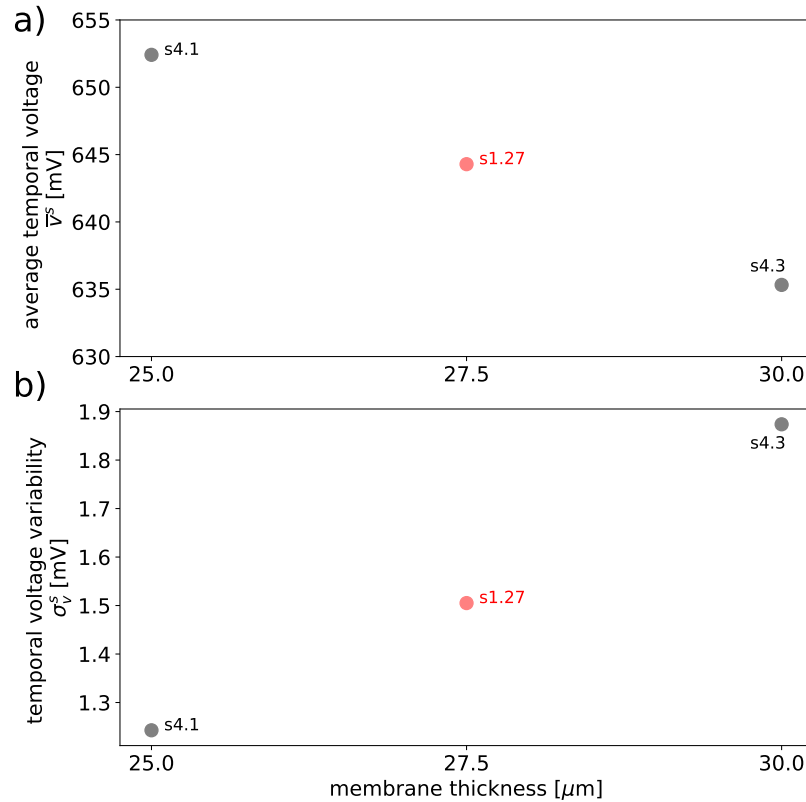


Figure 8.12: Temporal average voltage and standard deviation (SD) of the cell on steady state for different membrane thicknesses

The change in membrane thickness produces a change in the water balance of the cell Fig. 8.13. Thicker membrane produces a reduction of the back-diffusion water transport, Eq. (5.33). This effect counterbalances the electro-osmotic water drag. Therefore the water diffusion becomes higher from the anode side, drying the membrane. As observed, when the membrane thickness decreases, the water content in the anode increases. The evaporation rate in the cathode is higher but stable than the anode due to higher gas flow rates in the flow field and the effect of the electro-osmotic drag. This effect causes the water content in the cathode to be relatively constant. However, the amount of water in the anode decreases due to the water back-diffusion since the membrane thickness increases.

In the spatial performance of the cell, no significant differences can be observed for the different membrane thicknesses, as shown in Fig. 8.14. The only remarkable effect observed is produced in the anode inlet (bottom-left from Fig. 8.14), where a

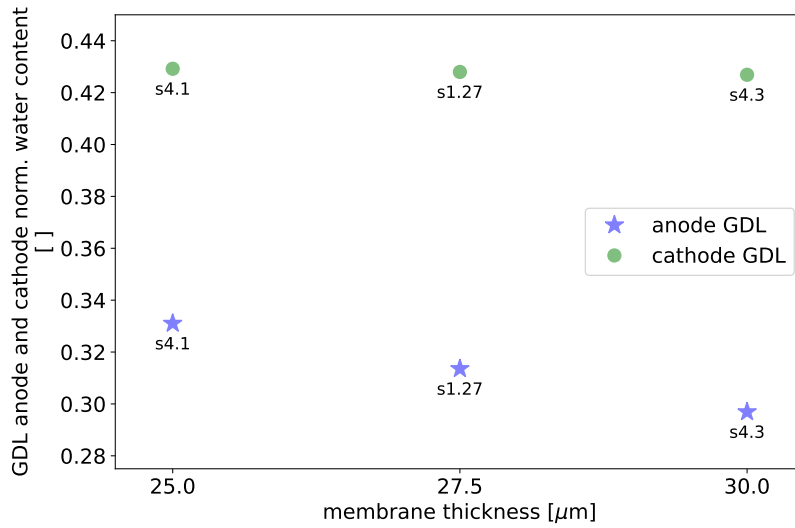


Figure 8.13: Effect in anode and cathode GDL water content for different membrane thicknesses

local decrease in water content is produced if the membrane thickness increases.

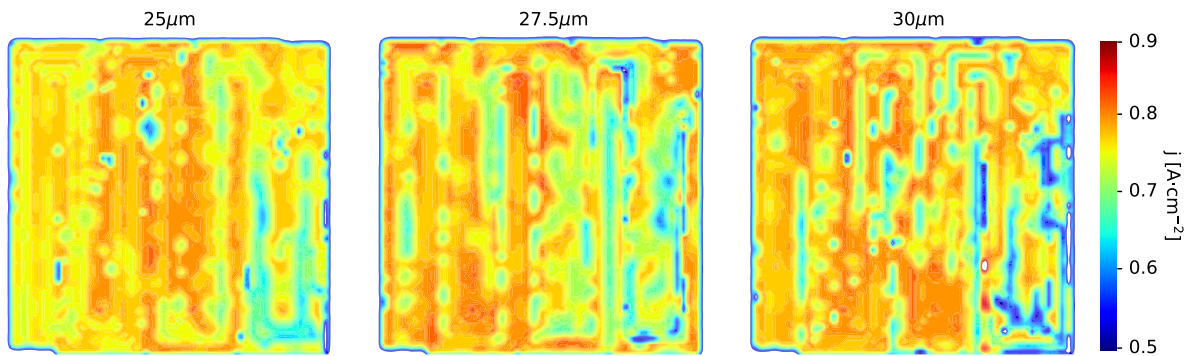


Figure 8.14: Spatial current density distribution for different membrane thicknesses at 500 s time in the experiment simulation

8.7 Temperature (Exp₅)

The temperature has a relevant impact on the cell's performance since it affects the evaporation rate, changes the protonic conductivity of the membrane, changes the membrane water diffusivity, and also varies the contribution of each type of overpotentials, as described in section 5.4.1. Inhere, a simulation study with a different temperature range is performed to observe the effect in the submodels

analyzed in section 5.4.1 and the result in the complete model simulation. In Tab. 8.7, the simulations performed are listed to study the impact of temperature on the cell's performance.

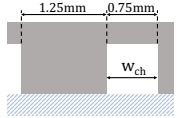
	ID #	w_c/w_r	# ch.	R_{st}	T [°C]
	s5.1	3/5	7	1	50
	s5.2	3/5	7	1	60
	s5.3	3/5	7	1	70
	s1.27	3/5	7	1	80
	s5.4	3/5	7	1	90

Table 8.7: Parameters used in the simulations for temperature analysis, Exp₅

The temporal performance of the experiment simulations has been analyzed in Fig. 8.15-a,b where a direct relationship can be observed with the cell voltage, \bar{v}^s , and the voltage stability, represented by σ_v^s , in the cell. The variability of cell voltage decreases as the temperature increases due to the water content being removed by evaporation instead of a breakthrough mechanism. Liquid water removal by breakthrough mechanism instead of via evaporation produces instability by sudden punctual water content drops in the cell, causing fluctuations in the cell's voltage. As stated in section 5.4.1, the increase in performance is mainly driven by the change in the membrane conductivity due to the temperature increase.

The effect of lower temperature and, therefore, lower evaporation can be directly observed in the cell's spatial homogeneity as shown in Fig. 8.15-c. For lower temperatures, the spatial in-homogeneity is increased with the increment of temperature, and suddenly, between 60-70°C, drops to lower values. This drop results from decreasing the overall water content in the membrane and GDLs due to reaching a temperature threshold.

From the temperature study, the importance of water removal, especially in steam form, in order to reduce instability and improve the spatial homogeneity performance of the cell can be stated. Moreover, by increasing the cell's temperature, the overall performance improves thanks to increasing the membrane's protonic conductivity.

The cell temperature is typically controlled by a cooling system using a fluid, gas, or liquid as a heat exchanger to cool the bipolar plates. The temperature of the

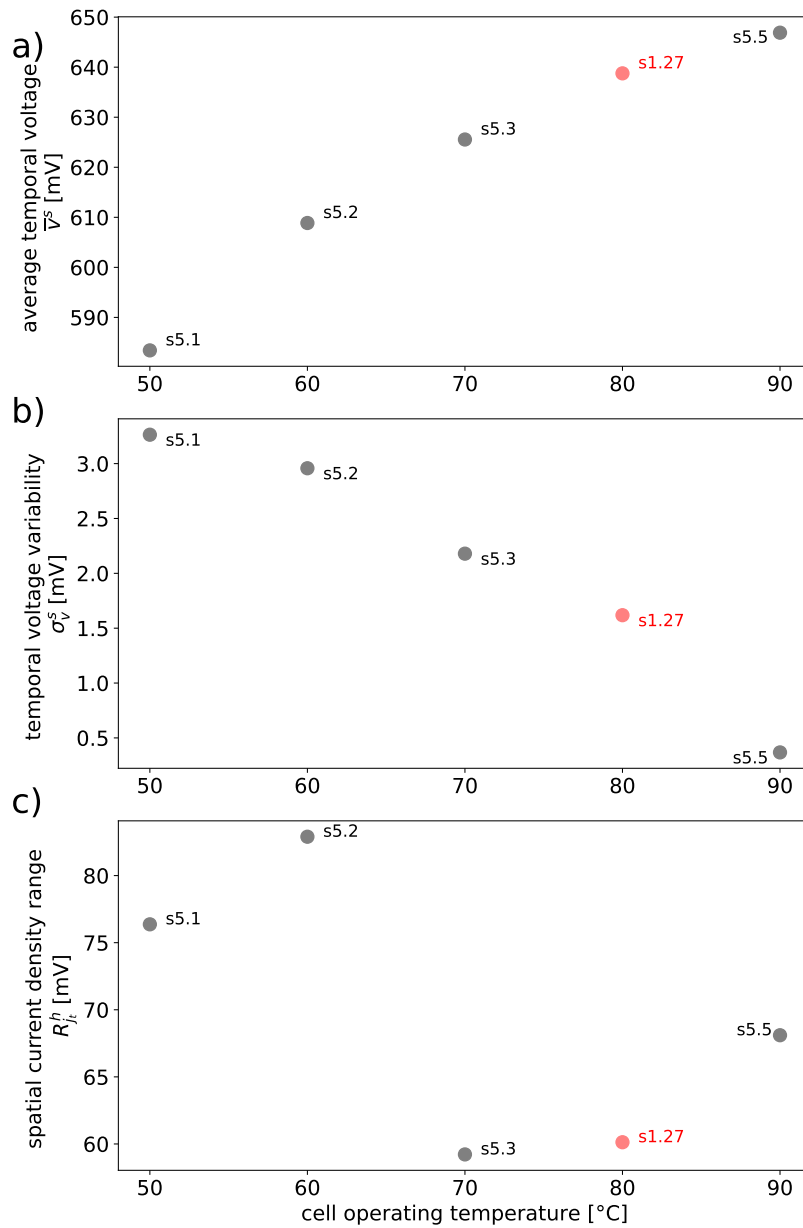


Figure 8.15: Uniformity analysis a) temporal average cell voltage, b) temporal voltage SD, and c) spatial current density SD on steady state for different cell operating temperatures

gas streams can also control the cell temperature, but the heat capacity of the gases is lower; therefore, its cooling capacity is also lower. In this model, the cell is set to a constant homogeneous temperature in the simulations. However, as described, the cooling system's implementation may produce spatial cell performance inhomogeneities, such as channel-rib differences or directional patterns in the direction of the cooling fluid. Implementing the cooling system may also produce condensing

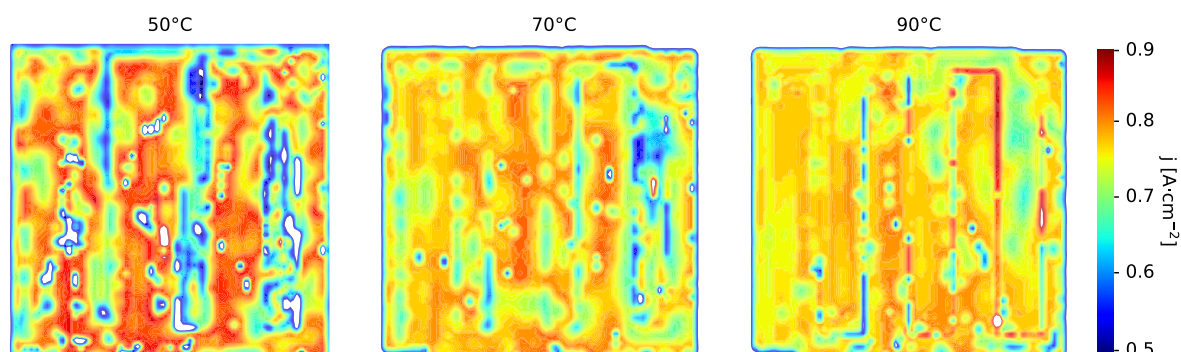


Figure 8.16: Effect different cell operating temperatures in the spatial current density

water areas within the flow field, generating undesired operational effects.

Overall, working at high temperatures (80 - 90°C) reduces the need for cooling power costs and eases the water removal from the cell via evaporation.

8.8 Co-flow and counter-flow (Exp₆)

To study the differences between counter-flow and co-flow, the configurations s1.27 simulation has been taken as a reference and modified to have a co-flow configuration. By using a co-flow configuration, the RH of the cathode and anode will evolve in the same direction, whereas in contrast with the counter-flow, as the cathode increase left-to-right in the anode, it increases right-to-left. A similar phenomenon occurs with fuel consumption. Both flow fields decrease their partial fuel pressure, since they evolve along the flow field. Therefore it is expected to have more spatial differences using the co-flow than the counter-flow configuration. Fig. 8.17 illustrates the reactant consumption and relative humidity of the counter-flow compared with the co-flow configuration.

The parameters used in the experiment simulations of the co-flow or the counter-flow effect are listed in Tab.8.8. The table shows in the column called "gas inlet place" 1 or 0 to indicate the gas inlet position of the anode and cathode, being 0 the inlet situated at the bottom left place of the image, and 1 indicates that the inlet is at the top right corner. The letters "c" or "a" reference if the inlet is of the anode or the cathode. Therefore, c-1 implies that the cathode inlet is in the top right corner.

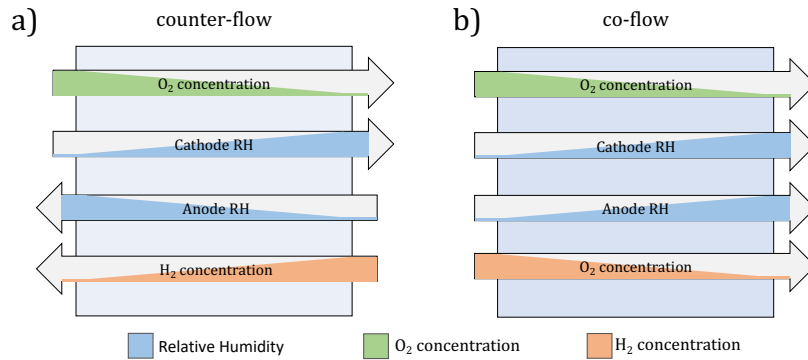


Figure 8.17: Impact on RH and fuel concentration comparing a) counter-flow or b) co-flow configuration

	ID #	w_c/w_r	# ch.	R_{st}	gas flow	gas inlet place
	s6.1	3/5	7	1	co-flow	c-0/a-0
	s6.2	3/5	7	1	co-flow	c-1/a-1
	s1.27	3/5	7	1	counter-flow	c-0/a-1

Table 8.8: Parameters used in co-flow and counter-flow simulations. In column "gas inlet place", 0 indicates inlet at the bottom left, 1 inlet at top right, Exp₆

Fig. 8.18 shows the spatial current density for the three different configurations based on the cathode and anode gas direction relationship. As observed in the figure, the higher and lower current density regions change according to the flow direction. This change is a consequence of both the RH gradient and the fuel consumption, which evolve in the same direction, increasing the non-uniformity performance of the cell. The most balanced configuration is the counter-flow, as illustrated in Fig. 8.17. In the simulations performed, the average water content across all the simulations is stable, since the current demand is stable. Fig. 8.18 shows that the non-uniform spatial distribution of the current density could cause in-homogeneous degradation of the cell.

8.9 Conclusions

In this chapter, the model simulation has been used to analyze the impact of different parameters in the uniformity performance of the cell. The impact of the number of parallel channels in the parallel serpentine flow field design, the stoichiometry ratio,

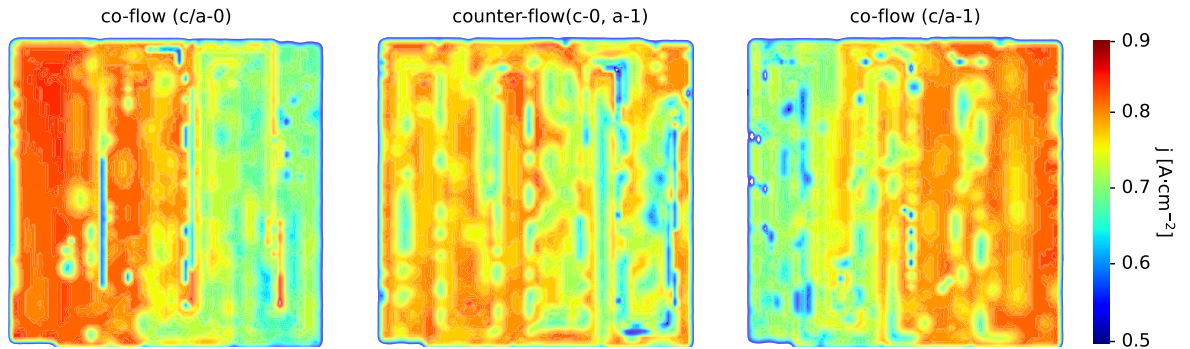


Figure 8.18: Spatial current density distribution comparing counter-flow and co-flow simulations

and the w_c/w_r ratio have been studied. For the studied range of cell configuration parameters, the better performing design consisted of 7 parallel channels and a stoichiometric ratio of 1 (with respect original), since this setup consumed the lesser fuel, obtaining the highest spatial homogeneity and stability results.

The results of the parallel serpentine design have been compared with a straight parallel channels design, confirming the impact of gas speed on the cell's stability and the need for a minimum gas flow rate to evacuate liquid water from the flow field.

The better-performing cell setup is used as an experimental baseline, varying design, and operational parameters: a) the GDL thickness, b) membrane thickness, c) the operating temperature, and d) co-flow and counter-flow designs.

From the simulations on GDL thickness, minor differences have been observed in the cell's performance. The absolute water content in the cell increases as the GDL thickness increases and the amount of water evaporated. This effect produces a more uniform performance on the cell.

From the simulation results on membrane thickness, it has been observed that changes in the membrane thickness modify the water content balance between the anode and the cathode due to the back-diffusion effect, modifying the operating voltage of the cell in galvanostatic mode. The thicker the membrane, the higher the difference in water content between the anode and the cathode. The increase in membrane thickness has a notable effect on the cell's operating point since the membrane's protonic resistance becomes higher if the thickness is increased.

On the cell temperature analysis, it is observed that lower temperatures reduce evaporation, and water must be removed in liquid form from the cell, causing instabilities in cell performance. Higher temperatures, despite increasing evaporation rate, change the cell's operating point due to a change in the conductivity of the membrane with temperature.

Finally, in the counter-flow and co-flow simulations comparison, it has been shown the impact of RH and fuel consumption in the overall cell uniformity proves the importance of those contributors to the spatial current density homogeneity.

All in all, this chapter's simulations show the model's capabilities and the simulation procedure to represent a variety of different setups successfully, providing valuable insights into parameter configuration for spatial uniformity and temporal stability cell performance. All of the dynamic long-term simulations performed are only possible because of the optimization of the computational cost of the simulation procedure.

9

Conclusions and future work

9.1 Conclusions

This thesis presents the development of a PEM fuel cell pseudo-3D dynamic model capable of analyzing the homogeneity and stability of the cell's performance since the uniform performance increases the durability and robustness of the cell, decreasing the maintenance cost. The model is focused on water management in steam and liquid phases, including the liquid droplet movement in the flow fields. The simulation procedure allows the long-term and accurate analysis of different flow field patterns, designs and operational parameters with low computational effort.

The main conclusions of this thesis are presented as follows:

- The developed model is composed of a set of submodels that can be simulated individually. This feature allows the simulation of the complete model by sequentially simulating the submodels. This procedure allows for optimizing the computational effort and increasing the simulations' robustness without affecting the results' accuracy.
- The model has been validated with experimental data by spatially and temporally analyzing water and current density distribution using neutron-imaging and segmented cell methods. The experiments studying the impact

of RH inlet gas cycles in current density distribution and voltage in a 141 cm², 23 channels parallel serpentine cell, and the drying/re-humidification due to droplet insertion in a 25 cm² single serpentine cell were used for the validation procedure.

- The simulation model has been used to evaluate the effect of varying design and operational parameters, such as the channel-rib ratio, stoichiometry ratio, membrane thickness, GDL thickness, temperature, and co-flow and counter-flow, on the homogeneity and stability of the cell's performance.

The main conclusions obtained from the simulation results are as follows:

- The speed of gases has an important role in removing water droplets from the channels to avoid local water flooding, improving the uniformity performance of the cell.
- For a specific cell size, there is a characteristic number of channels in the flow field configuration, which optimizes the spatial and temporal uniformity of the cell performance.
- The increase in GDL thickness increases the homogeneity performance of the cell.
- Due to the back-diffusion effect, the decrease in membrane thickness homogenizes the amount of water diffused from cathode to anode GDLs.
- The decrease in the cell temperature reduces the evaporation rate, which increases the current density variability.
- Co-flow configuration decreases the uniform performance of the cell compared with counter-flow configuration.

Within the studied parameter ranges of the fuel cell, the 100 cm² active area configurations operating at 50% RH feeding in the anode and cathode in counter-flow, using 7 channels and the narrower channels (channel width of 0.75 mm and rib width of 1.25 mm), using and stoichiometry ratio of 1.2 in the anode and 2 in the cathode

operating at 80° C using a 253 μm GDL and a 27.5 μm membrane thickness provided the better-performing cell in terms of temporal stability and spatial homogeneity.

This configuration provided high gas flow at a lower stoichiometry ratio which ease the liquid droplets removal from the flow field while reducing the waste of fuel.

9.2 Future work

The following guidelines for future work are proposed:

- Increase the computational efficiency of the simulations by implementing the submodels of the parts that can still slow down the complete simulation time in C++ language. Also, with the aim of improving the computational cost, design the simulation procedure in multi-threading processing and be able to be used in multiprocessor computers.
- Extending the isothermal models used to dynamic and spatial temperature-dependent models to represent better the heat transfer produced by gas flows and the heat generation due to electrochemical reactions.
- Extend models to non-isotropic models, which can represent the spatial inhomogeneity of some physical properties of materials, such as water diffusion in the GDL and membrane.
- Use the simulation procedure employed in this thesis on DMFC or SOFC models.

A

Nomenclature

Greek Symbols

β	Conductivity model exponential parameter	[-]
$\Delta\theta_A$	Droplet approximate advancing deformation	[m]
ϵ	Porosity	[-]
η	Dynamic viscosity	[Pa·s]
γ	Surface tension of the liquid	[N·m ⁻¹]
λ_m	Water content in the membrane	[H ₂ O/SO ₃]
\mathcal{A}_{ij}	SM matrix of fluxes in each coordinate direction	[m·s·mol ⁻¹]
ν	Kinematic viscosity	[N·m·kg ⁻¹]
ρ_i	Element i density	[kg·m ⁻³]
$\sigma_{r_w}^s$	Temporal liquid water removal rate variability	[mm ³ ·s ⁻¹]
σ_v^s	Cell voltage temporal standard deviation	[mV]
σ_0	Hydrated membrane electric conductivity	[S·m ⁻¹]
σ_j^h	Spatial current density variability	[mA·cm ⁻²]
$\sigma_{m,0}$	Reference membrane electric conductivity	[S·m ⁻¹]

σ_m	Membrane electric conductivity	[S·m ⁻¹]
σ_P^s	Temporal pressure drop variability	[kPa]
σ_p^s	Temporal power density variability	[mW·cm ⁻²]
$\sigma_{r_e}^s$	Temporal evaporation rate variability	[mm ³ ·s ⁻¹]
σ_W^s	Temporal normalized water content in cathode or anode variability	[-]
τ	Porous media tortuosity	[-]
θ	Droplet contact angle	[rad]
θ_A	Droplet advancing angle	[rad]
θ_R	Droplet receding angle	[rad]
θ_S	Droplet static contact angle	[rad]

Roman Symbols

A_d	Droplet gas flow perpendicular area	[m ²]
A_{ef}	Effective area	[m ²]
a_{evp}	Holterman droplet evaporation constant	[m ² ·s ⁻¹]
a_k	Water activity	[]
b_1	Membrane conductivity constant	[5.139·10 ⁻³]
b_2	Membrane conductivity constant	[3.26·10 ⁻³]
b_3	Membrane conductivity constant	[1268]
b_{evp}	Holterman droplet evaporation constant	[s ^{1/2} ·m ⁻¹]
C	Sum of gases concentrations	[mol·m ⁻³]
C_j	Gas concentration of the j^{th} element	[mol·m ⁻³]
C_{CL}	Contact line constant	[kg·m ⁻¹]
C_D	Dragging coefficient	[-]
c_D	Droplet dynamic chord	[m]
$C_{H_2,0}$	Reference O ₂ concentration	[mol·m ⁻³]

C_{H_2}	Reference O ₂ concentration	[mol·m ⁻³]
$C_{O_2,0}$	Reference O ₂ concentration	[mol·m ⁻³]
C_{O_2}	Reference O ₂ concentration	[mol·m ⁻³]
c_S	Droplet static chord	[m]
d	Distance	[m]
d^c	Critical distance between two droplets to coalesce	[m]
D_λ	Liquid water diffusion coefficient in the membrane	[m ² ·s ⁻¹]
D_d	Droplet diameter	[m]
D_h	Hydraulic diameter	[m]
$D_{i,j}$	Binary coefficient of the i^{th} component on the j^{th} component	[m ² ·s ⁻¹]
d_p	Pore diameter	[m]
D_T	Corrected liquid water diffusion coefficient with temperature	[m ² ·s ⁻¹]
$D_{v,f}$	Average water diffusion coefficient in air	[m ² ·s ⁻¹]
dh	Space interval between two elements	[m]
dt	Time interval within two steps of a simulation	[s]
E	Cell potential at equilibrium	[V]
E_0	Open circuit voltage	[V]
e_r	Relative roughness of the duct	[-]
EW	Equivalent weight	[g · mol ⁻¹]
F	Faraday constant	96485 [s·A·mol ⁻¹]
f	Darcy friction coefficient	[m]
$F_{adh,S}$	Simplified adhesion force	[N]
F_{adh}	Droplet adhesion force	[N]
f_b	forced flow in Neumann boundary	[-]
F_{drag}	Droplet dragging force	[N]

G	Gibbs energy	[J]
g_f	Formation Gibbs energy	[J]
H	Enthalpy	[J]
h_c	Channel height	[m]
h_d	Droplet height	[m]
h_f	Formation enthalpy	[J]
IEC	Ionic exchange capacity	[meq·g ⁻¹]
J	Fluxes	[mol·m ⁻² ·s ⁻¹]
j	Current density	[A·cm ⁻²]
j_0	Exchange current density	[A·cm ⁻²]
J_{bd}	Back diffusion flow	[mol·m ⁻² ·s ⁻¹]
J_{eo}	Electro-osmotic drag flow	[mol·m ⁻² ·s ⁻¹]
\bar{j}^h	Spatial average current density	[mA·cm ⁻²]
K	Permeability of the porous media	[m ²]
$k_{d,evp}^*$	Evaporation area correction for droplet evaporation	[-]
k_{adh}	Constant adhesion force function of droplet shape	[-]
k_{con}	Condensation constant from porous media	[s ⁻¹]
k_{evp}	Evaporation constant from porous media	[Pa ⁻¹ ·s ⁻¹]
k_{rl}	Liquid relative permeability	[-]
L	Length	[m]
M	Molar weight of the i^{th} component	[kg·mol ⁻¹]
m^g	Water mass in steam phase	[g]
m_{dry}	Mass of the Nafion membrane dry	[g]
m_d	Droplet mass	[kg]
m_{wet}	Mass of the Nafion membrane wet	[g]

n	Number of moles	[-]
n_d	Electro-osmotic drag coefficient	[]
\bar{P}^s	Temporal average pressure drop	[kPa]
\bar{p}_t^s	Temporal average power density	[mW·cm ⁻²]
p_{bt}	Porous media break-through capillary pressure	[Pa]
P_c	Capillary pressure	[Pa]
P_d	Droplet perimeter	[m]
P_i	Partial pressure of the i^{th} component	[Pa]
p_{st}	Porous media steady decayed capillary pressure	[Pa]
Q_g	Volumetric flow of the gas	[m ³ ·s ⁻¹]
R	Universal gas constant	[J·mol ⁻¹ ·K ⁻¹]
\bar{r}_e^s	Temporal average evaporation rate	[mm ³ ·s ⁻¹]
\bar{r}_w^s	Temporal average liquid water removal rate	[mm ³ ·s ⁻¹]
R_d	Droplet radius static	[m]
$R_{j_t}^h$	Temporal voltage range	[mV]
R_{st}	Stoichiometry ratio multiplier with respect the original stoichiometry	[-]
Re	Reynolds number	[-]
S	Entropy	[J·K ⁻¹]
s	Normalized water content	[-]
S_{cond}	Condensate water	[m ³]
$S_{d, evp}$	Droplet volumetric water evaporation rate	[m ³ ·s ⁻¹]
S_{evp}	Evaporate water	[m ³]
s_f	Formation entropy	[J·K ⁻¹]
S_{H_2O}	Molar H ₂ O generation	[mol·s ⁻¹]
S_{H_2}	Molar H ₂ consumption	[mol·s ⁻¹]

S_{O_2}	Molar O ₂ consumption	[mol·s ⁻¹]
T	Temperature	[K]
t_d	Droplet width	[m]
t_j	j^{th} time step of the simulation	[s]
th	Thickness	[m]
\bar{u}_g^s	Temporal average gas speed	[m·s ⁻¹]
u_d	Droplet advancing speed	[m·s ⁻¹]
u_{ef}	Effective speed	[m·s ⁻¹]
u_g	Gas speed	[m·s ⁻¹]
V_{act}	Activation losses	[V]
V_{con}	Concentration losses	[V]
V_d	Droplet volume	[m ³]
V_{fc}	Voltage of the cell	[V]
V_m	Bounding box volume of the membrane	[m ³]
V_{ohm}	Ohmic losses	[V]
\bar{W}^s	Temporal average normalized water content in cathode or anode	[-]
w_c	Channel width	[mm]
W_{dry}	Weight of the membrane in dry conditions	[g]
w_r	Width of the rib	[mm]
w_t	Total width of channel plus rib	[mm]
W_{wet}	Weight of the membrane in wet conditions	[g]
WU	Ratio between dry and wet membrane water uptake	[-]
WU^c	Ratio between dry and wet membrane threshold water uptake	[-]
\bar{x}_{mfp}	Mean molecular free path	[m]
$x_{d,CM}$	Droplet x center of gravity	[m]

X_i	Molar fraction of the i^{th} element	[-]
#ch.	Number of channels on the configuration	[-]

Superscripts

c	Critical
h	Homogeneity parameter
n	New
s	Stability parameter
vap	Referring to vapour
sat	Saturated, in terms of pressure

Subscripts

*	Corrected with respect other factors
λ	Referring to the value with respect the current water activity, λ
λ, T	Referring to the value with respect the current water activity and temperature, λ and T
a	Absorption
adh	Adhesion, regarding forces
bd	Back diffusion
bt	Referring to the break trough drain condition
c	Channel when referring to dimensions
CM	Center of masses
con	Condensation
D	Dynamic
d	Droplet
$drag$	Drag, regarding forces
$drain$	Referring to the liquid flow in break-through conditions

<i>eo</i>	Electro-osmotic	
<i>evp</i>	Evaporation	
<i>f</i>	Formation, referring to the entropy or the enthalpy	[J·K ⁻¹]
<i>g</i>	Referring to the state of the matter, liquid	
<i>GDL</i>	Referring to the gas diffusion layer (GDL)	
<i>k</i>	Spatial <i>k</i> th element the 1D dimensions line	
<i>K_n</i>	Referring to the Knudsen parameter	
<i>l</i>	Referring to the state of the matter, liquid	
<i>m, T0</i>	Referring to the membrane at the reference temperature <i>T</i> ₀	
<i>m, T1</i>	Referring to the membrane at the calculated temperature <i>T</i> ₁	
<i>mfp</i>	Mean free path	[m]
<i>p</i>	particle	[m]
<i>S</i>	Static	
<i>sat</i>	Saturation state	
<i>st</i>	Referring to the stop drain condition	
<i>t</i>	value of the t-time step	
<i>tot</i>	Referring to total when in concentration or pressure	
<i>x</i>	Referring to an specific axis	
<i>act</i>	Activation	
<i>con</i>	Concentration	
<i>m</i>	Membrane	
<i>ohm</i>	Ohmic	

B

List of Figures

3.1	PEM fuel cell components overview	18
3.2	SEM image of PEM fuel cell MEA [48]	19
3.3	Conceptual design of a PEM fuel cell with its components	24
3.4	Example of some flow field designs (The gray area represents the surface of the bipolar layer resting on the diffusion layer), a) single serpentine, b) interdigitated, c) parallel straight channels, and d) pins designs.	26
4.1	Model classification homogeneous function of their attributes.	41
5.1	Conceptual representation of the different phenomena of water exchange in the cell a) droplet evaporation in the flow field, b) liquid water evaporation from the GDL, c) flow field to GDL steam condensation, d) GDL liquid break-through, e) liquid water re-absorption in the steam phase, f) electro-osmotic drag, g) back diffusion, h) water generation, i) in-plane diffusion.	51
5.2	Maximum theoretical performance of a PEM fuel cell function of its temperature	59

5.3	Membrane conductivity function of the temperature and normalized water content	62
5.4	Simulation of polarization curve and the contribution of the different overpotentials	64
5.5	Simulation of polarization curve function of the operating temperatures.	65
5.6	Simulation of polarization curve function of the operating gas pressures in anode and cathode	66
5.7	Simulation of polarization curve function of normalized water content in the membrane	67
5.8	Simulation of power density function voltage different values of the water content of the membrane	68
5.9	Comparison of Springer model [130] and Vetter model [122] at 80 °C	70
5.10	Water diffusion coefficient function of the normalized water content and the temperature.	71
5.11	Capillary pressure function of a) the normalized water content on the x-axis, b) in the GDL porosity range (40-80%) the colored areas, and c) different values of GDL water permeability, K	76
5.12	a) the evaporation rate function of the RH (the colored area from 50% to 90%, the dashed line) and the temperature and b) the effect of the porosity in the evaporation rate considering RH 50% and temperature 80 °C for different normalized water content in the GDL.	78
5.13	Example of the relationship between actual pore water content and capillary pressure in a given GDL with the maximum water capillary pressure breakthrough, p_{bt} , and the stable decayed capillary pressure, p_{st}	80
5.14	Scheme of phenomena involved the variation of concentration of species in the flow field. The phenomena described are a) evaporation from a droplet; b) liquid water evaporation from the GDL; c) steam condensation into liquid water in the GDL; and d) consumption of reactants	83

5.15	RH evolution along the linear channel of 100 mm length with respect to a) different cathode airflow speeds and b) the operating temperatures	85
5.16	Water content evolution along the linear channel of 100 mm length with respect to a) different cathode airflow speeds and b) the operating temperatures	86
5.17	Scheme of adhesion force of a droplet deformed by gas flow	89
5.18	Gas flow effect on a droplet geometry over a hydrophobic surface a) when the gas flow is zero (static) and b) when the gas flow is positive (dynamic)	89
5.19	Steady state droplet advance speed function of droplet volume and gas speed	94
5.20	Steady state droplet advance speed function of droplet volume and contact angle	95
5.21	a) droplets at a distance which will not coalesce, b) droplets at the critical coalescence distance	96
5.22	Scheme of a droplet contacting with two perpendicular surfaces of the channel, a) real contact and b) simplification	98
6.1	Simulation flow chart with marked in the dashed red rectangle the submodels implemented in C++	103
6.2	Illustration showing a) the MEA xy -mesh, b) the linear-discretization, and c) the linear-discretization converted into a pseudo-2D approach.	107
6.3	Scheme of grouping GDL discretization elements into flow field discretization regions	108
6.4	Illustration representing the two kinds of discretization, the xy -mesh and the linear-discretion with the regions used in the complete model	109
6.5	Representation of a) flow field's channel turn in the 2D plane with the used discretization l_i , and the regions r_k , as explained in section 6.3, and b) the same channel (a) using the 1D discretization	113
6.6	Example of FDM mesh using artificial nodes for Neumann boundary condition using the FTCS approach.	114

6.7	Droplet positions in a 1D channel at a) initial time and b) after a time step interval. The rectangles below the surface represent the amount of water in the GDL at each region	117
7.1	Humidification cycle used in validation procedure	121
7.2	Effect of different time step sizes in the RH cycles simulation. a) Voltage response for 5, 2, 1, and 0.5 s and b) voltage error between each time step size response and the 0.5 s.	122
7.3	Parallel serpentine flow field, 23 channels, 0.8 mm channel width, 1 mm rib width, 3 loops. Segmented cell divided into 9x10 segments.	124
7.4	Spatial current density comparison of the experimental and simulation results for the RH in the setup shown in Tab. 7.2	125
7.5	Simulated results of partial pressure of a) Oxygen in the cathode and b) Hydrogen in the anode of simulation S.3	126
7.6	Flow field (single serpentine cell, 1x1 mm ² section) used in the validation of drying and re-humidification cycle experiment	127
7.7	RH inlet levels and liquid water injection flow on the drying and humidification cycles simulation validation.	128
7.8	Spatial distribution of water content during droplet injection in experimental and simulation, and the spatial distribution of current density in the simulation	129
7.9	Comparison on average current density between data and simulation	130
7.10	Dynamic performance of a) amount of water in each side of the cell with the current density, and b) different water transfer rate contribution and the total water transfer rate	131
7.11	Simulation results at experiment time 10 s after droplet injection (blue marker on Fig.7.9) a) Water content in the cell in the three spatial axes, b) in-plane water content distribution in the anode flow field, and in the anode and cathode GDLs.	132

8.1 Representation of 4 parallel serpentine flow field designs used in the uniformity study. From left to right, number of parallel channels and MEA surface a) 5 channels, 10x10.4 cm, (s.4, s.8, s.12, s.16, s.20, s.24, s.28, s.32, s.36) b) 7 channels, 10x10.2 cm (s.3, s.7, s.11, s.15, s.19, s.23, s.27, s.31, s.35), c) 9 channels, 10x11.2 cm (s.2, s.6, s.10, s.14, s.18, s.22, s.26, s.30, s.34), and d) 11 channels, 10x11.4 cm (s.1, s.5, s.9, s.13, s.17, s.21, s.25, s.29, s.33). 142

8.2 Relationship of a) voltage SD, σ_v^s , b) spatial current density SD, σ_{jt}^h , and c) average power density, \bar{p}_t^s , of the different simulation setups with the cathode nominal gas speed 145

8.3 Voltage SD related to the number of channels, ratio C-R, and stoichiometry ratio 146

8.4 Spatial current density SD at the time 500 s related to the number of parallel channels, the ratio C-R, and the stoichiometry ratio. . . 146

8.5 Comparison of a) a low number and b) a high number parallel channel in serpentine design for approximately the same cell size 147

8.6 Spatial current density and water content comparison between simulation s.11 and s.35 at the time step 500 s. Seven parallel serpentine channels and 1.7 cathode stoichiometry are used in both configurations. The C-R width ratio is 5/3 for s.11 and 3/5 for s.35 148

8.7 Parallel straight channel with stoichiometry ratio 3 a) spatial current density map and b) water content distribution 150

8.8 Cell performance of different GDL thicknesses (Exp₃) a) temporal average voltage, b) temporal voltage stability, c) evaporation rate, and d) spatial current density variability 151

8.9 Dynamic response of water evaporation rate of the cathode GDL for different GDL thicknesses 152

8.10 Spatial current distribution for three different GDL thicknesses at 500 s experiment time 153

8.11 Polarization curves function of the membrane thickness within a membrane water content range of 30% and 40%.	154
8.12 Temporal average voltage and standard deviation (SD) of the cell on steady state for different membrane thicknesses	155
8.13 Effect in anode and cathode GDL water content for different membrane thicknesses	156
8.14 Spatial current density distribution for different membrane thicknesses at 500 s time in the experiment simulation	156
8.15 Uniformity analysis a) temporal average cell voltage, b) temporal voltage SD, and c) spatial current density SD on steady state for different cell operating temperatures	158
8.16 Effect different cell operating temperatures in the spatial current density	159
8.17 Impact on RH and fuel concentration comparing a) counter-flow or b) co-flow configuration	160
8.18 Spatial current density distribution comparing counter-flow and co-flow simulations	161

C

List of Tables

5.1	Summary table of the classification of each implemented submodel	56
7.1	Main parameters used on the simulation	124
7.2	Stability of simulations with different RH in anode and cathode used in the model validation procedure	125
7.3	Comparison of voltage stability in the experiments and the simula- tions used in model validation using different RH setups	126
7.4	Parameters used on the experimental simulations where dt is the time step, dx the MEA XY spatial discretization, w_c the width of the channel, h_c the height of the channel, #ch. the number of channels, RH_x the cathode or anode humidity, θ_s the contact angle of the GDL.	128
7.5	Computation time to simulate of one time step (1 s) for 25 cm ² , 100 cm ² and 141 cm ² cell surface.	134
8.1	Stability and homogeneity parameters table	140
8.2	Parameters and values used in Exp ₁	142
8.3	Design table of simulated experiment varying parameters: channel-rib width ratio, w_c/w_r , number of channels in the flow field, # parallel channels, and stoichiometry ratio, R_{st}	143

8.4	Parameters used in the simulations of parallel straight channels design, Exp ₂	149
8.5	Parameters used in simulations of GDL thickness analysis, Exp ₃ . .	150
8.6	Parameters used in experiment simulations of membrane thicknesses, Exp ₄	154
8.7	Parameters used in the simulations for temperature analysis, Exp ₅ .	157
8.8	Parameters used in co-flow and counter-flow simulations. In column "gas inlet place", 0 indicates inlet at the bottom left, 1 inlet at top right, Exp ₆	160

D

Implementation code samples

Contents

D.1 Electrochemical model	184
D.1.1 Voltage and current density calculation	184
D.1.2 Electrochemical model	186
D.1.3 Activation overpotential	186
D.1.4 Ohmic overpotential	186
D.1.5 Concentration overpotential	187
D.1.6 Electro-osmotic drag	188
D.1.7 Back-diffusion algorithm	188
D.2 GDL Model	189
D.2.1 FTCS algorithm	189
D.2.2 Liquid water removal from GDL	191
D.2.3 Water evaporation from the GDL	192
D.2.4 Water condensation from the GDL	193
D.3 Droplet movement	194

This chapter contains samples of the code implementation of the simulation solver. The functions or models selected to be shown are chosen as having specific implementations worth mentioning.

D.1 Electrochemical model

D.1.1 Voltage and current density calculation

This submodel is implemented in C++ as it evaluates the current density and the voltage for each plane element xy . A cell may operate in a) galvanostatic mode and b) potentiostatic model.

When operating in galvanostatic mode the total current generated by the cell is known, j_{total} , but depending on the state conditions of each point in the xy (water content, partial pressures, humidity, temperature) the local current density will vary for the same cell voltage. The overall voltage of the cell will fluctuate to adapt depending on the different state conditions for the same current density. For instance, a cell with a known j_{total} and 40% RH on the cathode flow field inlet will have a different voltage than the same cell operating at 60% RH on the cathode flow field inlet. Therefore, the model implemented has to use a search algorithm to find the overall operating point.

The search algorithm used is the binary search, which will set a starting operating voltage, V_i . It will calculate the overall current of the cell with this operating point and the conditions in each element of the cell. If the j_{total} found is greater than the expected, j_{target} , the V_i will be updated with a higher value. If the j_{total} is lower than j_{target} , the V_i will be decreased. This algorithm will continue until the absolute difference between j_{target} and j_{total} is lower than the maximum allowed error. This procedure is shown in pseudo-code in Alg. 4. This pseudo-code uses the function "solvejV" which calculates the current density of each element for a given V_i . Cod. 1 shows part of the actual code implemented in C++ to find the system's operating point.

Algorithm 4 Pseudo-code to calculate the operating point of the cell in galvanostatic mode

```

error = 10**6
Vmax = 1.2
Vmin = 0.1
while error > maxError do
  Vi = 0.5*(Vmax+Vmin)

  for all nodes do
    | jtotal += solvejV(Vi, conductivities, Vacts, Ers, constants)
  end
  error = abs(jtotal - jtarget)
  if jtotal > jtarget then
    | Vmax = Vi
  else
    | Vmin = Vi
  end
end

```

Code 1 Piece of code implemented in C++ to calculate the operating point of the cell in galvanostatic mode

```

while (abserror > maxError && its < maxIts) {
  jTotal = 0;
  vTarget = 0.5*(vmin+vmax);
  wavg = 0;
  for (int i = 0; i < nLen; i++){
    wi = 0.5*(w_cath[i] + w_anod[i]);
    Pa = P_anod[i];
    Pc = P_cath[i];

    j = solvejV_fast(vTarget, conductivities[i], vactivations[i], Ers[i], ←
      constant);

    js[i] = j;
    jTotal = jTotal + j;
    wavg = wavg + wi;
  }

  jTotal = jTotal*A_cm2;
  error = ref_val-jTotal;

  abserror = abs(error);

  if (error > 0) {
    vmax = vTarget;
  }
  else {
    vmin = vTarget;
  }
  its++;
}

```

D.1.2 Electrochemical model

The electrochemical model of the fuel cell is described in section 5.4.1. Eqs. (5.14, 5.23, 5.26) describe the overvoltage of the fuel cell. Those equations are implemented into the model in C++ as each element of the cell xy discretization is evaluated. The following subsections show the specific implementation of each overpotential.

D.1.3 Activation overpotential

The activation overpotential model is described in section 5.4.1, and the implementation of this model is shown in Cod. 2.

Code 2 Piece of code implemented in C++ to calculate the activation overpotential

```
float activationVoltage(float j, float A = 1, float jn = 1, float jo = 1)
{
    float num = (j+jn)/jo;
    if (num < 0.001) {
        num = 0.5;
    }
    float vcon = A*log(num);
    return vcon;
}
```

D.1.4 Ohmic overpotential

The ohmic overpotential is described in section 5.4.1. The ohmic overpotential requires the calculation of the actual conductivity of the membrane and the actual current density. As the cell is solved iteratively, calculating the electric conductivity at every iteration would be very expensive computationally. Therefore, the ohmic overpotential is calculated in two stages to accelerate the calculations. The conductivity of the membrane only depends on the amount of water in the membrane; therefore it is first calculated of all the mesh elements of the cell. Later, the overpotential, which depends on the actual current density, is calculated within the iterative loop. In Cod. 3, the portion where the conductivity is calculated is shown.

Code 3 Piece of code implemented in C++ to calculate the conductivity of an element

```
float membraneConductivity_Yin(float wi, float membraneTh = 0.0000275, float jn ←
= 1, float Wc = 5.5, float Betta = 0.126, float K_Scm0 = 0.0043, float wdry ←
= 55, float porosity = 0.5){

    float roH2O_gm3 = 1000000;
    float mass_h2o = roH2O_gm3*membraneTh*porosity*wi;
    float wt = mass_h2o/(mass_h2o+wdry);

    if (wt*100 < Wc) {
        wt = Wc/100.;
    }

    float K_Scm = K_Scm0*pow((wt*100 - Wc), Betta);

    return K_Scm;
}
```

D.1.5 Concentration overpotential

The concentration overpotential model is described in section 5.4.1 and is calculated once at every time step outside of the iterative loop, since it does not depend on the actual current density. In Cod. 4, the portion where the conductivity is calculated is shown.

Code 4 Piece of code implemented in C++ to calculate the conductivity of an element

```
float concentrationVoltage(float P_o2, float P_h2, float P02_threshold = 0.325, ←
float PH2_threshold = 1)
{
    float alpha_c = 0.509;
    float RT_anF = 1;
    RT_anF = 8.31*350/(alpha_c*2*96485);

    if (P_o2 > P02_threshold) {
        P_o2 = P02_threshold;
    }
    else if (P_o2 < 0.01) {
        P_o2 = 0.01;
    }

    if (P_h2 > PH2_threshold) {
        P_h2 = PH2_threshold;
    }
    else if (P_h2 < 0.01) {
        P_h2 = 0.01;
    }

    float numO2 = P_o2/P02_threshold;
    float numH2 = P_h2/PH2_threshold;
    float num = numO2*numH2;

    float vcon = -RT_anF*log(num);
    return vcon;
}
```

D.1.6 Electro-osmotic drag

The electro-osmotic drag is the phenomenon of water transfer from the anode to the cathode due to the flow of protons as described in section 5.4.2. This model is implemented in C++ and executed after the operational point of the cell is found, current, and voltage. The algorithm to calculate the electro-osmotic drag is presented in Cod. 5.

Code 5 Piece of code of the implemented in C++ to calculate the electro-osmotic drag

```
float electroOsmoticDrag(float wc, float wa, float j, float A_m2, float dt){
    float A_cm2 = A_m2*10000;

    float lami = calculateLambda(0.5*(wc+wa));

    float nd = 0.0029*lami*lami + 0.05*lami - 3.4*pow(10,-19);
    float Jeo_molcm2 = nd*j/Faraday;

    float w_mm3 = dt*M_H20/rhoH20_gmm3*A_cm2*Jeo_molcm2;

    return w_mm3;
}
```

D.1.7 Back-diffusion algorithm

The back-diffusion is the counter-effect phenomenon of the electro-osmotic drag, section 5.4.2. The algorithm used to simulate the back-diffusion is present in Cod. 6.

Code 6 Piece of code to implemented in C++ to calculate the electro-osmotic drag

```
float backDiffusion(float wc, float wa, float j, float A_m2, float dt, float ←
    membraneTh = 0.0000275, float wdry = 55., float EW = 1100){

    float A_cm2 = A_m2*10000;

    float lam_c = calculateLambda(wc);
    float lam_a = calculateLambda(wa);

    float D_lam = 2.2* pow(10,-10);
    float Dw_m2s = D_lam*exp(2416 * (1 / 303. - 1 / (273.15+40)));

    float mdry_gm3 = wdry/membraneTh;
    float w_mols = mdry_gm3/EW*Dw_m2s*(lam_c-lam_a)/membraneTh*A_m2*dt;
    float w_mm3 = w_mols*M_H20/rhoH20_gmm3;

    return w_mm3;
}
```

D.2 GDL Model

D.2.1 FTCS algorithm

This section presents a simplified implementation of the FTCS algorithm described in section 6.4.3. The function is implemented in C++ as it is a high-costly algorithm to compute due to the number of elements in the mesh. To simplify the calculations, three different files are loaded, the current state values of each node, the neighbor nodes of each element, the nodes that have a no-flow condition, the length of each file, and the total number of nodes are also passed to the function. The other three variables loaded are the simulated time, the time-step of the solver, and the diffusivity.

The code, Cod. 7, starts by creating a copy of the current state values to a new list and a backup copy, the original list. During the simulation, there are three different stages: a) the state value of the no-flow nodes is set, to ensure there is no gradient, b) the diffusion at the current time step is calculated, and c) the update of the new values is set to the current values.

At the end of the simulation loop, the current step results are returned.

Code 7 Simplified piece of the implemented code in C++ to calculate the FTCS scheme for diffusivity

```

float* simplifiedFTCS(float T[ ], int *neighs[ ], int *noFlow[ ], string filename, int n, int n2, int n3, int n4, float tmax = 10, float dt = 0.001, float alpha = 0.0001)
{
    int* inChannel = readIntList(n4, filename);

    float ti = 0;
    int i0 = 0;
    int i1 = 0;
    int j0 = 0;
    int j1 = 0;
    int ii = 0;

    int element;
    int n0;
    int n1;

    float* Tn = new float[n];
    float* Torg = new float[n];
    for (int i = 0; i < n; ++i) {
        Tn[i] = T[i];
        Torg[i] = T[i];
    }

    while (ti <= tmax) {
        if (n3 > 0) {
            for (int i = 0; i < n3; ++i) {
                n0 = noFlow[i][0];
                n1 = noFlow[i][1];
                T[n0] = T[n1];
            }
        }

        for (int i = 0; i < n2; ++i) {
            ii = neighs[i][0];
            i0 = neighs[i][1];
            i1 = neighs[i][2];
            j0 = neighs[i][3];
            j1 = neighs[i][4];

            // CONSTANT DIFFUSION
            Tn[ii] = T[ii] + alpha*( (T[i0]-2*T[ii]+T[i1]) + (T[j0]-2*T[ii]+T[j1]) );
        }
        for (int i = 0; i <= n; ++i) {
            T[i] = Tn[i];
        }
        ti = ti+dt;
    }

    return T;
}

```

D.2.2 Liquid water removal from GDL

In this section, the implementation of the algorithm to simulate liquid water removal described in section 5.4.5 is presented. The code is executed for each region or element, Cod. 8.

This algorithm uses an internal variable bi that sets if the break-through has started if the water content upper limit has been surpassed if it starts draining water and sets bi to 1.

If the amount of water is below the break-through lower limit bi is set to 0, and the break-through is stopped.

Finally, to ensure that there are no numerical miss-matches if the water content removed in a single time step is higher than the maximum physical allowed water removal, this is set to the maximum physical allowed flow rate.

Code 8 Code of the implemented in Python to calculate the liquid water removal

```
def waterUptake(wi, bi, Am2, Vmm3 = 1, cs = cs, ps = ps):
    smount_breakthru = cs.startbreakthru
    smount_stopBreakthru = cs.stopBreakthru

    if wi > smount_breakthru:
        bi = 1
    elif wi < smount_stopBreakthru:
        bi = 0
    else:
        pass

    if bi == 1:
        q_breakthru_u3s = (wi - cs.swin) * cs.Dqbreak
        q_breakthru_mm3s = q_breakthru_u3s * Vmm3 # * Am2

        wfinal = wi - q_breakthru_u3s
        if wfinal < cs.swin:
            q_breakthru_mm3s = (wi - cs.swin) * Vmm3
            bi = 0

    else:
        bi = 0
        q_breakthru_mm3s = 0

    return q_breakthru_mm3s, bi
```

D.2.3 Water evaporation from the GDL

Water evaporation from the GDL occurs at non-saturated conditions as described in section 5.4.4. Here the equations presented in section 5.4.4 are presented in the piece of code form Cod. 9.

Code 9 Code of the implemented in Python to calculate the droplet movement dynamics

```
def evapModel(wi, Psat_Pa, Pg_Pa, HRi, V_m3, T_K, ugas_ms, ps = ps):  
  
    if wi <= wcut_0:  
        wi_act = 0  
    elif wi >= wcut_0 and wi < wcut_1:  
        wi_act = (wi-wcut_0)  
    elif wi >= wcut_1:  
        wi_act = wcut_1-wcut_0  
  
    if HRi < 1:  
        evp_m3_m3_s = - Kevp * porosity * wi_act * (HRi - 1) * Psat_Pa  
    else:  
        evp_m3_m3_s = 0.  
  
    evp_mm3s = evp_m3_m3_s * V_m3  
  
    return evp_mm3s
```

D.2.4 Water condensation from the GDL

Water evaporation from the GDL occurs at saturated conditions as described in section 5.4.4. Here, the equations presented in section 5.4.4 are shown in the piece of code form Cod. 10.

Code 10 Code of the implemented in Python to calculate the droplet dynamic movement

```
def condModel(wi, Psat_Pa, Pg_Pa, HRi, V_m3, T_K, ugas_ms, ps = ps):
    rho_gmm3 = cs.rho_water*10**(-6)

    if HRi >=1:
        Psat_atm = Psat_Pa/101300.
        cond_molm3_s = - cs.Kcon * ps.porosity * (1 - wi) / (cs.R * T_K) * (HRi-1)* Psat_atm
    else:
        cond_molm3_s = 0

    cond_mm3s = cond_molm3_s* V_m3*cs.M_H20/rho_gmm3

    return cond_mm3s
```

D.3 Droplet movement

The simplified droplet movement functionality is described in section 5.5.3. The implementation of dynamic movement dynamics is implemented in Python language. The Python programmed function is presented in Cod. 11.

Code 11 Code of the implemented in Python to calculate the droplet dynamic movement

```
def simplifiedForcesModel(V_mm3, udrop, vgas, dt, wchannel):
    udrop0 = udrop

    kdrag = 0.15
    dTh_c0 = 0.0025
    dTh_c1 = 0.15

    V_m3 = 1. * V_mm3 * 10 ** (-9)
    R_m = calculateRadius(V_mm3 * 10 ** (-9))

    massdrop_kg = V_m3 * 1000
    D_m = R_m * 2

    if wchannel < D_m:
        Kfriction = 1.5
    else:
        Kfriction = 1

    td = calculateTd(R_m)
    Am2 = calculateDropletArea(R_m)

    v_ulmin = 10 ** -11
    if V_mm3 > v_ulmin:
        Fdrag = cs.kdrag * vair ** 2. * cs.rho_gas * Am2

    dTh0 = cs.dTh_c0 * (180 - cs.contactAngle) * 3.141593 / 180.
    dTh2 = cs.dTh_c1 * udrop

    Fadh = 2 * cs.water_surfaceTension * td * dTh0 * Kfriction
    C = 2 * cs.water_surfaceTension * td * dTh_c1 * Kfriction
    M = massdrop_kg
    A_B = Fdrag - Fadh

    F = (A_B) / C
    % initial condition udrop = 0 at t = 0
    c1 = -F

    udrop = (A_B) / C + c1 * exp(-(C / M) * dt)

    if udrop < 0:
        udrop = 0

    return udrop
```

Bibliography

- [1] “History world first automative competition.” webpage link. Accessed: 2021-May-06.
- [2] K. O. Yoro and M. O. Daramola, “CO₂ emission sources, greenhouse gases, and the global warming effect,” in *Advances in Carbon Capture*, pp. 3–28, Buckingham, England, UK: Woodhead Publishing, 2020.
- [3] H. T. Arat and M. G. Sürer, “State of art of hydrogen usage as a fuel on aviation,” *Eu. Mech. Sci.*, vol. 2, no. 1, pp. 20–30, 2018.
- [4] P. García-Salaberri, D. Sánchez, P. Boillat, M. Vera, and K. Friedrich, “Hydration and dehydration cycles in polymer electrolyte fuel cells operated with wet anode and dry cathode feed: A neutron imaging and modeling study,” *J. Power Sources*, vol. 359, pp. 634 – 655, 2017.
- [5] D. Garcia, T. Ruiu, K. Friedrich, J. Sanchez-Monreal, and M. Vera, “Analysis of the influence of temperature and gas humidity on the performance stability of polymer electrolyte membrane fuel cells,” *J. Electrochem. Soc.*, vol. 163, p. F150, 2015.
- [6] J. M. Andújar and F. Segura, “Fuel cells: History and updating. A walk along two centuries,” *Renewable Sustainable Energy Rev.*, vol. 13, no. 9, pp. 2309–2322, 2009.
- [7] A. J. Appleby, “From Sir William Grove to today: fuel cells and the future,” *J. Power Sources*, vol. 29, no. 1, pp. 3–11, 1990.
- [8] M. Ludwig and L. Carl, “V. A new form of gas battery,” *Proc. R. Soc. Lond.*, vol. 46, no. 280-285, pp. 296–304, 1890.
- [9] C. Stone and A. E. Morrison, “From curiosity to “power to change the world®”,” *Solid State Ionics*, vol. 152-153, pp. 1–13, 2002.
- [10] “A big step for hydrogen fuel cells in cars.” webpage link. Accessed: 2021-Nov-09.
- [11] “World-first home hydrogen battery stores 3x the energy of a powerwall 2.” webpage link. Accessed: 2021-Nov-10.
- [12] “Fuel cell technologies office reaches major patent milestone.” webpage link. Accessed: 2021-Nov-09.
- [13] G. Merle, M. Wessling, and K. Nijmeijer, “Anion exchange membranes for alkaline fuel cells: A review,” *J. Membr. Sci.*, vol. 377, no. 1, pp. 1–35, 2011.
- [14] PubChem, “Method of converting potential energy of carbon into electrical energy - Patent US-555511-A - PubChem,” 2021. [Online; accessed 10. Nov. 2021].

- [15] F. Bidault and P. H. Middleton, “4.07 - Alkaline Fuel Cells: Theory and Application,” in *Comprehensive Renewable Energy*, vol. 4, pp. 179–202, Waltham, MA, USA: Elsevier, 2012.
- [16] E. Gülzow and M. Schulze, “Alkaline fuel cells,” in *Materials for Fuel Cells*, pp. 64–100, Buckingham, England, UK: Woodhead Publishing, 2008.
- [17] E. Agel, J. Bouet, and J. F. Fauvarque, “Characterization and use of anionic membranes for alkaline fuel cells,” *J. Power Sources*, vol. 101, no. 2, pp. 267–274, 2001.
- [18] “Fuel cell - Types of fuel cells,” 2021. [Online; accessed 6. May 2021].
- [19] R. H. Henne and K. A. Friedrich, “Applications – Transportation | Auxiliary Power Units: Fuel Cells,” in *Encyclopedia of Electrochem. P. Sources*, pp. 157–173, Waltham, MA, USA: Elsevier, 2009.
- [20] N. Sammes, R. Bove, and K. Stahl, “Phosphoric acid fuel cells: Fundamentals and applications,” *Curr. Opin. Solid State Mater. Sci.*, vol. 8, no. 5, pp. 372–378, 2004.
- [21] N. H. Behling, “Chapter 4 - History of Phosphoric Acid Fuel Cells,” in *Fuel Cells*, pp. 53–135, Waltham, MA, USA: Elsevier, 2013.
- [22] A. J. Appleby, *Fuel Cells - Phosphoric acid fuel cells / Overview*. Elsevier, 2009.
- [23] “Fuji electric is working to expand the use of phosphoric acid fuel cells.” webpage link. Accessed: 2021-Nov-10.
- [24] H. Abdi, R. Rasouli Nezhad, and M. Salehimaleh, “Chapter 5 - Fuel Cells,” in *Distributed Generation Systems*, pp. 221–300, Oxford, England, UK: Butterworth-Heinemann, 2017.
- [25] A. B. Stambouli and E. Traversa, “Solid oxide fuel cells (SOFCs): a review of an environmentally clean and efficient source of energy,” *Renewable Sustainable Energy Rev.*, vol. 6, no. 5, pp. 433–455, 2002.
- [26] Z. Zakaria, Z. A. Mat, S. H. A. Hassan, and Y. B. Kar, “A review of solid oxide fuel cell component fabrication methods toward lowering temperature,” *Int. J. Energy Res.*, vol. 44, no. 2, pp. 594–611, 2020.
- [27] S. Singhal, *Solid Oxide Fuel Cells: Past, Present and Future*, vol. 55, pp. 1–23. 2013.
- [28] S. C. Singhal, “Solid Oxide Fuel Cells,” *Electrochem. Soc. Interface*, vol. 16, no. 4, p. 41, 2007.
- [29] K. Wang, D. Hissel, M. Péra, N. Steiner, D. Marra, M. Sorrentino, C. Pianese, M. Monteverde, P. Cardone, and J. Saarinen, “A review on solid oxide fuel cell models,” *International Journal of Hydrogen Energy*, vol. 36, no. 12, pp. 7212–7228, 2011.
- [30] L. Barelli, G. Bidini, and G. Cinti, “Operation of a Solid Oxide Fuel Cell Based Power System with Ammonia as a Fuel: Experimental Test and System Design,” *Energies*, vol. 13, no. 23, p. 6173, 2020.

- [31] F. Baldi, L. Wang, M. Pérez-Fortes, and F. Maréchal, “A Cogeneration System Based on Solid Oxide and Proton Exchange Membrane Fuel Cells With Hybrid Storage for Off-Grid Applications,” *Front. Energy Res.*, vol. 6, 2019.
- [32] C. Yuh and M. Farooque, “Fuel cells - molten carbonate fuel cells | materials and life considerations,” in *Encyclopedia of Electrochem. P. Sources*, pp. 497–507, Waltham, MA, USA: Elsevier, 2009.
- [33] S. Dharmalingam, V. Kugarajah, and M. Sugumar, “Membranes for Microbial Fuel Cells,” in *Microbial Electrochemical Technology*, pp. 143–194, Waltham, MA, USA: Elsevier, 2019.
- [34] A. S. Aricò, V. Baglio, and V. Antonucci, *Direct Methanol Fuel Cells: History, Status and Perspectives*. John Wiley & Sons, Ltd, 2009.
- [35] P. Joghee, J. N. Malik, S. Pylypenko, and R. O’Hayre, “A review on direct methanol fuel cells – In the perspective of energy and sustainability,” *MRS Energy & Sustainability*, vol. 2, 2015.
- [36] J. Mergel, H. Janßen, M. Müller, J. Wilhelm, and D. Stolten, “Development of Direct Methanol Fuel Cell Systems for Material Handling Applications,” *J. Fuel Cell Sci. Technol.*, vol. 9, no. 3, 2010.
- [37] V. S. Silva, A. M. Mendes, L. M. Madeira, and S. P. Nunes, “Membranes for direct methanol fuel cell applications: analysis based on characterization, experimentation and modeling,” 2005.
- [38] V. Baglio, A. Di Blasi, A. S. Aricò, V. Antonucci, and E. Traversa, “Influence of TiO₂ Nanometric Filler on the Behaviour of a Composite Membrane for Applications in Direct Methanol Fuel Cells,” *J. New Mater. Electrochem. Syst.*, vol. 7, no. 4, 2004.
- [39] S. Elangovan, J. J. Hartvigsen, and L. J. Frost, “Intermediate Temperature Reversible Fuel Cells,” *Int. J. Appl. Ceram. Technol.*, vol. 4, no. 2, pp. 109–118, 2007.
- [40] V. N. Nguyen and L. Blum, “Reversible fuel cells,” in *Compendium of Hydrogen Energy*, vol. 3, pp. 115–145, Buckingham, England, UK: Woodhead Publishing, 2016.
- [41] G. Levis, *Reversible Fuel Cells Combined with Hydrogen Storage as a Tool to Improve the Electric Grid’s Reliability and Resiliency*. PhD thesis, 2019.
- [42] M. A. Cornachione, *Reversible fuel cell performance and degradation*. PhD thesis, Montana State University - Bozeman, College of Engineering, 2011.
- [43] N. Q. Minh and M. B. Mogensen, “Reversible Solid Oxide Fuel Cell Technology for Green Fuel and Power Production,” *Electrochem. Soc. Interface*, vol. 22, no. 4, pp. 55–62, 2013.
- [44] R. E. Rosli, A. B. Sulong, W. R. W. Daud, M. A. Zulkifley, T. Husaini, M. I. Rosli, E. H. Majlan, and M. A. Haque, “A review of high-temperature proton exchange membrane fuel cell (HT-PEMFC) system,” *Int. J. Hydrogen Energy*, vol. 42, no. 14, pp. 9293–9314, 2017.
- [45] M. Mehrpooya, M. Eikani, G. Nouri, N. Khandan, and A. Hajinezhad, “Role of mea fabrication parameters in PEM fuel cell performance,” 2013.

- [46] Z. Nondudule, J. Chamier, and M. Chowdhury, "Effect of stratification of cathode catalyst layers on durability of proton exchange membrane fuel cells," *Energies*, vol. 14, no. 10, 2021.
- [47] Porstmann, Wannemacher, and Richter, "Overcoming the Challenges for a Mass Manufacturing Machine for the Assembly of PEMFC Stacks," *Machines*, vol. 7, no. 4, p. 66, 2019.
- [48] K. Talukdar, S. Helmly, M. Schulze, D. G. Sanchez, and K. A. Friedrich, "Enveloping of Catalyst Powder by Ionomer for Dry Spray Coating in Polymer Electrolyte Membrane Fuel Cells," *J. Power Sources*, vol. 424, pp. 82–90, 2019.
- [49] A. D. Santamaria, P. K. Das, J. C. MacDonald, and A. Z. Weber, "Liquid-Water Interactions with Gas-Diffusion-Layer Surfaces," *J. Electrochem. Soc.*, vol. 161, no. 12, pp. F1184–F1193, 2014.
- [50] P. Gallo Stampino, D. Molina, L. Omati, S. Turri, M. Levi, C. Cristiani, and G. Dotelli, "Surface treatments with perfluoropolyether derivatives for the hydrophobization of gas diffusion layers for PEM fuel cells," *J. Power Sources*, vol. 196, pp. 7645–7648, 2011.
- [51] R. Schweiss and O. Öttinger, "The importance of carbon materials in micro-porous layer in gas diffusion layers for proton exchange membrane fuel cells," *Carbon*, vol. 93, p. 1079, 2015.
- [52] J. Ramousse, O. Lottin, S. Didierjean, and D. Maillet, "Heat sources in proton exchange membrane (PEM) fuel cells," *J. Power Sources*, vol. 192, no. 2, pp. 435–441, 2009.
- [53] D. Froning, U. Reimer, and W. Lehnert, "Inhomogeneous Distribution of Polytetrafluorethylene in Gas Diffusion Layers of Polymer Electrolyte Fuel Cells," *Transp. Porous Media*, vol. 136, no. 3, pp. 843–862, 2021.
- [54] P. Zhou, C. W. Wu, and G. J. Ma, "Influence of clamping force on the performance of PEMFCs," *J. Power Sources*, vol. 163, no. 2, pp. 874–881, 2007.
- [55] M. Prasanna, H. Y. Ha, E. A. Cho, S. A. Hong, and I.-H. Oh, "Influence of cathode gas diffusion media on the performance of the PEMFCs," *Journal of Power Sources*, vol. 131, no. 1, pp. 147–154, 2004.
- [56] Z. Shangguan, B. Li, P. Ming, and C. Zhang, "Understanding the functions and modifications of interfaces in membrane electrode assemblies of proton exchange membrane fuel cells," *J. Mater. Chem. A*, vol. 9, pp. 15111–15139, 2021.
- [57] T. Corrales-Sánchez, J. Ampurdanés, and A. Urakawa, "MoS₂-based materials as alternative cathode catalyst for PEM electrolysis," *Int. J. Hydrogen Energy*, vol. 39, no. 35, pp. 20837–20843, 2014.
- [58] L. Xia, M. Ni, Q. Xu, H. Xu, and K. Zheng, "Optimization of catalyst layer thickness for achieving high performance and low cost of high temperature proton exchange membrane fuel cell," *Appl. Energy*, vol. 294, p. 117012, 2021.
- [59] Y. Jeon, D. J. Kim, J. K. Koh, Y. Ji, J. H. Kim, and Y.-G. Shul, "Interface-designed Membranes with Shape-controlled Patterns for High-performance Polymer Electrolyte Membrane Fuel Cells - Scientific Reports," *Sci. Rep.*, vol. 5, no. 16394, pp. 1–11, 2015.

- [60] Y. Shao, G. Yin, and Y. Gao, "Understanding and approaches for the durability issues of Pt-based catalysts for PEM fuel cell," *J. Power Sources*, vol. 171, no. 2, pp. 558–566, 2007.
- [61] S. J. Peighambaroust, S. Rowshanzamir, and M. Amjadi, "Review of the proton exchange membranes for fuel cell applications," *Int. J. Hydrogen Energy*, vol. 35, no. 17, pp. 9349–9384, 2010.
- [62] J. Fimrite, H. Struchtrup, and N. Djilali, "Transport phenomena in polymer electrolyte membranes. I. Modeling framework," *J. Electrochem. Soc.*, vol. 152, no. 9, pp. A1804–A1814, 2005.
- [63] B. Tylkowski, J. Walkowiak-Kulikowska, J. Wolska, and H. Koroniak, "Polymers application in proton exchange membranes for fuel cells (PEMFCs)," *Phys. Sci. Rev.*, vol. 2, no. 8, 2017.
- [64] A. Hermann, T. Chaudhuri, and P. Spagnol, "Bipolar plates for PEM fuel cells: A review," *Int. J. Hydrogen Energy*, vol. 30, no. 12, pp. 1297–1302, 2005.
- [65] O. S. Ijaodola, E. Ogungbemi, F. Nisar, T. Wilberforce, and A. G. Olabi, "Evaluating the Effect of Metal Bipolar Plate Coating on the Performance of Proton Exchange Membrane Fuel Cells," *Energies*, vol. 11, no. 11, p. 3203, 2018.
- [66] S. Frangini and F. Zaza, "Anti-Corrosion Methods for Fuel Cell Metal Bipolar Plates: A Review of Recent Patent Literature," *Recent Patents on Corrosion Science*, vol. 1, no. 2, pp. 93–107, 2011.
- [67] Y.-D. Kuan, J.-L. Lyu, T.-R. Ke, M.-F. Sung, and J.-S. Do, "Planar current collector design and fabrication for proton exchange membrane fuel cell," *Int. J. Hydrogen Energy*, vol. 44, no. 20, pp. 10071–10081, 2019.
- [68] V. Ionescu, "Simulating the effect of gas channel geometry on PEM fuel cell performance by finite element method," *Proc. Tech.*, vol. 22, pp. 713–719, 2016.
- [69] W.J. Yang, H.Y. Wang, and Y.B. Kim, "Channel geometry optimization using a 2D fuel cell model and its verification for a polymer electrolyte membrane fuel cell," *Int. J. Hydrogen Energy*, vol. 39, pp. 9430–9439, 2014.
- [70] J.E. Steinbrenner, E.O. Lee, C.H. Hidrovo, J.K. Eaton, and K.E. Goodson, "Impact of channel geometry on two-phase flow in fuel cell microchannels," *J. Power Sources*, vol. 196, pp. 5012–5020, 2011.
- [71] A. Morin, F. Xu, G. Gebel, and O. Diat, "Influence of PEMFC gas flow configuration on performance and water distribution studied by SANS: Evidence of the effect of gravity," *Int. J. Hydrogen Energy*, vol. 36, pp. 3096–3109, 2011.
- [72] M. Erni, W. R. W. Daud, and E. H. Majlan, *Review on Serpentine Flow Field Design for PEM Fuel Cell System*, vol. 447. Trans Tech Publications, 2010.
- [73] A. Baroutaji, J. G. Carton, M. Sajjia, and A. G. Olabi, *Materials in PEM Fuel Cells*. Waltham, MA, USA: Elsevier, 2016.

- [74] Q. Zhang, C. Harms, J. Mitzel, P. Gazdzicki, and K. A. Friedrich, “The challenges in reliable determination of degradation rates and lifetime in polymer electrolyte membrane fuel cells,” *Curr. Opin. Electrochem.*, vol. 31, p. 100863, 2022.
- [75] W.-M. Yan, F. Chen, H.-Y. Wu, C.-Y. Soong, and H.-S. Chu, “Analysis of thermal and water management with temperature-dependent diffusion effects in membrane of proton exchange membrane fuel cells,” *Journal of Power Sources*, vol. 129, no. 2, pp. 127–137, 2004.
- [76] S. Kjelstrup and A. Røsjorde, “Local and Total Entropy Production and Heat and Water Fluxes in a One-Dimensional Polymer Electrolyte Fuel Cell,” *J. Phys. Chem. B*, vol. 109, no. 18, pp. 9020–33, 2005.
- [77] U. Basuli, J. Jose, R. H. Lee, Y. H. Yoo, K.-U. Jeong, J.-H. Ahn, and C. Nah, “Properties and degradation of the gasket component of a proton exchange membrane fuel cell—a review,” *J. Nanosci. Nanotechnol.*, vol. 12, no. 10, pp. 7641–7657, 2012.
- [78] S. Pehlivan-Davis, “Polymer Electrolyte Membrane (PEM) fuel cell seals durability,” 2016.
- [79] Z. Liu, J. Chen, S. Chen, L. Huang, and Z. Shao, “Modeling and Control of Cathode Air Humidity for PEM Fuel Cell Systems,” *IFAC-PapersOnLine*, vol. 50, no. 1, pp. 4751–4756, 2017.
- [80] S. H. Mirfarsi, M. J. Parnian, and S. Rowshanzamir, “Self-Humidifying Proton Exchange Membranes for Fuel Cell Applications: Advances and Challenges,” *Processes*, 2020.
- [81] M. Watanabe, H. Uchida, Y. Seki, M. Emori, and P. Stonehart, “Self-Humidifying Polymer Electrolyte Membranes for Fuel Cells,” *J. Electrochem. Soc.*, vol. 143, no. 12, pp. 3847–3852, 1996.
- [82] “Mercedez benz glc f-cell.” webpage link. Accessed: 2022-Dec-11.
- [83] Y. Wang, D. F. Ruiz Diaz, K. S. Chen, Z. Wang, and X. C. Adroher, “Materials, technological status, and fundamentals of PEM fuel cells – A review,” *Mater. Today*, vol. 32, pp. 178–203, 2020.
- [84] L. Dubau, L. Castanheira, F. Maillard, M. Chatenet, O. Lottin, M. Gaël, J. Dillet, A. Lamibrac, J.-C. Perrin, E. Maukheiber, A. Elkaddouri, G. D. Moor, C. Bas, L. Fladin, and N. Caque, “A review of PEM fuel cell durability: Materials degradation, local heterogeneities of aging and possible mitigation strategies,” *Wiley Interdiscip. Rev. Energy Environ.*, vol. 3, pp. 540–560, 2014.
- [85] J. Wu, X.Z. Yuan, J.J. Martin, H. Wang, J. Zhang, J. Shen, S. Wu, and W. Merida, “A review of PEM fuel cell durability: Degradation mechanisms and mitigation strategies,” *J. Power Sources*, vol. 184, pp. 104–119, 2008.
- [86] F. Bruijijn, V.A. Dam, and F. Janssen, “Review: Durability and degradation issues of PEM fuel cell components,” *Fuel Cells*, vol. 8, pp. 3–22, 2008.
- [87] D. Zhong, R. Lin, Z. Jiang, Y. Zhu, D. Liu, X. Cai, and L. Chen, “Low temperature durability and consistency analysis of proton exchange membrane fuel cell stack based on comprehensive characterizations,” *Appl. Energy*, vol. 264, p. 114626, 2020.

- [88] V. F. Valdes-Lopez, T. Mason, P. R. Shearing, and D. J. L. Brett, "Carbon monoxide poisoning and mitigation strategies for polymer electrolyte membrane fuel cells – A review," *Prog. Energy Combust. Sci.*, vol. 79, no. 27, p. 100842, 2020.
- [89] C. Huang, R. Jiang, M. Elbaccouch, N. Muradov, and J. M. Fenton, "On-board removal of CO and other impurities in hydrogen for PEM fuel cell applications," *J. Power Sources*, vol. 162, no. 1, pp. 563–571, 2006.
- [90] M. Zhao, *Membrane Separation Technology in Carbon Capture*. 2017.
- [91] S. Kang, K. Min, and S. Yu, "Dynamic modeling of a proton exchange membrane fuel cell system with a shell-and-tube gas-to-gas membrane humidifier," *Int. J. Hydrogen Energy*, vol. 37, no. 7, pp. 5866–5875, 2012.
- [92] A. Akinwunmi and H. Pienaar, "Re-Use of the anode exhaust gas of a PEM fuel cell to improve the efficiency and lower the running cost," *2013 IEEE International Conference on Industrial Technology (ICIT)*, 2013.
- [93] N. I. Dmitrieva and M. B. Burg, "Increased Insensible Water Loss Contributes to Aging Related Dehydration," *PLoS One*, vol. 6, no. 5, p. e20691, 2011.
- [94] L. Dubau, J. Durst, F. Maillard, M. Chatenet, and E. Rossinot, "Heterogeneities of aging within a PEMFC MEA," *Fuel Cells*, vol. 12, no. 2, pp. 188–198, 2012.
- [95] S. Mukherjee, J. V. Cole, K. Jain, and A. Gidwani, "Water Management in PEM Fuel Cell: A Lattice-Boltzmann Modeling Approach," *Proceedings of the 7th International Conference on Fuel Cell Science, Engineering, and Technology 2009*, 2009.
- [96] X. Xu, K. Li, Z. Liao, J. Cao, and R. Wang, "A Closed-Loop Water Management Methodology for PEM Fuel Cell System Based on Impedance Information Feedback," *Energies*, vol. 15, no. 20, p. 7561, 2022.
- [97] M. L. Sarmiento Carnevali, *Modeling and control of PEM fuel cells*. PhD thesis, Universitat Politècnica de Catalunya, 2017.
- [98] G. Zhang and K. Jiao, "Multi-phase models for water and thermal management of proton exchange membrane fuel cell: A review," *J. Power Sources*, vol. 391, pp. 120–133, 2018.
- [99] P. K. Bhattacharya, "Water flooding in the proton exchange membrane fuel cell," 2015.
- [100] A. Sorrentino, K. Sundmacher, and T. Vidakovic-Koch, "Polymer Electrolyte Fuel Cell Degradation Mechanisms and Their Diagnosis by Frequency Response Analysis Methods: A Review," *Energies*, vol. 13, no. 21, p. 5825, 2020.
- [101] S. Kandlikar and Z. Lu, "Thermal management issue in PEMFC stack - A brief review of current status," *Appl. Therm. Eng.*, vol. 29, pp. 1276–1280, 2009.
- [102] J. D. Rojas, C. Kunusch, C. Ocampo-Martínez, and V. Puig, "Control-Oriented Thermal Modeling Methodology for Water-Cooled PEM Fuel-Cell-Based Systems," *IEEE Trans. Ind. Electron.*, vol. 62, no. 8, pp. 5146–5154, 2015.

- [103] L. Xing, W. Xiang, R. Zhu, and Z. Tu, "Modeling and thermal management of proton exchange membrane fuel cell for fuel cell/battery hybrid automotive vehicle," *Int. J. Hydrogen Energy*, vol. 47, no. 3, 2021.
- [104] G. Zhang, H. Yuan, Y. Wang, and K. Jiao, "Three-dimensional simulation of a new cooling strategy for proton exchange membrane fuel cell stack using a non-isothermal multiphase model," *Appl. Energy*, vol. 255, p. 113865, Dec. 2019.
- [105] C. H. Woo and J. B. Benziger, "PEM fuel cell current regulation by fuel feed control," *Chem. Eng. Sci.*, vol. 62, no. 4, pp. 957–968, 2007.
- [106] L. Valiño, R. Mustata, and L. Dueñas, "Consistent modeling of a single PEM fuel cell using Onsager's principle," *Int. J. Hydrogen Energy*, vol. 39, no. 8, pp. 4030–4036, 2014.
- [107] B. Xie, Y. Jiang, G. Zhang, Y. Yin, Q. Du, and K. Jiao, "Large-scale simulation of pem fuel cell using a "3d+1d" model," 04 2020.
- [108] L. Xuan, Y. Wang, D. Mei, and J. Lan, "Design and Modelling of 3D Bionic Cathode Flow Field for Proton Exchange Membrane Fuel Cell," *Energies*, vol. 14, no. 19, p. 6044, 2021.
- [109] M. A. Rahman, F. Mojica, M. Sarker, and P.-Y. A. Chuang, "Development of 1-D multiphysics PEMFC model with dry limiting current experimental validation," *Electrochim. Acta*, vol. 320, p. 134601, 2019.
- [110] U. Pasaogullari and C. Wang, "Liquid water transport in gas diffusion layer of polymer electrolyte fuel cells," *J. Electrochem. Soc.*, vol. 151, 2004.
- [111] D. Niblett, A. Mularczyk, V. Niasar, J. Eller, and S. Holmes, "Two-phase flow dynamics in a gas diffusion layer - gas channel - microporous layer system," *J. Power Sources*, vol. 471, p. 228427, 2020.
- [112] P. A. García-Salaberri, M. Vera, and R. Zaera, "Nonlinear orthotropic model of the inhomogeneous assembly compression of PEM fuel cell gas diffusion layers," *Int. J. Hydrogen Energy*, vol. 36, no. 18, pp. 11856–11870, 2011.
- [113] C. Qin, "Water transport in the gas diffusion layer of a polymer electrolyte fuel cell: Dynamic pore-network modeling," *J. Electrochem. Soc.*, vol. 162, pp. F1036–F1046, 2015.
- [114] F. S. Nanadegani, E. N. Lay, and B. Sunden, "Effects of an MPL on water and thermal management in a PEMFC," *Int. J. Energy Res.*, vol. 43, no. 1, pp. 274–296, 2019.
- [115] X. Wang, B. Zhou, and M. Jiang, "Dynamic contact angle effects on gas-liquid transport phenomena in proton exchange membrane fuel cell cathode with parallel design," *Int. J. Energy Res.*, vol. 42, no. 10, 2018.
- [116] S. Dutta, S. Shimpalee, and J. W. Van Zee, "Three-Dimensional Numerical Simulation of Straight Channel PEM Fuel Cells," *J. Appl. Electrochem.*, vol. 30, no. 2, pp. 135–146, 2000.
- [117] E. Tardy, F. Courtois, M. Chandesris, J.-P. Poirot-Crouvezier, A. Morin, and Y. Bultel, "Investigation of liquid water heterogeneities in large area PEM fuel cells using a pseudo-3D multiphysics model," *Int. J. Heat Mass Transfer*, vol. 145, p. 118720, 2019.

- [118] O. B. Rizvandi and S. Yesilyurt, “A transient Pseudo-3D model of the PEM fuel cell for the analysis of dead-ended anode and anode bleeding operation modes,” *Electrochimica Acta*, vol. 324, p. 134866, 2019.
- [119] C. Yin, J. Li, Y. Zhou, H. Zhang, P. Fang, and C. He, “Phase Separation and Development of Proton Transport Pathways in Metal Oxide Nanoparticle/Nafion Composite Membranes during Water Uptake,” *J. Phys. Chem. A*, vol. 122, pp. 9710–9717, 2018.
- [120] E. C. Kumbur, K. V. Sharp, and M. M. Mench, “Validated Leverett Approach for Multiphase Flow in PEFC Diffusion Media,” *J. Electrochem. Soc.*, vol. 154, no. 12, 2007.
- [121] T. Berning, *On the Nature of Electro-Osmotic Drag*. PhD thesis, Multidisciplinary Digital Publishing Institute, 2020.
- [122] R. Vetter and J. O. Schumacher, “Free open reference implementation of a two-phase PEM fuel cell model,” *Comput. Phys. Commun.*, vol. 234, pp. 223–234, 2019.
- [123] A. Esposito, C. Pianese, and Y. G. Guezennec, “Coupled modeling of water transport and air–droplet interaction in the electrode of a proton exchange membrane fuel cell,” *J. Power Sources*, vol. 195, no. 13, pp. 4149 – 4159, 2010.
- [124] M. Lindstrom and B. Wetton, “A comparison of fick and maxwell-stefan diffusion formulations in PEMFC cathode gas diffusion layers,” *Heat Mass Transfer*, vol. 53, 2013.
- [125] À. J. Arabí, “Analysis of droplet dynamics on the GDL surface of a PEM fuel cell cathode,” Master’s thesis, UPC, 2013.
- [126] K. Raman, B. Mondal, and X. Li, “Water droplet transport in single gas flow channel of PEM fuel cell,” *Int. J. Adv. Ther. Sci. Eng.*, vol. 2, pp. 27–33, 2011.
- [127] P. Thanh Nguyen, T. Berning, M. Bang, and N. Djilali, “A three-dimensional model of PEM fuel cells with serpentine flow channels,” *INIS*, vol. 35, 2003.
- [128] C. Kunusch, P. F. Puleston, M. A. Mayosky, and J. J. Moré, “Characterization and experimental results in PEM fuel cell electrical behaviour,” *Int. J. Hydrogen Energy*, vol. 35, no. 11, pp. 5876 – 5881, 2010.
- [129] D. M. Bernardi and M. W. Verbrugge, “A Mathematical Model of the Solid-Polymer-Electrolyte Fuel Cell,” *J. Electrochem. Soc.*, vol. 139, no. 9, pp. 2477–2491, 1992.
- [130] T. Springer, T. A. Zawodzinski, and S. Gottesfeld, “Polymer electrolyte fuel cell model,” *J. Electrochem. Soc.*, vol. 138, pp. 2334–2342, 1991.
- [131] L. Mazzapioda, S. Panero, and M. Navarra, “Polymer electrolyte membranes based on nafion and a superacidic inorganic additive for fuel cell applications,” *Polymers*, vol. 11, p. 914, 2019.
- [132] J. Santana-Villamar, M. Espinoza-Andaluz, and M. Andersson, “Impact of the Temperature on the Proton Conductivity and Power Output of a PEFC Operating at High Current Densities,” *IOP Conf. Ser.: Earth Environ. Sci.*, vol. 994, no. 1, p. 012006, 2022.

- [133] R. O'Hayre, S.-W. Cha, W. Colella, and F. B. Prinz, *Fuel Cell Fundamentals*. Wiley, 2016.
- [134] V. Liso, G. Savoia, S. S. Araya, G. Cinti, and S. K. Kær, "Modelling and Experimental Analysis of a Polymer Electrolyte Membrane Water Electrolysis Cell at Different Operating Temperatures," *Energies*, vol. 11, no. 12, p. 3273, 2018.
- [135] M. A. Salam, M. S. Habib, P. Arefin, K. Ahmed, and N. Papri, "Effect of Temperature on the Performance Factors and Durability of Proton Exchange Membrane of Hydrogen Fuel Cell: A Narrative Review," *Material Science Research India*, vol. 17, no. 2, pp. 179–191, 2020.
- [136] C. Cai, Y. Rao, Y. Zhang, F. Wu, S. Li, and M. Pan, "Failure mechanism of PEM fuel cell under high back pressures operation," *Int. J. Hydrogen Energy*, vol. 44, no. 26, pp. 13786–13793, 2019.
- [137] Q. Duan, H. Wang, and J. Benziger, "Transport of liquid water through Nafion membranes," *J. Membr. Sci.*, vol. s 392-393, pp. 88–94, 2012.
- [138] I. Ali and N. A. Malik, "A Realistic Transport Model with Pressure-Dependent Parameters for Gas Flow in Tight Porous Media with Application to Determining Shale Rock Properties," *Transp. Porous Media*, vol. 124, no. 02, 2018.
- [139] M. E. A. and M. A. P., *Gas transport in porous media : the dusty-gas model*. Elsevier Scientific Pub. Co Amsterdam ; New York, 1983.
- [140] C. Chan, N. Zamel, X. Li, and J. Shen, "Experimental measurement of effective diffusion coefficient of gas diffusion layer/microporous layer in PEM fuel cells," *Electrochim. Acta*, vol. 65, pp. 13–21, 2012.
- [141] P. K. Sinha and C.-Y. Wang, "Pore-network modeling of liquid water transport in gas diffusion layer of a polymer electrolyte fuel cell," *Electrochim. Acta*, vol. 52, no. 28, pp. 7936–7945, 2007.
- [142] D. Zhang, Q. Cai, and S. Gu, "Three-dimensional lattice-Boltzmann model for liquid water transport and oxygen diffusion in cathode of polymer electrolyte membrane fuel cell with electrochemical reaction," *Electrochim. Acta*, vol. 262, pp. 282–296, 2018.
- [143] T. Bednarek and G. Tsotridis, "Calculation of effective transport properties of partially saturated gas diffusion layers," *J. Power Sources*, vol. 340, pp. 111–120, 2017.
- [144] C. Si, X.-D. Wang, W.-M. Yan, and T.-H. Wang, "A Comprehensive Review on Measurement and Correlation Development of Capillary Pressure for Two-Phase Modeling of Proton Exchange Membrane Fuel Cells," *J. Chem.*, vol. 2015, p. 876821, 2015.
- [145] Z. Zhan, J. Xiao, D. Li, M. Pan, and R. Yuan, "Effects of porosity distribution variation on the liquid water flux through gas diffusion layers of PEM fuel cells," *J. Power Sources*, vol. 160, no. 2, pp. 1041–1048, 2006.
- [146] Q. Ye and T. Van Nguyen, "Three-Dimensional Simulation of Liquid Water Distribution in a PEMFC with Experimentally Measured Capillary Functions," *J. Electrochem. Soc.*, vol. 154, no. 12, 2007.

- [147] S. Chaudhary, V. K. Sachan, and P. K. Bhattacharya, “Two dimensional modelling of water uptake in proton exchange membrane fuel cell,” *Int. J. Hydrogen Energy*, vol. 39, no. 31, pp. 17802 – 17818, 2014.
- [148] D. Donnarumma, G. Tomaiuolo, S. Caserta, Y. Gizaw, and S. Guido, “Water evaporation from porous media by dynamic vapor sorption,” *Colloids Surf., A*, vol. 480, pp. 159 – 164, 2015.
- [149] X. Wang and T. Van Nguyen, “Modeling the Effects of Capillary Property of Porous Media on the Performance of the Cathode of a PEMFC,” *J. Electrochem. Soc.*, vol. 155, no. 11, 2008.
- [150] C.-M. Hwang, M. Ishida, H. Ito, T. Maeda, and T. Yoshida, “Effect of PTFE contents in the Gas Diffusion Layers of Polymer Electrolyte-based Unitized Reversible Fuel Cells,” *J. Int. Council. Electr. Eng.*, vol. 2, no. 2, 2012.
- [151] A. Santamaria, P. Das, J. C. MacDonald, and A. Weber, “Liquid-water interactions with gas-diffusion-layer surfaces,” *J. Electrochem. Soc.*, vol. 161, pp. F1184–F1193, 2014.
- [152] M. Mortazavi and K. Tajiri, “Liquid water breakthrough pressure through gas diffusion layer of proton exchange membrane fuel cell,” *Int. J. Hydrogen Energy*, vol. 39, no. 17, pp. 9409–9419, 2014.
- [153] S. Lal, A. Lamibrac, J. Eller, and F. N. Büchi, “Determination of Water Evaporation Rates in Gas Diffusion Layers of Fuel Cells,” *J. Electrochem. Soc.*, vol. 165, no. 9, pp. F652–F661, 2018.
- [154] A. Gad and A. Abd-Elaal, “Practical guidelines for a reliability-based design of building water supply systems,” *Urban Water J.*, vol. 13, no. 2, pp. 1–14, 2015.
- [155] B. Mondal, K. Jiao, and X. Li, “Three-dimensional simulation of water droplet movement in PEM fuel cell flow channels with hydrophilic surfaces,” *Int. J. Energy Res.*, vol. 35, no. 13, pp. 1200–1212, 2010.
- [156] À. Jarauta, M. Secanell, J. Pons-Prats, P. Ryzhakov, S. R. Idelsohn, and E. Oñate, “A semi-analytical model for droplet dynamics on the GDL surface of a PEFC electrode,” *Int. J. Hydrogen Energy*, vol. 40, no. 15, pp. 5375 – 5383, 2015.
- [157] C. H. Schillberg and S. G. Kandlikar, “A review of models for water droplet detachment from the gas diffusion layer-gas flow channel interface in PEMFCs,” in *ASME 5th Int. Conf. Nanochannels, Microchannels, and Minichannels*, vol. 4272X, pp. 1–12, 2007.
- [158] C. W. Extrand and Y. Kumagai, “Liquid Drops on an Inclined Plane: The Relation between Contact Angles, Drop Shape, and Retentive Force,” *J. Colloid Interface Sci.*, vol. 170, no. 2, pp. 515–521, 1995.
- [159] P. Polverino, A. Esposito, and C. Pianese, “Experimental validation of a lumped model of single droplet deformation, oscillation and detachment on the GDL surface of a PEM fuel cell,” *Int. J. Hydrogen Energy*, vol. 38, no. 21, pp. 8934–8953, 2013.

- [160] A. Esposito, P. Polverino, C. Pianese, and Y. G. Guezennec, “A Lumped Model of Single Droplet Deformation, Oscillation and Detachment on the GDL Surface of a PEM Fuel Cell,” *ASME 2010 8th International Conference on Fuel Cell Science, Engineering and Technology, FUELCELL 2010*, vol. 1, 2010.
- [161] P. R. Griffiths, “Static and Dynamic Components of Droplet Friction,” *Digital Commons @ University of South Florida*, 2013.
- [162] A. Esposito, A. Motello, C. Pianese, and Y. G. Guezennec, “Numerical Modeling and Experimental Analysis of Air-Droplet Interaction in the Channel of a Proton Exchange Membrane Fuel Cell,” *J. Fuel Cell Sci. Technol.*, vol. 7, no. 3, 2010.
- [163] S. C. Cho, Y. Wang, and K. S. Chen, “Droplet dynamics in a polymer electrolyte fuel cell gas flow channel: Forces, Deformation and detachment. II: Comparisons of analytical solution with numerical and experimental results,” *J. Power Sources*, vol. 210, pp. 191–197, 2012.
- [164] P. Gopalan and S. G. Kandlikar, “Droplet-Sidewall Dynamic Interactions in PEMFC Gas Channels,” *J. Electrochem. Soc.*, vol. 159, p. F468, July 2012.
- [165] H. Holterman, *Kinetics and evaporation of water drops in air*. IMAG report 2003, 2003.
- [166] P. Hawkes and E. Kasper, “Chapter 11 - The Finite-Difference Method (FDM),” in *Principles of Electron Optics (Second Edition)*, pp. 167–183, Waltham, MA, USA: Elsevier, 2018.
- [167] S. E. A. Alhazmi, “Numerical Solution of Fisher’s Equation Using Finite Difference,” *Bulletin Appl. Math. Sci. and Apps.*, vol. 12, pp. 27–34, 2015.
- [168] “NafionXL specifications datasheet.” Accessed: 2020-12-22.
- [169] J. Song, Q. Ye, K. Wang, Z. Guo, and M. Dou, “Degradation Investigation of Electrocatalyst in Proton Exchange Membrane Fuel Cell at a High Energy Efficiency,” *Molecules*, vol. 26, no. 13, 2021.
- [170] P. Pucheng, Y. Li, H. Xu, and Z. Wu, “A review on water fault diagnosis of PEMFC associated with the pressure drop,” *Appl. Energy*, vol. 173, pp. 366–385, 2016.
- [171] “Sigracet BC specifications datasheet.” Accessed: 2020-10-04.
- [172] N. Pourmahmoud, S. Rezazadeh, I. Mirzaee, and V. Heidarpour, “Three-dimensional numerical analysis of proton exchange membrane fuel cell,” *J. Mech. Sci. Technol.*, vol. 25, no. 10, p. 2665, 2011.
- [173] V. M. Truong, N. B. Duong, and H. Yang, “Effect of Gas Diffusion Layer Thickness on the Performance of Anion Exchange Membrane Fuel Cells,” *Processes*, vol. 9, no. 4, p. 718, 2021.
- [174] D. H. Jeon, “Effect of gas diffusion layer thickness on liquid water transport characteristics in polymer electrolyte membrane fuel cells,” *J.s Power Sources*, vol. 475, p. 228578, 2020.
- [175] C. Francia, V. S. Ijeri, S. Specchia, and P. Spinelli, “Estimation of hydrogen crossover through Nafion (R) membranes in PEMFCs,” *J. Power Sources*, vol. 196, no. 4, pp. 1833–1839, 2011.